Electrical Resistance Tomography for Multiphase flow in water industry

Chen, Bo

Award date:
2019

Awarding institution:
University of Bath

Electrical Resistance Tomography for Multiphase flow in water industry

Author: Bo Chen

A thesis submitted for the degree of

Doctor of Philosophy

University of Bath

Department of Electrical and Electronic Engineering

Bath, Mar 2019

Declaration

I declare that I have read and understood the entry in the Student Handbook for the Department of Electronic and Electrical Engineering on Cheating and Plagiarism and that all material in this thesis is my own work, except where I have indicated with appropriate references. It is being submitted for in fulfilment of the requirements of the degree of Doctor of Philosophy in Electronic and Electrical Engineering. No portion of the work in this document has been submitted before for any degree or examination at any other university.

Signature of Author.....

Date .....

Abstract

The main purpose of this thesis is to develop a better understanding of the interfaces between materials in spatial and time domains via 2D and 3D visualization and quantitative parameter measurement using Electrical Resistance Tomography (ERT). Some advantages of ERT have been reported as being a high temporal resolution, low-cost and non-radiation emitting. The ERT modality is generally used to visualize the interior of a region by mapping the conductivity distribution using potential difference that is measured by electrodes that are attached to the medium. The main algorithm for image reconstruction that has been used is total variation regularisation due to its potential for producing high-quality images with sharp boundaries. In this work, a series of simulation studies and lab-based phantom experimental tests were conducted.

Contributions of this thesis are generally categorized into three aspects. First of all, a spatial-temporal total variation based on the Split Bregman method has been proposed for analyzing dynamical movement of a target in a circular tank based on 2D ERT, where spatial and temporal gradients were employed for exploring performance in the space and time domains, and time response of dynamical ERT images has been proposed for the comparison and illustration of advantages of sharp dynamical images. Furthermore, the proposed STTV has extended to 3D ERT visualization, where a tank with the shape of a vertical pipe has been designed with a dual-plane aiming at representing interior information by producing dynamical images of a moving target inside the pipe. Velocity measurements are feasible based on 2D/3D ERT and the cross-correlation method, and the accuracy of these was discussed. Moreover, a planar array for 3D ERT visualization was used to overcome the issue that 3D ERT visualizations based on traditional electrode-ring sensors would suffer from the low resolution on the axis-direction along the pipe, especially the region between rings where electrode-ring gaps lead to missing data. Results showed that ERT planar array can extract additional information in its detectable region with a higher 3D spatial resolution, and a combination of planar array and ring-electrode ERT can potentially be made for the purpose of exploring more information in a pipeline.

In general, this thesis represents the research works on improving the performance of static/dynamical ERT visualization and quantitative parameter measurements. These works have potential applications in flow imaging and tomography-based measurement or control systems in the future. Detailed applications and further work are suggested. Although ERT is a new imaging technique and lots of issues are still preserved to be solved, it is believed that such research would have contributions to the future development of electrical impedance tomography research.

List of Publications

1. *Chen, B., Abascal, J. and Soleimani, M. (2018). Electrical Resistance Tomography for Visualization of Moving Objects Using a Spatiotemporal Total Variation Regularization Algorithm. Sensors, 18(6), p. 1704.*

2. *Chen, B., Abascal, J. and Soleimani, M. (2018). Extended Joint Sparsity Reconstruction for Spatial and Temporal ERT Imaging. Sensors, 18(11), p.4014.*

3. *Chen, B., Soleimani, M. (2018). Depth analysis of planar array for 3D electrical impedance tomography (submitted to IEEE Sensors)*

Acknowledgments

This study was carried out in the Department of Electronic and Electrical Engineering at the University of Bath from September 2015. I sincerely thank everyone who gave me support during my research.

Above all, I would like to express my greatest gratitude to my supervisor Professor Manuchehr Soleimani. He provided me with an opportunity to begin my Ph.D. after I finished my B.eng. During these last three years, Professor Manuchehr always gave me technical support, great ideas, and valuable suggestions. This thesis would have never been completed without his strong support, inspiration, and professional guidance

In addition, I wish to express my greatest thanks to my parents. They educated me all the way, and I would not even of had the chance to come to the University of Bath without their financial support. During the research study, they always provided me with mental support, and encourage me to carry on when I faced difficulties.

Moreover, I wish to express my greatest gratitude to Dr. Chao Tan from Tianjin University for his guidance in my first-year exploration of multiphase flow. Also thanks to Dr. Juan E.P.J. Abascal for the support on algorithms, and his contributions to two published journal papers as co-author. And Mr. Dong Xiaoxiao for his patience when answering my many technical questions.

In the end, I would like to thank my group mates, especially Mrs. Quanbao Wu, Mrs. Fang Li, Dr. Ander, Dr. Carl, Mrs. Dan Jiang, Mrs. Gege Ma, Ms. Jing Hu, Ms. Xi Duan for many scientific and non-scientific discussions during my journey.

List of Figures

List of Tables

List of Symbols

$\nabla -$ divergence operator

$\vec{E} -$ electric field

$\vec{B} -$ magnetic field

$\vec{D} -$ electric displacement vector

$J_D -$ displacement current density

$J_c -$ conducting current density

$\vec{H} -$ magnetic field intensity

$\sigma -$ conductivity

$\varepsilon -$ permittivity

$\varphi -$ electric potential

$\vec{\mathrm{n}} -$ outward normal vector

Nomenclature

EIT – Electrical Impedance Tomography

ERT – Electrical Resistance Tomography

ECT – Electrical Capacitance Tomography

MIT – Magnetic Induction Tomography

CEM – Complete Electrode Model

FEM – Finite Element Method

TOS – Temprol One step Solver

TV – Total Variation

STTV – Spatiotemporal Total Variation

SBTV – Split Bregman Total Variation

EMF – Electromagnetic Flowmeter

OEIT – Open domain Electrical Impedance Tomography

Content

Chapter 1 Introduction

Tomography is a technique for mapping the cross-section of an object of interest, this has been utilized in various aspects of science, for example, in scanning or imaging techniques in the medical field for clinical detection in patients; in the monitoring of industrial process and components analysis in geophysical or materials science are also important for humans to explore the knowledge of objects of interest. Two categories of tomographic methods are usually employed: Hard-field tomography and soft-field tomography. Some of the mature and well-known imaging techniques, like X-ray, CT, $\gamma - \mathrm{ray}$ are classified as hard-field tomography, where the signal or Electromagnetic waves generated from the radiator source propagate along straight lines, and materials of the medium would affect the transmitting path or strength. Hard-field tomography is high image-quality and has been widely used in different areas, however, the equipment is normally high-cost and the radiation can be harmful to targets, such as the human body. Soft-field tomography can also be used in different applications, especially electrical tomographic methods, such as, Electrical Resistance Tomography (ERT), Electrical Capacitance Tomography (ECT), and Electromagnetic Tomography (EMT). Generated signals are commonly transmitted as electrical or magnetic fields, and the complicated features of the Electromagnetic field can cause difficulties for image reconstruction, however, they do benefit from being low-cost, non-invasive, and of high speed. Generally, in soft-field tomography, admittivity is combined with conductivity and permittivity. ERT conducts current density via attached electrodes, which requires a conductive medium, and its imaging utilizes conductivity distribution. ECT imaging is based on the permittivity distribution of the medium by measuring the conductance via capacitive plates, without making contact with the region. For process tomography of two-phase flow imaging, ERT works for a water-dominated flow, but it is not valid for an oil-dominated flow, and ECT is commonly used instead for cases of detection in oil-phase dominated two-phase flows.

Table 1.1 Electrical tomographic techniques

Technique	Sensors	Measurements	Distribution
EIT	Electrodes	Impedance	Conductivity
ECT	Capacitive plates	Capacitance	Permittivity
ERT	Electrodes	Resistance	Conductivity
EMT(MIT)	Inductive coils	Mutual inductance	Admittivity

1.1 Electrical Resistance Tomography

Electrical impedance tomography (EIT) is one of the electrical tomographic methods that maps the conductivity distribution throughout the domain of interest. The domain should normally be a conductive medium to conduct an injected current density over the region, the resulting potentials are taken via electrodes to map the internal conductivity. Such mediums are present in a variety of areas, such as, human tissue, flow pipelines, and fabrics [1]. The implementation of EIT requires the measured current/potential by attached electrodes, placed on the boundary of the conductive domain, which makes it simple and high-speed when compared with mature hard-field tomographic methods. The current source is utilized to produce current density and generate an electric field, whilst high-cost and complicated radiation generators are required for methods such as CT, $\mathrm{x}-\mathrm{ray}$, $\gamma - ray$, although these techniques are relatively mature and have been widely used in daily life. Electrical resistance tomographic techniques in this case have great potential in the future. However, ERT is suffering from low spatial resolution and a poor signal-to-noise-ratio (SNR) as the number of electrodes cannot be infinitely increased in practise, which leads to the problem of missing data. The Ill-posed ERT inverse problem is also an issue that leads to uncertainty in the image reconstruction results. Although the image quality of ERT visualised results is incomparable with conventional matured tomographic modalities, it has still triggered much attention in solving many engineering problems due to its advantages of being non-invasive, non-radiation emitting, having a high time resolution, and being low-

cost. A conventional EIT system is composed of a hardware system, sensor, software, and a PC. Hardware is one of the most important and complicated components that drives the current generated via a constant current or voltage source, where low-frequency and constant-amplitude current or voltage is produced. A set of volt/current meters on corresponded electrodes are applied for data measurement. The sensor is where the region to be tested and acquire data from is, which contains a conductive medium and target. In addition, the PC is another important component that provides the functions of modelling for solving the forward problem, making effective calculations, as well as creating the visualization via a variety of algorithms.

The early idea of mapping the resistivity distribution can be traced back to the early 20th century when people started to detect geological structure information for the demands of planning natural resources and dealing with the rising pressures on the environment [2]. More than a hundred years ago, the computer had not yet been invented, which meant many works, such as data measurement had to be done manually. People were using a few electrodes to engage in their prospecting works in geophysical detection, a pair of electrodes were used to generate a DC signal via the ground and employing other electrodes to get potential data. To acquire more effective information, they had to move the electrodes by hand for more data measurements. In addition, the works were also restricted by the time-consuming calculations without the assistance of PC. With the birth and great development of computers a few decades later, the process of imaging techniques was developed too, and this was coupled with a rapid improvement in the data analyzing process. Systems with more electrodes were starting to be zutilized from 1981 due to the improvement in computational speed, and PC-controlled switching was produced for electrodes shifting instead of manually controlled ones from 1989.

In the early 1980s, the ideas of EIT research were focusing a lot on clinical applications. Ideas of measuring different tissues in the human body were proposed, such as the thorax [3], lungs [4], breasts [5], new-borns [6], however, most of those works were only in the theoretical stage. Since vivo imaging methods were produced in 1984 [7], more researchers proposed their works in medical applications, aiming at detecting various diseases, such as, in human brain function [8], pulmonary function [9], gastric function [10], breast cancer [11], and also thermal monitoring of hyperthermia treatment [12].

Nowadays, EIT as a new emerging modality contributes to many technology fields [13]. In material engineering, EIT is employed to map the structure of materials. For example, Tsung-Chin Hou and their groups used EIT to detect the response of carbon nanotube thin films in different pH environments [14]. In Biotechnology, literature has shown that EIT can suggest some cell information, such as, cell viability, distribution, cell size and cell activity, by measuring the spatial distribution of electric properties. Meir proposed a feasibility study in 2014 [15] aiming at developing a new method of monitoring the electroporation process of cells, and results showing that EIT would potentially be useful in such an application of imaging spatial and temporal distributions of dynamical processes. In [16], the authors explored cell distributions within a hydrogel and a microporous scaffold using frequency-difference EIT. For more literature one can also refer to [17] [18] [19] [20].

The EIT technique also contributes to industrial applications, and can be used in process assessment, and the visualization tomographic method also benefits from the high time resolution of EIT technology making it capable of zvisualizing long-term industrial processes. Flow is commonly encountered in many industrial processes, and the ERT technique appears in many applications of flow measurement and process visualizations. Many fields started to develop ERT as a new measurement method, and much literature of different applications has been proposed, for example, it was applied to non-uniform foaming density detection in 1999 by a Manchester group [21], and M Henningson proposed their works to determine the velocity profile of yogurt flow using ERT with the assistance of cross-correlation [22]. In the petroleum industry, the management of oil production is always required, and measurements of oil-water two-phase flow is often a topic that attracts much attention. Quantitative parameters, such as, flow rate, and void fraction, are important factors for justifying oil production, water disposal or reinjection [23]. ERT can be applied to oil-in-water flows, where the oil-phase is acting as a disperse phase. In [24], authors show their works of ERT-based flow measurement methods, where they proposed their method of measuring flow rate using raw data collected from an ERT system. More recently, in [25], *Y. Faraj et al* presented their work about measuring oil-in-water flow rate in a vertical pipe with a combination of ERT and Electromagnetic Flowmeter (EMF). The method of flow pattern analysis is proposed in [26], where dynamical information is extracted via time-series from 16 electrodes of ERT, and flow pattern separation is conducted whilst jointly

utilizing the correlation dimension of the multivariate time-series. For the scenarios of high conductive oil, where water is a continuous-phase, ERT is appropriate to be applied for analyzing such types of two-phase flow. In the past few decades, much proposed research has shown the feasibility of doing analyses or measurements based on the ERT modality. In [23], *J Jia et al* investigated oil-water two-phase flow with different void fractions using ERT and proved that visualizations on both directions are available, and the measurement of high conductive oil using ERT is experimentally validated. In water in industrial processes, ERT is also applied to gas-liquid flow, such as, gas-phase flow rate measuring [27], flow regime identification [28], void fraction estimation [29] [30], gas hold-up [31], and bubble behavior analysis [32].

1.2 Thesis motivation

The main objective of research works of this Ph.D. Thesis is to develop a better understanding of phase interface by visualizing dynamical movement of a target for potential flow measurements using 2D/3D ERT as a modality of process tomography. ERT is a new emerging tomographic method and has been investigated for a few decades. Although ERT suffers from low spatial resolution, and few flow measurements are based on reconstructed images, TV regularisation can produce a sharp interface between materials and hopefully can enhance the image quality. In addition, high temporal resolution is one of the advantages of ERT, but most algorithms are based on frame-by-frame reconstructions, which cannot make use of temporal information. Moreover, most previous works have been done in 2D, however, 2D ERT reconstructs images based on a cross-section of the region of interest that is located on the plane of electrode sensor, which neglects information outside the cross-section. To visualize volumetric information of a target may bring a worse situation of solving an ill-posed ERT inverse problem, but it still worth the effort. To solve these problems, the following ideas are utilize various combinations. Above all, 2D/3D ERT imaging is investigated. Furthermore, regarding the monitoring of dynamical processes of industrial applications, the target being tested is non-static, which also brings about difficulties in visualizations. Conventional frame-by-frame algorithms suffer from noise introduced by inter-frame data, and a high enough data collection rate of the ERT devices is

also required. To solve such problems, the temporal information can be given more attention by regularising over a time series with redundant information on neighboring frames. Since TV can produce high-quality images, it is expected to further develop the TV regularisation algorithm in both the spatial and time domains due to the high temporal resolution of ERT. In addition, to further improve the spatial resolution, an ERT planar array sensor is employed, and combinations of both types of ERT sensors are supposed to exploit information from flow pipelines together. A list of targets has been conducted for smoothly meeting the motivation:

- Review literature on ERT background, mathematical models of basic working principles, and previous related works.
- Establish ERT forward modeling.
- Analyze and compare different algorithms for the ERT inverse problem.
- Understand the dynamical process of ERT imaging.
- Enhance the algorithm for image-quality improvement.
- Evaluate the Temporal TV algorithm, and investigate the potential applications.
- Carry out a feasibility study, and experimental validations of dynamical ERT imaging aiming at flow measurement applications using circular ERT sensor.
- Evaluate the performance of ERT Planar array sensors, and investigate the feasibility of the method by simulation and experiments.

1.3 Contributions

The main contributions of this work are the dynamical ERT applied with STTV, which is the first time that STTV has been used with ERT. Two pieces of this work have been published successfully in peer-reviewed journals. The first one evaluates the performance of STTV by comparing it with TOS, and shows the advantages of using a piecewise constant TV function in the time domain. The second work focuses on velocity measurement of a moving object via 2D/3D ERT and the cross correlation technique based on image reconstructions using the proposed STTV regularisation method.

The last piece of work is aimed at the subsurface ERT problem, which has not been developed upon much in previous works. It is a challenging topic as it is deals with the problem of OEIT, and also suffering from missing data, which results in a degradation of image quality more than in conventional close-domain 2D/3D ERT image reconstructions. SBTV is applied to solve this problem as a TV-based method potentially contributes to a better image quality. This work suggests that the performance of detecting target depth based on OEIT, and optimized reconstruction results are analysis based on suggested parameter selection method. This work is submitted to the IEEE sensor journal. Contributions can be listed as below：

- Developing STTV algorithm for dynamical ERT imaging
- investigating the performance of STTV
- proposing a velocity profile measurement method based on STTV
- Evaluating the performance of planar array ERT for depth detection

1.4 Thesis organization

The chapter arrangement of this thesis is organized with the following contents:

Chapter 2 introduces the basic theory of ERT, starting with the basic principles of Maxwell's Equations that are employed in ERT as basic functions for further descriptions and derivations of ERT mathematical models. In addition, different electrode models, the finite element method, and sensitivity distribution are briefly introduced. Moreover, the inverse problem of ERT is illustrated, where some algorithms for image reconstructions are reviewed. Quantitative index for image quality evaluation is demonstrated in the last section.

Chapter 3 is presented as a literature review chapter about multiphase flow. The background is introduced from a few angles, including definition, way of production, and specific situation in the practical industries regarding multiphase flow. In section 3.1, flow regimes of air-water flow and oil-water flow are summarised, and 3.2 presents some common flow parameters that are encountered in flow measurements. In addition, some proposed flow models are concluded, and each flow model that is frequently encountered

in literatures is demonstrated. The last section reviews literatures of flow measurement using ERT techniques in previous works and summarises it from several perspectives.

Chapter 4 proposes the spatial-temporal total variation (STTV) algorithm based on the Split Bregman method, which is designed to make contributions to improve the performance of dynamical visualization results of a moving target for 2D ERT. To evaluate the performance of STTV regularisation method, another temporal algorithm is employed for making comparisons. Spatial and temporal distributions and gradients of temporal imaging from both algorithms are defined and compared. For further illustration, the time response of dynamical imaging is proposed, and it is found that results using STTV response faster than TOS since STTV preserves the sharp edge of the object. This work was published in [33].

Chapter 5 extends the STTV algorithm into 3D. An experimental phantom is designed with 2 electrode rings for 3D ERT sensing. The purpose of this research is for the quantitative monitoring of a moving object by reconstructing 2D/3D dynamical images. By using cross-correlation between planes on the top and bottom rings, the average moving velocity of objects based on 2D/3D temporal ERT imaging is calculated and discussed. This work was published in [34].

Chapter 6 investigates the performance of volumetric ERT using planar array, aiming at exploring the interior information of a pipeline to solve the problem of poor spatial resolution on the axis-direction of 3D ERT using electrode rings. Split Bregman TV is been used for image reconstruction for improving the image quality, and the detected depth of the target was discussed. Results show that 3D ERT using planar array can improve spatial resolution within the detectable region. Although visualizations using planar array have limitations in distance, it can potentially be combined with ring-electrode model ERT and reflect more information of the pipeline.

Chapter 7 is a conclusion chapter with two sections. Section 1 summarises the contents involved in each chapter, including the conclusions of novel ideas, what has been conducted, results, and novel finding of the research. Based on these discoveries, potential applications are suggested, and future development, as well as further works using these findings, are proposed.

Chapter 2 EIT Principles

EIT is a newly emerging technique aimed at mapping cross-sectional images. In some literature, especially in industrial applications, the name of EIT has sometimes termed Electrical Resistance Tomography (ERT) if the reactive capacitive component of the impedance is negligible, and only the real-part is used as measured data. Due to the complexity of 'soft field', ERT is definitely a difficult technique. David S Holder stated the main difficulties of EIT in Chapter 1 of his book 'Electrical Impedance Tomography Methods, History and Applications' [35]. Above all, numerous equations relating to all pixels/voxels and measurements in an EIT system are required to be solved. In addition, the EIT inverse problem is an ill-posed problem that requires the development of a variety of regularisation algorithms, where well-posed means that it must satisfy that a unique solution exists regarding all admissible data, and the solution should vary with different data.

Different types of EIT/ERT reconstruction modalities have been used, including time-difference imaging, frequency-difference imaging [36] [37], and absolute imaging, or 2D and 3D EIT [38] [39] [40] imaging, depending on the dimensions of the image. Time-difference imaging produces images using the voltage difference Δv between the time interval t1 and t2. Normally, a frame of data would be used as a reference, or called background data, and another frame of data that made difference on conductivity distribution over Δv. Time-difference EIT imaging is widely used, for instance, in industrial applications, as a process tomographic method. In some of the medical or clinical applications, the background data is not available, so, frequency-difference methods are suitable for such cases. Tissue shows high resistivity and low capacitive. The frequency-difference imaging can represent the electric properties of tissues or cells, where difference-data is measured under different frequencies. Research demonstrates that EIT measurements for biological tissue can be made between 20Hz to 1MHz, and membranes of tissues impede current flow at low frequencies while high-frequency measurement is dependent on the liquids around cells [41]. Time-difference and frequency-difference imaging produce conductivity differences for visualization while the absolute EIT imaging solves the absolute conductivity distribution. Theoretically, absolute imaging is possible with an accurate enough forward modelling calculation as well as a reliable and precise measurement system [42]. However, initial

values of data, contact impedance, and physical factors can have a large influence and make it very difficult. Small errors in modelling lead to degrading image quality, and even losing valuable information.

Based on the requirements of various applications, image reconstruction approaches could also be classified as static imaging and dynamic imaging. It is obvious that that static imaging is for cases that the object remains still, and has been widely researched. Dynamic imaging is sometimes referred to as temporal imaging and is required in process tomography (PT). However, more unstable factors can be introduced when compared with static imaging, which can lead to blurring of the reconstructed results. There are some works that contribute to dynamic sense using temporal algorithms, which led to some improvements in the results [33] [43] [44] [33] [45] [46].

2.1 EIT hardware system

A hardware system may consist of a current source (one or more), voltage meters, a controller, and a switching network. Many EIT hardware systems have been developed for either researching purposes or commercial use, and vary in complexity of connection. In this section, some of these previous systems are reviewed.

Several versions of the Sheffield EIT system were developed from 1987 to 2000 [47] [48] [49]. All versions were designed with a single current source. The first version was produced in 1987, and called the Sheffield MK1 EIT system, which employed 16-electrode channels and a single option of operational frequency. Although an upgraded version appeared after two years, it only had a lighter weight and smaller body size, its function was relatively less interesting. The Sheffield MK2 system was invented in 1990, it had a lower frequency and was designed with digital technology instead of the analogue technique in older versions. In the following decade, the MK3 and MK3.5 systems were developed, and for both versions, more choices of frequency were allowed. MK3 has 8 frequencies varying from 9.6 KHz to 1.2 MHz, and 30 operation frequencies between 2 KHz and 1.6 MHz.

Table 2.1: Sheffield EIT system specifications

Sheffield EIT system versions	Time	Number of electrodes	data acquisition protocol	Frequency	Technique	Current source
MK1 EIT system	1987	**16**	**adjacent drive/receive**	**50 KHz**	**Analogue**	**single**
Space/portable	1989	**16**	**adjacent drive/receive**	**50 KHz**	**Analogue**	**single**
MK2 EIT system	**1990**	**16**	**adjacent drive/receive**	**< 50KHz**	**Digital**	**single**
MK3 EIT system	**1993**	**16**	**Interlaced**	**8:9.6KHz-1.2MHz**	**Analogue**	**single**
MK3.5 EIT system	**2000**	**8**	**adjacent drive/receive**	**30:2KHz-1.6MHz**	**Digital**	**single**

The Oxford Group designed several systems with multiple-sources, including OXPACT-II [50], OXBACT-III [51], where simultaneous current excitation is operated via multiple current sources. OXPACT- II was developed with 32 driving electrodes and 32 measuring electrodes under the control of a microcomputer. The collection speed was unsatisfactory for applications as it was designed for 'vitro studies', and phantom tests showed that images could only be produced by small conductivity contrast targets. OXBACT- III is designed as a real-time multiple-drive adaptive system, with a real-time rate of 25 frames/s. The upgraded system was developed for clinical purposes, and the multi-frequency is another improvement over the OXPACT-II.

Table 2.2: Oxford EIT system development

Oxford EIT system versions	Time	Number of electrodes	Frequency	Current source
OXPACT-II	1991	64	9.6KHz	Multiple current source
OXPACT-III	1994	64	10-160KHz	Multiple current source

Kyung Hee University created a 16-channel multi-frequency EIT system called KHU Mark I system in 2007 [52], designed with a single current source and multiple voltage measurement devices. The operational frequency could be chosen between 10 KHz and 500 KHz. Experiments have been carried out with a 2-D phantom to produce time-difference images under different chosen frequencies. An upgraded new system KHU Mark II was proposed after a few years, which was designed as a fully-parallel multi-frequency system, based on its Impedance Measurement Module (IMM) [53] [54]. This new system improved the data acquisition rate to satisfy the requirements of a faster speed in practice, in addition, flexible electrode configurations and multiple independent operation sources were also included in the new system features.

Table 2.3: KHU EIT system development

Kyung Hee EIT system versions	Number of electrodes	Frequency
KHU Mark I	16/32/64	10HKz-500HKz
KHU Mark II	16/32/40	10Hz-1MHz

2.2 EIT data acquisition

In ERT, the boundary voltage data measurement is required in order to recover the conductivity map of the test target in the medium. The data measurement strategy of ERT includes current driving and data acquisition via the ERT hardware system. Driving patterns can be classified into two types depending on the type of sources [55]. Multi-source systems are termed Optimal Patterns, and ones using single-source are known as Bipolar Patterns. Multiple current sources are working simultaneously for current driving, and the resulting voltages are measured via all the remaining electrodes, whilst a single-current source is applied to a pair of current-driving electrodes in Bipolar Patterns, and the resulting potentials are taken from all electrodes. Optimal patterns require too many current sources that are not possible in practice for a large electrode-number ERT system. In comparison, single-source patterns are more commonly used, and some conventional methods have been suggested, such as, the neighboring method (adjacent method), opposite method, and cross method.

2.2.1 Adjacent method

The most common measurement method is the adjacent method, where the data is collected on neighboring pairs of electrodes. In terms of a 16-electrode sensor, the current is injected into an adjacent pair of electrodes, and the voltage could be measured via the remaining adjacent electrode pairs. For example, the first current is applied to (1, 2), then the resultant voltages are measured on (3, 4), (4, 5)… (15, 16). The following current injection is addressed on the ’ neighbor’ (2, 3), and the way of data collection is identical. A whole image corresponds to a cycle of the data collection process, where the current is applied to (1, 2), (2, 3)… (16, 1). The measured data via the driving-electrode are normally ignored and would be removed if the data collection system cannot skip them. For a 16-electrode sensor, 208 independent measurements (16×(16-3)) are taken to reconstruct an image.

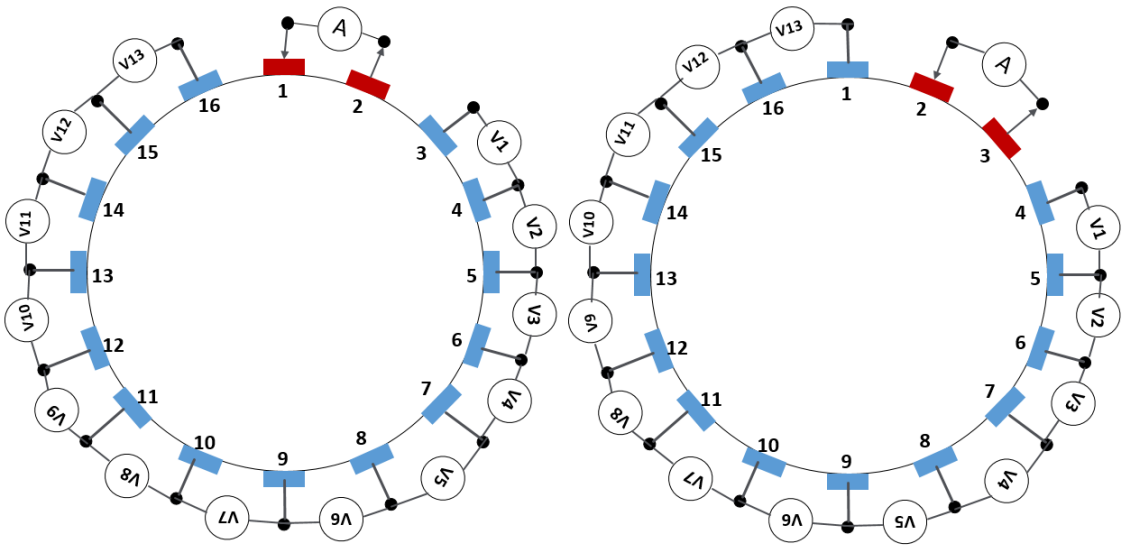

(a) (b)

Figure 2.1: Illustration of the adjacent method on a 2D circular sensor with a 16-electrode ring. (a) Measurements with current injected via 1-2. (b) Measurements with current injected via 2-3.

2.2.2 Opposite method

The approach using opposite-placed electrode pairs, such as, (1, 9), (2, 10), (3, 11), etc., for current driving is named the opposite method. A reference electrode is chosen for voltage measurement during data acquisition. For a current injected via (1, 9), electrode no.2 becomes the reference electrode, and voltages between (2, 3), (2, 4), (2, 5)… (2, 16) are collected as measurement data, where voltages between the reference electrode and current driving electrodes, (2, 1) and (2, 9), are removed. For each current excitation, 13 voltages are measured and collected, and 108 individual measurements from 8 sets of current driving (half of the data from 16 current injections are identical).

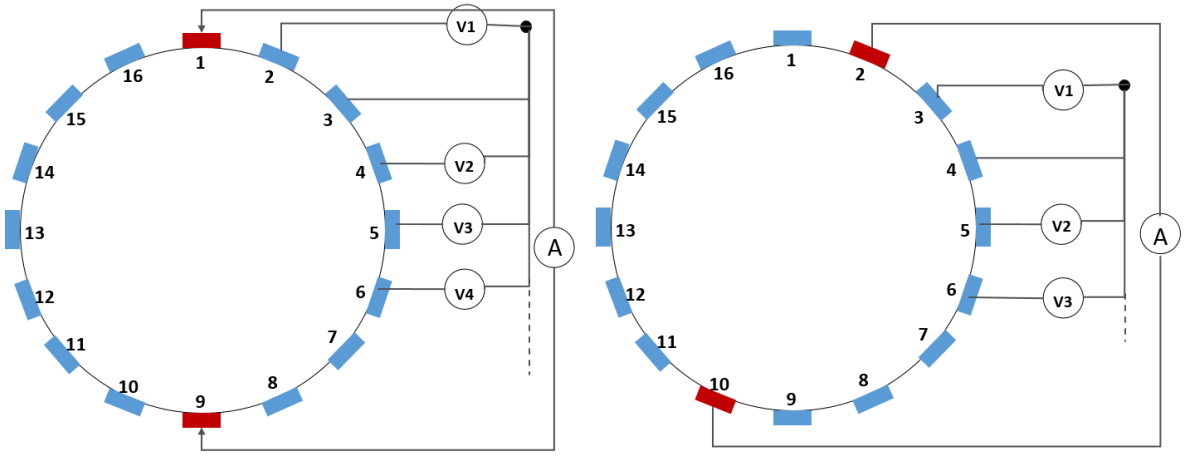

Figure 2.2: Figure of the opposite current pattern for a 2D circular sensor with a 16-electrode ring. (a) Measurements with current injected via 1-9. (b) Measurements with current injected via 2-10.

2.2.3 Cross method

Two adjacent electrodes are selected to be reference electrodes for current driving and voltage measuring respectively. The figure below shows the situation of data collection for a 16-electrode ERT model using electrode 1 as the current injection, and electrode 2 for measurement. Thirteen voltages via (2, 4), (2, 5), (2, 6) … (2, 16) are recorded when current is driving from (1, 3). In addition, further current excitations are engaged via (1, 5), (1, 7), (1, 9), (1, 11), (1, 13) and (1, 15), and procedure of voltage measurement is identical. In total, 91 individual measurements are taken from 7 sets of current driving.

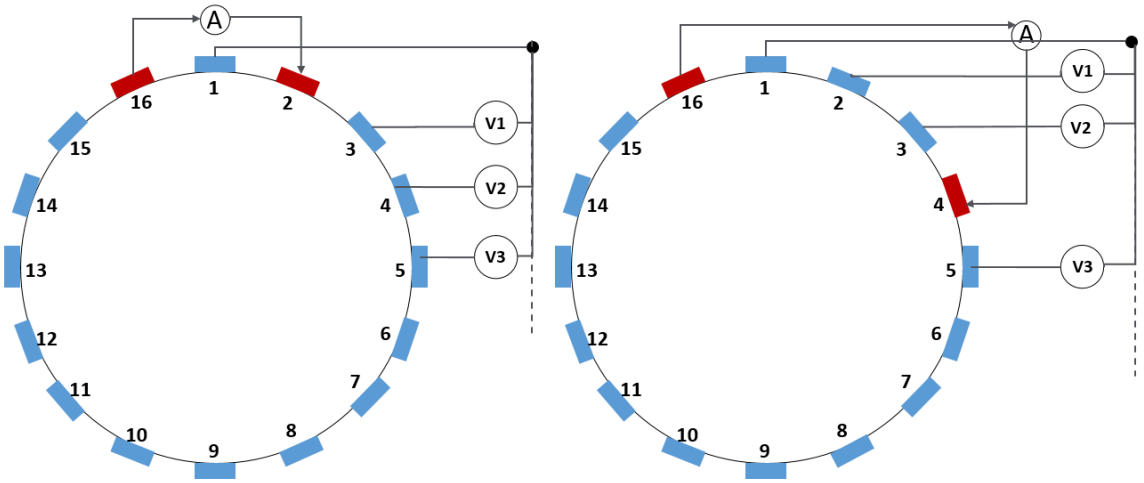

(a) (b)

Figure 2.3: Figure of the cross method current pattern for a 2D circular sensor with a 16-electrode ring. (a) Measurements with current injected via 16-2. (b) Measurements with current injected via 16-4.

N J Avis and D C Barber represents their works of comparing driving configurations of adjacent pattern, opposite pattern and cross pattern, and confirmed that the adjacent pattern performs the best [56]. Researchers argue that the adjacent patterns provide the best spatial resolution on reconstructed images, but also yields a poor signal-to-noise-ratio (SNR) on data [57]. Some literature regarding the performance of different single-source driving patterns is also proposed [58], [59]. For 3D ERT imaging, different data acquisition methods on multiple rings with various connections, such as, Zigzag, Square, are also proposed [60], where J. Wagenaar and A. Adler proposed literature for evaluating the performance of volumetric ERT with two planes, by comparing several electrode placement patterns. Note that these suggested methods of connections for circular twin-plane sensor would only affect the electrode numbering arrangement, and the neighboring method is utilized for all the different electrode connection methods.

2.3 Maxwell's Equations

The starting point of ERT Theory should begin with Maxwell's Equations [61]. Electric field $\vec{E}$ and magnetic field $\vec{H}$ are involved in the ERT system as a 'soft field'. Above all, Faraday's law suggests the variation of magnetic flux generates the electric field. In the static field of a conventional ERT system, the induced electric field in an enclosed path depends on the change of magnetic induction $\vec{B}$, which is given by the equation:

$$\nabla \times \vec{E} = -\frac{\partial \vec{B}}{\partial t} \qquad (2.1)$$

Coulomb's law is also called the Total Current Law in some books, as it states the relationship between total current and magnetic field, which is expanded from Ampere's circuital Law. The total electric current is composed of conducting current density J_c and displacement current density, given by $J_D = \frac{\partial \vec{D}}{\partial t}$ ($\vec{D}$ donates to the electric displacement field). The conducting current is the general current going through the wire or other conductor. For the case of time-varying field presented in dielectric materials, the displacement current is taken into account in the total electric current relating to the polarisation effect. The current is the integral of current density on an enclosed surface **S,** so we have:

$$I_{total} = \oiint J_c \cdot dS + \iint J_D \cdot dS \qquad (2.2)$$

Mathematically, Coulomb's law is described by the following equation:

$$\oint \vec{H} \cdot dl = I_{total} \qquad (2.3)$$

In differential form:

$$\nabla \times \vec{H} = J_c + \frac{\partial \vec{D}}{\partial t} \qquad (2.4)$$

In an electromagnetic field, the following equations are also valid, where ε and μ contribute to permittivity and the permeability of space:

$$\vec{D} = \varepsilon\vec{E} \tag{2.5}$$

$$\vec{B} = \mu\vec{H} \tag{2.6}$$

$$J_c = \sigma\vec{E} \tag{2.7}$$

Time-harmonic Maxwell's equations introduce time and frequency in equations, where electric field and magnetic field in time can be written as:

$$E = Ee^{j2\pi ft} \tag{2.8}$$

$$B = Be^{j2\pi ft} \tag{2.9}$$

Maxwell's equations in time are rewritten as:

$$\nabla \times \vec{E} = -j\omega\mu\vec{H} \tag{2.10}$$

$$\nabla \times \vec{H} = J_s + (\sigma + j\omega\varepsilon)\vec{E} \tag{2.11}$$

2.4 Forward problem

The main questions of ERT are solving the Forward Problem and Inverse Problem. The Forward Problem is the process looking for potential distributions with an assumed conductivity distribution. Jacobian calculation also results from this step based on FEM solver. This is usually implemented by conducting simulation modelling with PC, and EIDORS software has been applied for solving the Forward Problem of ERT. The Inverse Problem is reconstructing the image by working out the conductivity distribution based on the potential distributions and Jacobian matrix, and regularisation methods are usually required for optimizing such an ill-posed problem. The flow chart of ERT is shown below:

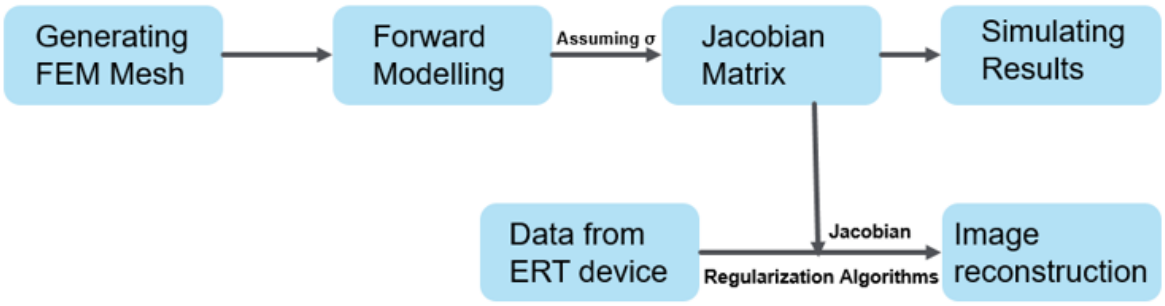

Figure 2.4: Forward problem and inverse problem of ERT

2.4.1 Mathematically setting-up of ERT

The Forward Problem of ERT is solving the electric potential with an assumed conductivity distribution σ. For most EIT problems, moderate frequencies are applied to the conductive region, and in this thesis, experiments are around frequencies of 10 KHz to 200 KHz, which can be considered as low-frequency ERT. For such quasi-static electromagnetic fields, the terms multiplied by $j\omega\mu$ or $j\omega\varepsilon$ can be seen as 0 and neglected as such frequencies would have a very small influence. Such situations mean it is under a nearly constant field, and the DC case is usually considered as a simplification of the mathematical setup.

In ERT, equations are formed with:

$$\nabla \times \vec{E} = 0 \tag{2.12}$$

$$\nabla \cdot J = 0 \tag{2.13}$$

$$\vec{E} = -\nabla\varphi \tag{2.14}$$

$$\nabla \times \vec{H} = J_s + (\sigma + j\omega\varepsilon)\vec{E} \tag{2.15}$$

In equation (2.15), $(\sigma + j\omega\varepsilon)\vec{E}$ is donating the conducting current density and approximated to be $\sigma\vec{E}$ due to low-frequency. The interior region typically has no current source, which brings J_s to 0. Hence, the equation (2.15) can be rewritten as:

$$\nabla \times \vec{H} = J = \sigma\vec{E} \tag{2.16}$$

A combination of the above equations gives a dominating equation of ERT [7]:

$$\nabla \cdot \sigma \nabla \varphi = 0 \tag{2.17}$$

Boundary conditions of ERT are introduced on the boundary of the region by an outward normal vector $\overrightarrow{n}$. Assuming current density j on the boundary $\partial\Omega$:

$$j = \sigma \nabla \varphi \cdot \vec{\mathrm{n}} = \sigma \frac{\partial \varphi}{\partial \vec{n}} \tag{2.18}$$

2.4.2 Electrode model

Various electrode models have been investigated in previous research, including the continuum model, gap model, shunt model, and complete electrode model [62]. The primary assumption has been made on the electrode model is Continuum model, where a continuous current function was suggested, and that means no gap between electrodes. Obviously, this assumption is far from the case in practice. The Gap model considers the electrode gap, and the current density remains 0 in the gap. The mathematical expression of the Gap model with electrode area A is given by:

$$j = \begin{cases} \frac{I_N}{A}, & \mathrm{x} \in e_l \\ 0 \quad , & x \in \partial\Omega \text{ and } x \notin e_l \end{cases} \tag{2.19}$$

However, it is not comprehensive that the 'shunting effect' of metal electrodes is neglected, and would lead to an overestimation of the resistivity.

The shunt model made some improvements, and the constant potential on metal electrodes has been assumed as a constraint.

The current on electrodes is composed of current density over electrode area:

$$I_l = \int \sigma \frac{\partial \varphi}{\partial \vec{n}} \cdot dS \quad \mathrm{x} \in e_l, \;\; l = 1, 2, \ldots, N \tag{2.20}$$

$$V_l = \mathrm{u} = \mathrm{constant} \tag{2.21}$$

Since electrodes have to be in contact with the medium in ERT, effects caused by contact impedance have to be considered in an electrode model. The contact-impedance effect is

especially critical in absolute image reconstruction, however, it is normally considered as constant in difference imaging, and measurement data is only related to conductivity re-distribution over the ERT conductive domain. Such considerations are under ideal conditions, however, the conditions of metal electrodes can change over time [63]. The Complete Electrode Model accounts for the shunting effect and generation of contact impedance, which was introduced in [64] and is commonly utilized in the ERT forward model. Voltage drop would produce on contact impedance z_l between the l^{th} electrode and the region:

$$\mathrm{u} + z_l . \sigma \frac{\partial u}{\partial \vec{n}} = V_l \quad \mathrm{x} \in e_l, \qquad l = 1, 2, \dots, N \tag{2.22}$$

Zero current density would be applied to that area that off electrodes on the boundary:

$$\sigma \frac{\partial u}{\partial \vec{n}} = 0 \quad , x \in \partial\Omega, \text{and } x \notin e_l \tag{2.23}$$

In addition, conservation of charge, as well as Kirchhoff's law on the electrode-ring, must hold, where we have:

$$\sum_{l=1}^{N} I_l = 0 \quad l = 1, 2, \dots, N \tag{2.24}$$

$$\sum_{l=1}^{N} V_l = 0 \quad l = 1, 2, \dots, N \tag{2.25}$$

Experimental measurements have been made on the complete electrode model for predicting, and existence and uniqueness have been proved in [62].

2.4.3 Finite element method

The Forward problem is solving the potential distribution inside the ERT region based on known conductivity. Practical mediums of ERT are continuous, and doing element subdivision is a conventional method such that the region is composed with lots of small elements and potential distribution is solved on these elements. The finite element method (FEM) is commonly employed as a forward solver for regional discretion, and is applicable

for inhomogeneous distribution. FEM 2D mesh is usually produced with lots of connecting triangles/rectangles, while 3D mesh uses tetrahedrons as elements. Elements are connected via nodes, where electric potential on joint nodes must be equivalent. EIDORS is a useful software for solving the forward problem, where it computes the potentials based on the FEM solver by simply defining the geometry/size of the medium, size/number of electrodes, and assumed conductivity values on the background and the target. The Jacobian matrix can be calculated with output potential distributions from FEM. Figure 2.5 displays a 2D FEM mesh generated by EIDORS, where a circular model with 16 plate electrodes was applied for forward-modelling. In this thesis, all of the forward modelling is based on EIDORS software.

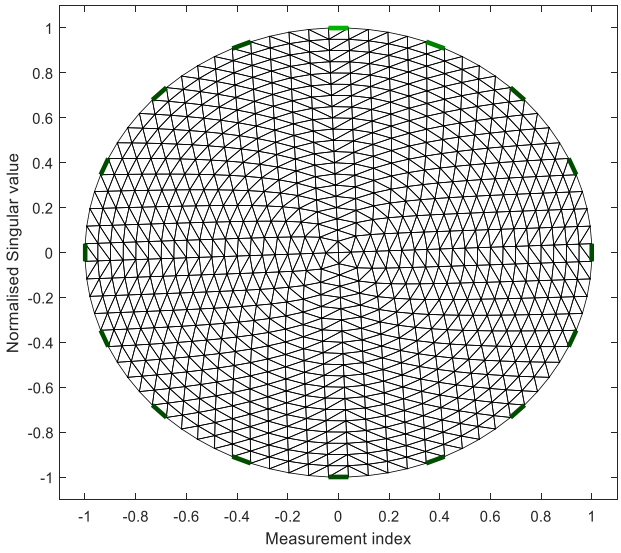

Figure 2.5: 2D mesh generated using EIDORS [65]

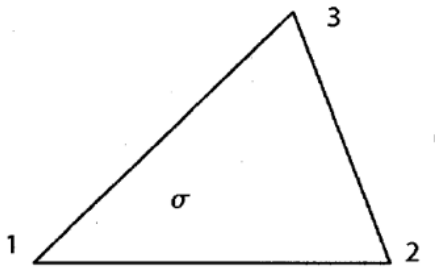

Figure 2.6: triangle element from 2D FEM mesh

Assuming a triangle element in figure 2.6 is one of the FEM elements taken from a 2D FEM mesh with nodes numbered node 1, node 2 and node 3. A typical way is introducing a linear interpolation function [61] [65]. Giving (x1, y1), (x2, y2) and (x3, y3) to each node with corresponding potentials φ_1 , φ_2 and φ_3 . The potentials can be given by the linear approximated function:

$$\varphi(x, y) = a + bx + cy \tag{2.26}$$

Regarding 3 triangle nodes,

$$\begin{bmatrix} 1 & x_1 & y_1 \\ 1 & x_2 & y_2 \\ 1 & x_3 & y_3 \end{bmatrix} \begin{bmatrix} a \\ b \\ c \end{bmatrix} = \begin{bmatrix} \varphi_1 \\ \varphi_2 \\ \varphi_3 \end{bmatrix} \tag{2.27}$$

Now we expect to solve three coefficients a, b, c in the equation above, and take an inversion:

$$\begin{bmatrix} a \\ b \\ c \end{bmatrix} = \begin{bmatrix} 1 & x_1 & y_1 \\ 1 & x_2 & y_2 \\ 1 & x_3 & y_3 \end{bmatrix}^{-1} \begin{bmatrix} \varphi_1 \\ \varphi_2 \\ \varphi_3 \end{bmatrix} \tag{2.28}$$

The potential function $\varphi(x, y)$ could be reproduced on the left-hand side of the equation by multiplying back $[1 \quad x \quad y]$ to both sides:

$$\varphi(x, y) = [1 \quad x \quad y] \begin{bmatrix} 1 & x_1 & y_1 \\ 1 & x_2 & y_2 \\ 1 & x_3 & y_3 \end{bmatrix}^{-1} \begin{bmatrix} \varphi_1 \\ \varphi_2 \\ \varphi_3 \end{bmatrix} \tag{2.29}$$

Let $[N_i] = [1 \quad x \quad y] \begin{bmatrix} 1 & x_1 & y_1 \\ 1 & x_2 & y_2 \\ 1 & x_3 & y_3 \end{bmatrix}^{-1}$ and $[\varphi_i] = \begin{bmatrix} \varphi_1 \\ \varphi_2 \\ \varphi_3 \end{bmatrix}$

$$\varphi(x, y) = \sum_{i=1}^{3} N_i \cdot \varphi_i \tag{2.30}$$

$[N_i]$ could also be expanded to be related to spatial coordinates (x, y) by introducing the inversed matrix. Rename the inversed matrix to a 3-by-3 matrix $[\mathrm{Q}_{ij}]$ for description, where each element of $[\mathrm{Q}_{ij}]$ are composed with coordinates of nodes:

$$[N_i] = Q_{1i} + xQ_{2i} + yQ_{3i} \tag{2.31}$$

$$\varphi(x, y) = \varphi_i \cdot (Q_{1i} + xQ_{2i} + yQ_{3i}) \tag{2.32}$$

It obvious to observe that the equation represents the expression relating nodal potentials φ_i with interior potentials $\varphi(x, y)$ of a FEM element.

$$\varphi(x_i, y_i) = \varphi_i = N_i(x_i, y_i)\varphi_i + N_j(x_j, y_j)\varphi_j + N_k(x_k, y_k)\varphi_k \tag{2.33}$$

Indicating that

$$N_i(x_i, y_i) = 1, N_j(x_j, y_j) = 0, N_k(x_k, y_k) = 0$$

Based on such derivation, it can be concluded that

$$N_i(x_j, y_j) = \begin{cases} 1, & \text{if i} = \text{j} \\ 0, & \text{if i} \neq \text{j} \end{cases} \tag{2.34}$$

For 3D, the FEM is composed of tetrahedral elements, and the approximated 2D linear equation (2.26) can be extended to 3D, where

$$\varphi(x, y, z) = a + bx + cy + dz \tag{2.35}$$

Derivation of the linear interpolation function has a similar procedure as 2D, and the shape function combined potentials of 4 vertexes of a single tetrahedral element in 3D FEM takes the form:

$$\varphi(x, y, z) = \sum_{i=1}^{4} N_i \cdot \varphi_i \tag{2.36}$$

Where the equation (2.34) is valid for four vertices.

Approximation of the potential over the whole medium is a collection of FEM elements. Assuming that in ERT medium Ω, we have N nodes composed with a vertex of elements, the approximation can be represented by:

$$\phi_{FEM} = \sum_{i=1}^{\mathrm{N}} \phi_i \, N_i \tag{2.37}$$

A non-differential function ϕ_i cannot satisfy the formulation of $\sigma\nabla^2\phi = 0$. Instead, a function A is involved by multiplying this formulation and integral over the medium to make a weak form:

$$\int A \cdot \nabla \cdot (\sigma \nabla \phi_{FEM}) = 0 \tag{2.38}$$

Applying Vector Identities, the equation is equivalent to:

$$\int \nabla(A \cdot \sigma \nabla \phi_{FEM})\, d\Omega - \int \sigma \nabla A \cdot \nabla \phi_{FEM}\, d\Omega = 0 \tag{2.39}$$

Introducing function $A = \sum_{j=1}^{N} \phi_j\, N_j$ to the first term and applying divergence theorem,

$$\int \nabla(A \cdot \sigma \nabla \phi_{FEM})\, d\Omega = \sum_{i=1}^{N} \phi_i \sum_{j=1}^{N} \phi_j \int \sigma \nabla N_i \cdot \nabla N_i \, \mathrm{d}\Omega \tag{2.40}$$

And the second term is combined with CEM,

$$\int (\sigma \nabla A \cdot \nabla \phi_{FEM}) d\Omega = \int A \cdot \sigma \nabla \phi_{FEM} \cdot \vec{n}\, dS \tag{2.41}$$

$$\sigma \nabla \phi_{FEM} \cdot \vec{n} = \sigma \frac{\partial \phi_{FEM}}{\partial \vec{n}} \tag{2.42}$$

$$\sigma \frac{\partial \phi_{FEM}}{\partial \vec{n}} = \frac{1}{Z_{elec}} (V_l - \phi_{FEM}) \tag{2.43}$$

The total current on electrodes is written as integrals of current density over electrodes. For current on the l^{th} electrode with an area of contact impedance E_l,

$$I_l = \int \frac{1}{Z_{elec}} (V_l - \phi_{FEM})\, dE_l \tag{2.44}$$

$$= \frac{E_l}{Z_{elec}} \cdot V_l - \frac{1}{Z_{elec}} \cdot \sum_{\mathrm{i}=1}^{N} N_i \cdot \int \phi_i dE_l \tag{2.45}$$

The entire FEM system equation is formed by combining the equations above

$$\begin{bmatrix} \alpha & \beta \\ \beta' & \gamma \end{bmatrix} \cdot \begin{bmatrix} \phi \\ V_l \end{bmatrix} = \begin{bmatrix} 0 \\ I \end{bmatrix} \tag{2.46}$$

Where in a FEM system matrix,

$$\alpha_{ij} = \int \sigma \cdot \nabla \mathrm{N}_i \cdot \nabla \mathrm{N}_j d\Omega + \int \frac{1}{Z_{elec}} \left(\mathrm{N}_i \cdot \mathrm{N}_j\right) dS \tag{2.47}$$

$$\beta_{ij} = -\int \frac{1}{Z_{elec}} \phi_j dS \tag{2.48}$$

$$\beta'_{ij} = -\int \mathrm{N}_j dS \tag{2.49}$$

$$\gamma = \begin{bmatrix} \frac{\mathrm{E_l}}{\mathrm{Z_{elec}}} & \cdots & 0 \\ \vdots & \ddots & \vdots \\ 0 & \cdots & \frac{\mathrm{E_l}}{\mathrm{Z_{elec}}} \end{bmatrix} \tag{2.50}$$

And in the system equation,

$$[\phi] = \begin{bmatrix} \phi_1 \\ \vdots \\ \phi_{\mathrm{N}} \end{bmatrix} \qquad [V_l] = \begin{bmatrix} V_1 \\ \vdots \\ V_L \end{bmatrix} \qquad [I] = \begin{bmatrix} \mathrm{I}_1 \\ \vdots \\ \mathrm{I}_L \end{bmatrix} \qquad [0] = \begin{bmatrix} 0 \\ \vdots \\ 0 \end{bmatrix}$$

2.4.4 Jacobian matrix

The Jacobian matrix is widely used for solving optimization problems, and is introduced in various algorithms. Some of the ERT related literature also called it a sensitivity matrix. The Jacobian matrix is a sparse matrix where lots of zero elements are enrolled, which is combined with first-order derivatives, the Jacobian matrix is calculated by partial derivatives of voltages with respect to conductivity. A common Jacobian calculation is the perturbation method, where a perturbation on the conductivity is taken with $\sigma + \delta\sigma$, yielding perturbations on potentials $\phi + \delta\phi$ and measurements of voltage $V_l + \delta V_l$. Literatures [66] and [67] presented derivations of the Jacobian based on perturbations in power.

For the k^{th} element with a fixed current injected, assuming a potential of d^{th} driving pattern and m^{th} measurement patterns are $\phi(I^d)$ and $\phi(I^m)$. The expression of the Jacobian is given by:

$$J_{kdm} = \frac{\partial V_{dm}}{\partial \sigma_k} = -\int \nabla\phi(I^d) \cdot \nabla\phi(I^m) dV \qquad \text{on pixel/voxel } k \tag{2.51}$$

In ERT, the conductivity change $\Delta\sigma$ can be determined based on measurements using the Jacobian matrix, and the calculation of the Jacobian is normally implemented in forward modelling using simulated data.

2.5 Inverse problem

The Inverse problem of ERT is aimed at image reconstruction based on the Jacobian matrix, where conductivity distribution is expected to be determined using measured boundary data, solving x for a given $A \cdot x = b$. For the case of ERT, A and b are Jacobian matrix and measurement data, and we wish to determine conductivity distribution x. The least-square method is commonly conducted to optimize, so that the difference $A \cdot x$ and b are to be as close as possible, however this solution is unstable, and even non-unique or non-existent. For solving the conductivity distribution, the worst case is that the Jacobian matrix is a singular matrix resulting non-invisible. The ill-posed inverse problem results in small perturbations in voltage measurements leading to a large error in results. To overcome such a situation, people use regularisations to impose additional information or constrain for stabilization. Linear back projection (LBP) is an early-proposed algorithm [68], where the inversed Jacobian J^{-1} is approximated by its transpose J^T to make the calculation, consequently, poor image-quality visualizations were created. However, priori information can be introduced as 'smoothness' for regularising this problem. Regularisation of ERT is an optimisation problem, and many algorithms, including Newton One Step Error Reconstruction (NOSER) [69], Tikhonov regularisation [70], Laplacian regularisation [71], the Landweber Iteration method [72], and Total variation methods [73] [74] [75], have been developed to be utilized in tomographic techniques.

Regularisation methods are classified as l2-norm or l1-norm methods. Most traditional algorithms, such as Tikhonov, are minimizing l2-norm, also known as the least square method. L2-norm is presented mathematically by a sum of squares. A general form of an underdetermined problem of ERT inverse problem is solving optimised residual error, and a penalty term is added as additional information. Conventional algorithms impose a penalty term with an l2-norm, where a smoothness factor is introduced for linearizing the ill-posed problem. TV regularisations are known as l1-norm methods, where l1-norm means the sum

of absolute values. Penalty terms of TV algorithms use the l1-norm for optimizations without smoothing aiming at discontinuous profiling via non-linear regularisation [76], which places more effort into preserving the sharp boundary of the reconstructed object.

In this thesis, the main contributions are conducted using total variation regularisations. Traditional regularisation methods introduce a differential regularisation term in the l2-norm as imposed prior information, and regularisation parameters can adjust solutions of the ERT inverse problem. Another type of regularisation function known as total variation is very popular since it was first introduced in [77] by Rudin *et al.* Earlier literature has shown that TV can contribute to good image quality with noise removal and image restoration [78]. TV has been applied to various imaging techniques for solving the inverse problem due to its capability of preserving the edge of the monitored target [79] [80]. In practical situations, most emerged case is that there are discontinuities in conductivity. Such an ability is especially useful for cases when the boundary information is important, and imposing smoothness may lead to bias in the true solution. For multiphase flow visualizations, TV contributes to the display and identifies the sharp change between different phases, i.e. interfaces between a continuous phase and dispersed phase can be monitored properly, if TV regularization can be applied to industries successfully. Above all, sharp images mean less position error and blurs, hence resulting in high-quality reconstructions, which will benefit detection purposes where the target is required to be localized. In addition, a sharp change of phases can also help in achieving other measurement purposes. One example is cases where flow regime identification is critical, and a sharp interface between phases can improve the image quality of flow visualization processes. For the cases of measuring phase concentration based on an image, a sharp boundary of the dispersed phase can allow an upgrade in the accuracy of the measurement of phase fraction. However, L2-norm based regularisations suffer from blurring since they are introduced prior to the information leading to smoothness, which makes it difficult for estimations of interface or boundary of the targets to be imaged. Blurred images cannot satisfy the precision required for image-based quantitative parameter measurements. Various methods have been proposed to solve TV formulations [75] [81], e.g. the primal and dual interior point method (PDIPM) [82], the linearized alternating direction method of multipliers (LADMM), and spatially adaptive total variation [73]. In particular, Split Bregman (SB) TV was proposed in 2009 [74] and is

capable of solving non-differentiable problems efficiently with a fast convergence rate, therefore it has received much attention. Comparison works suggest LADMM suffers from low resolution but has a fast computational time since it avoids second-order derivative calculations, and PDIPM introduces a smoothness parameter hence it has lower contrast. SB is recommended due to its high spatial resolution and faster convergence rate.

In this section, some regularisation methods regarding ERT static and dynamical imaging are introduced, where Tikhonov and Split Bregman TV (SBTV) are presented as spatial regularisation algorithms, while spatial-temporal TV (STTV) and Temporal one-step (TOS) algorithms are introduced as temporal regularisations dealing with dynamical imaging. Results from these algorithms are presented and discussed in the following few chapters.

2.5.1 Tikhonov regularization

Tikhonov regularisation is a popular method for solving the ill-posed inverse problem by introducing additional information. In the ERT Inverse problem, we wish to solve conductivity based on potentials, where it is approximated as a linear problem. The linear system of ERT is given by

$$J \cdot \sigma + error = u \tag{2.52}$$

Note that this is difference imaging, and the conductivity σ is given by $\sigma = \sigma_1 - \sigma_{background}$. This equation cannot be solved directly as it is ill-posed, and the noise or error of images is unavoidable as it can be imposed via many aspects, but it expected to make both sides of the equation to be as close as possible using optimizations. The residual error is minimized in order to make the solution as close as possible to the true value. In the ERT inverse problem,

$$x = argmin_{\sigma} \|J\sigma - u\|_2^2 \tag{2.53}$$

Tikhonov regularization imposes additional information for solving the ill-posed ERT inverse problem [70]. A penalty term with an l2-norm $\alpha\|\Delta\sigma\|^2$ is introduced for minimisation and solving optimization together. The general form of the standard Tikhonov formulation can be written as,

$$\underset{\sigma}{\operatorname{argmin}}\{\|J\sigma - u\|_2^2 + \alpha\|\Delta\sigma\|^2\} \tag{2.54}$$

For solving a minimization equation, let the first-order derivative of the Tikhonov function with respect to σ equal zero, and the solution of conductivity change is derived by the following steps.

$$\frac{\partial}{\partial(\sigma)}\left((J\cdot\sigma-u)\cdot(J\cdot\sigma-u)^T+\alpha\sigma\cdot\sigma^T\right)=0 \tag{2.55}$$

$$2J\cdot J^T-2Ju+2\alpha\sigma=0 \tag{2.56}$$

$$\sigma=(J^TJ+\alpha\mathrm{I})^{-1}.J^T\,u \tag{2.57}$$

Where J is Jacobian matrix, and σ and u are conductivity difference and potential difference respectively. α denotes the regularisation parameter, and it is referred to as an identity matrix.

2.5.2 Split Bregman Total variation

Total variation (TV) regularisation employs functions based on l_1-norm. Literature reports that the utilization of TV can contribute to a good image quality when solving the inverse problem. Traditional regularisation methods that impose 'smoothing' would result in blurring, whilst the TV function preserves discontinuity and reconstructs images with a non-smoothing reconstruction technique. TV is implemented by carrying out minimizations based on l1-norm, which calculates the total amplitude change on an objective function. The TV function with ERT imaging is defined as:

$$\mathrm{TV}(\sigma)=\int|\nabla\sigma|\,d\Omega \tag{2.58}$$

In the ERT inverse problem, TV is imposed as a penalty term and is formulated to solve:

$$\sigma=argmin_{\Delta\sigma}\|\mathrm{J}\sigma-u\|_2^2+\alpha\mathrm{TV}(\sigma) \tag{2.59}$$

Compared with L2-norm regularisations, a TV solution is relatively hard to implement while the former benefits from a differentiable function. Several approaches have been proposed for solving TV. Z Zhou and their group reported comparison works among PDIPM, SB and LADMM TV functions with Tikhonov regularisation. They suggested that TV regularisations lead to greater improvements in reconstruction results over l2-regularisation, and SBTV

shows a good performance in accuracy and convergence rate [75]. The Split Bergman method was first proposed by Osher [74], the constrained optimization problem of ERT is:

$$\sigma = argmin_{\sigma}\|\nabla\sigma\|_1 \;\; s.t. \|J\sigma - u\|_2^2 < \delta \tag{2.60}$$

TV function $\|\nabla\sigma\|_1$ is non-differentiable, and using traditional approaches would be computationally expensive. Therefore, TV function was replaced using Bregman distance. Based on literatures [79] [83] [80], mathematical derivations of SBTV start by defining a Bregman distance. Imaging that with each step, the solution is closer to the expected σ using a minimisation of such a 'distance'. The unconstrained optimising problem is rewritten as:

$$\sigma^{k+1} = argmin_{\sigma,d} D(\sigma, \sigma^k) + \frac{\beta}{2}\|J\sigma - u\|_2^2 \tag{2.61}$$

$$D(\sigma, \sigma^k) = \sigma - \sigma^k - < s^k, \sigma - \sigma^k > \tag{2.62}$$

The term $D(\sigma, \sigma^k)$ indicates the Bregman distance between optimal conductivity difference σ and k^{th} solution σ^k, where in the equation (2.62) <,> means the scalar product, and s denotes the sub-gradient of TV functional at k. Then the equation is modified to:

$$\sigma^{k+1} = argmin_{\sigma}\|\nabla\Delta\sigma\|_1 - < s^k, \sigma - \sigma^k > \; + \frac{\beta}{2}\|J\sigma - u\|_2^2 \tag{2.63}$$

$$s^{k+1} = s^k - \beta J^T(J\sigma^{k+1} - u) \tag{2.64}$$

Osher suggested that since J is linear, the equations above could be simplified to:

$$\sigma^{k+1} = argmin_{\sigma}\|\nabla\sigma\|_1 + \frac{\beta}{2}\|J\sigma - u^k\|_2^2 \tag{2.65}$$

$$u^{k+1} = u^k + u - J\sigma^k \tag{2.66}$$

The Split Bregman method introduces an auxiliary variable d such that $l1$ and $l2$ are decoupled. The constrained problem is framed as:

$$\sigma = argmin_{\sigma,d}\left\{\frac{\mu}{2}\|J\sigma - u\|_2^2 + \alpha\|d\|_1\right\} \qquad s.t. \;\; d = \nabla\sigma \tag{2.67}$$

And using constrain as a penalty term, the unconstrained problem given by the equation:

$$\Delta\sigma = argmin_{\sigma,d}\{\frac{\mu}{2}\|J\sigma - u\|_2^2 + \alpha\|d\|_1 + \frac{\beta}{2}\|d - \nabla\sigma\|_2^2\} \tag{2.68}$$

To solve this equation, Bregman iteration technique could be applied [74], referring to equations (2.63) and (2.64), the iterative equations of Split Bregman can be simplified as:

$$(\sigma^{k+1}, d^{k+1}) = argmin_{\sigma,d}\{\frac{\mu}{2}\|J\sigma - u\|_2^2 + \alpha\|d\|_1 + \frac{\lambda}{2}\|d - \nabla\sigma - b^k\|_2^2\} \quad (2.69)$$

$$b^{k+1} = b^k + \nabla\sigma^{k+1} - d^{k+1} \quad (2.70)$$

Optimization equation of (2.69) can be separated based on the first-order derivative with respect to σ and d:

$$\sigma^{k+1} = argmin_{\sigma}\{\frac{\mu}{2}\|J\sigma - u\|_2^2 + \frac{\lambda}{2}\|d^k - \nabla\sigma - b^k\|_2^2\} \quad (2.71)$$

$$d^{k+1} = argmin_{d}\left\{\alpha\|d\|_1 + \frac{\lambda}{2}\|d - \nabla\sigma^{k+1} - b^k\|_2^2\right\} \quad (2.72)$$

2.5.3 Spatiotemporal Total Variation Algorithm

In this thesis, a spatiotemporal reconstruction framework is proposed that exploits regularisation [33] [34]. Spatiotemporal total variation was chosen, as ERT images can be well approximated by a piecewise constant function and consecutive frames are expected to be similar. This allows the exploitation of redundant information across consecutive frames. The spatiotemporal total variation problem can be written as follows:

$$arg\min_{\Delta\sigma}\left\|\nabla_{x,y,z}\sigma\right\|_1 + \|\nabla_t\sigma\|_1 \quad \text{s.t.} \quad \left\|\tilde{J}\sigma - u\right\|_2^2 \leq \delta \quad (2.73)$$

Where the first and second terms correspond to isotropic spatial TV and temporal TV functions, respectively, and where σ represents a 4D conductivity distribution and $\tilde{J}$ is an augmented Jacobian operating on acts in a frame-by-frame basis.

The constrained optimization problem (2.73) can be solved using the split Bregman formulation, which efficiently handles constrained optimization and L1-regularisation. Using the Bregman iteration, the constrained problem (2.73) is converted into an iterative scheme:

$$\sigma^{k+1} = arg\min_{\sigma}\left\|\nabla_{x,y,z}\sigma\right\|_1 + \|\nabla_t\sigma\|_1 + \sum_{i=1}^{I}\frac{\mu}{2}\left\|\tilde{J}\sigma - u^k\right\|_2^2 \quad (2.74)$$

$$\mathrm{u}^{k+1} = \mathrm{u}^{k} - \tilde{\mathrm{J}}\sigma^{k+1} + \mathrm{u}, \tag{2.75}$$

Where (2.74) is an unconstrained optimization problem and (2.75) is a Bregman iteration that imposes the constraint iteratively. The cost function in (2.74) is still hard to minimize given the non-differentiability of the TV functional, but this can be easily done with a splitting technique. Including auxiliary variables allows splitting L1- and L2-function in such a way that they can be solved in separate steps in an easy manner. Images σ are given analytically by solving a linear system and L1-functions are solved using shrinkage formulae. To perform the split, we include $\mathrm{d}_x = \nabla_x\sigma, \mathrm{d}_y = \nabla_y\sigma, \mathrm{d}_z = \nabla_z\sigma, \mathrm{d}_t = \nabla_t\sigma$, so equation (2.74) becomes

$$\begin{aligned}\left(\sigma^{k+1}, \mathrm{d}_x, \mathrm{d}_y, \mathrm{d}_z, \mathrm{d}_t\right) \\ = arg \min_{\Delta\sigma, \mathrm{d}_x, \mathrm{d}_{y,} \mathrm{d}_z, \mathrm{d}_t} \left\|\left(\mathrm{d}_x, \mathrm{d}_y, \mathrm{d}_z\right)\right\|_1 + \|\mathrm{d}_t\|_1 \\ + \frac{\mu}{2}\left\|\tilde{\mathrm{J}}\sigma - \mathrm{u}^{k}\right\|_2^2 \quad \text{st.} \quad \mathrm{d}_i = \nabla_i\sigma \end{aligned} \tag{2.76}$$

Constraints in equation (2.76) are handled using the Bregman iteration as above, which leads to the following iterative scheme [84]

$$\left(\mu\tilde{\mathrm{J}}^T\tilde{\mathrm{J}} + \lambda\sum_{i=x,y,z,t}\nabla_i^T\nabla_i\right)\sigma^{k+1} = \mu\tilde{\mathrm{J}}^T u^k + \lambda\sum_{i=x,y,z,t}\nabla_i^T\left(b_i^k - d_i^k\right) \tag{2.77}$$

$$p^k = \sqrt{\sum_{i=x,y,z}\left|\nabla_i\sigma^{k+1} + b_i^k\right|^2} \tag{2.78}$$

$$d_i^{k+1} = \max\left(p^k - \frac{1}{\lambda}, 0\right)\frac{\nabla_i\sigma^{k+1} + b_i^k}{p^k} \quad \text{for } i = x, y, z \tag{2.79}$$

$$d_t^{k+1} = \max\left(\left|\nabla_t\sigma^{k+1} + b_t^k\right| - \frac{1}{\lambda}, 0\right)\frac{\nabla_t\sigma^{k+1} + b_t^k}{\left|\nabla_t\sigma^{k+1} + b_t^k\right|} \tag{2.80}$$

$$b_i^{k+1} = b_i^k + \nabla_i\sigma^{k+1} - d_i^{k+1} \quad \text{for } i = x, y, z, t \tag{2.81}$$

$$u^{k+1} = u^k + u - \tilde{J}\sigma^{k+1} \tag{2.82}$$

Equation (2.77) is given by the first-order derivative with respect to σ, and (2.78)-(2.80) use the shrinkage technique to minimize the auxiliary variable d in space and time domains respectively. Equations (2.81)-(2.82) denote the Bregman iterative scheme for updating, and it will stop when it meets convergence condition.

2.5.4 Temporal one-step solver

Another temporal algorithm known as a temporal one-step solver (TOS) was proposed in [43] in 2007, which was based on the Gauss-Newton one-step algorithm. Instead of reconstructing images frame by frame, TOS uses a data set that is combined with the data of nearby frames, where the data set and the conductivity change are given by:

$$\widetilde{u_n} = [u_{n-d}, \cdots, u_n, \ldots, u_{n+d}]^T \tag{2.83}$$

$$\widetilde{\sigma_n} = [\sigma_{n-d}, \cdots, \sigma_n, \ldots, \sigma_{n+d}]^T \tag{2.84}$$

The idea of TOS is that it correlates temporal information of consecutive frames in a time window, while STTV chases piecewise constants in time. For the case of monitoring the disappearing process of a target, STTV will cut it off instantly with its sharpness in time, whereas TOS correlates the whole process, which introduces smoothness for a temporal process. In (2.83) and (2.84), it takes d frames of data before and after frame n, in this case, the length of the data set would be (2d+1), and d is an integer and must be smaller than n.

The forward problem is modified into:

$$\widetilde{u_n} = \tilde{J}\widetilde{\sigma_n} + noise \tag{2.85}$$

The Jacobian is considered constant, and the augmented matrix augmented $\tilde{J} = \mathrm{I} \otimes \mathrm{J}$. Using GN One-step method, the inverse problem is formulated as:

$$\|\widetilde{u_n} - \tilde{J}\sigma_n\|^2 + \lambda^2\|\widetilde{\sigma_n}\|^2 \tag{2.86}$$

By solving (2.86), as stated in [43], the formulation is written as:

$$\widetilde{\sigma_n} = [\Gamma \otimes (PJ^T)][\Gamma \otimes (JPJ^T) + \lambda^2(I \otimes V)]^{-1} \cdot \widetilde{u_n} \tag{2.87}$$

In (2.87), V is an identical matrix, $V = eye(size(J, 1)$. $P = R^{-1}$ where $R = \alpha R_1 + \beta R_2 + \gamma R_3$. R_1 contributes to a NOSER prior, $R_1 = diag(diag(J^T * J))$, a diagonal matrix with diagonal elements of $J \cdot J^T$. R_2 denotes the Tikhonov regularization matrix, an identity matrix with a size of R_1. R_3 is a Laplacian regularisation matrix. Γ is a time-weighted matrix defined on the time window $(-\mathrm{d}, \mathrm{d})$ with a constant time weight γ,

$$\Gamma_{xy} = \gamma^{|x-y|} \qquad x, y = -d, \ldots, d \tag{2.88}$$

Computational time can be reduced with pre-calculation of $B = [\Gamma \otimes (PJ^T)][\Gamma \otimes (JPJ^T) + \lambda^2(I \otimes V)]^{-1}$

2.6 Study of image quality

Evaluation of the reconstructed images is always demanded when judging the accuracy when compared with the true situation. In [85] , the authors suggest several parameters that quantitatively evaluate the image quality, and these parameters have been widely used in the research of image reconstruction problems. Note that all of the computation of these parameters are based on a Thresholding image, where the image is black-and-white and composed of binary numbers.

2.6.1 Position Error (PE)

PE represents the error between the true position and the position in the reconstructed image. Numerical Position is described by the Centre of Gravity (CoG) of the target, and PE has been defined as:

$$PE = D_R - D_{TRUE} \tag{2.89}$$

Where D_R denotes the position in the reconstructed image given by the COG of the imaged target, and D_{TRUE} is the true position (CoG) of the target, where Thresholding of the whole reconstructed image will be required before calculating where the CoG of the target is located. CoG is computed based on the size and the shape of the target that is represented by a binary-number image. PE represents the accuracy of the target position that the reconstructed image makes, hence, it is treated as one of the standards when image quality is being evaluated. Obviously, less error is always optimal, so the PE expected to be small and stable with various locations of the target.

2.6.2 Resolution (RES)

RES is given by the ratio of the number of pixels in an object to the total number of pixels in the entire region of the reconstructed image. A uniform and small RES means it is more likely to be a reliable result since instabilities may lead to a non-uniform RES, and low-quality images also suffer from larger fractions. A uniform RES is one of the important criteria for evaluating image quality. In terms of previous work, RES is calculated by:

$$RES = \sqrt{\frac{A_q}{A_0}} \tag{2.90}$$

Where A_q and A_0 are given by the number of pixels of the target and the whole medium respectively.

2.6.3 Amplitude response (AR)

The amplitude response (AR) is defined by the ratio of the amplitudes of the image pixel to that of the total image pixel. AR is desired to be constant. It can be expressed as below:

$$AR = \frac{\sum_k [\widehat{X}]_k}{V_t \frac{\Delta\sigma}{\sigma_r}} \tag{2.91}$$

Where,

V_t is the volume of the image target

σ_r is the reference conductivity of a homogeneous medium

$\Delta\sigma$ is the difference between target conductivity and reference conductivity, $\Delta\sigma = \sigma_t - \sigma_r$

2.6.4 Shape deformation (SD)

Shape deformation represents the difference in object shape between the reconstructed image and the true shape of the tested target. Calculation of SD is conducted by working out the ratio of the unfitted area of the object on the image to the area of the entire image.

$$SD = \frac{\sum_{k \notin C} [\widehat{X_q}]_k}{\sum_k [\widehat{X_q}]_k} \tag{2.92}$$

Where C is the domain of the true shape, and K is the entire domain of the image. The area is measured by the number of pixels/voxels of each. A small SD index is desired since the recovered object is expected to be a shape that is close to the true shape of the target to be visualized.

2.7 Conclusion

This chapter introduces the details of ERT, with basic background information, including ERT devices and data measurement strategy, being introduced in the first part. Furthermore, the theory is discussed by imposing Maxwell's equations since ERT is a technique regarding the problem of electromagnetic fields. In addition, the forward problem of ERT is introduced by defining a mathematical model and the complete electrode model (CEM), and the FEM equations and sensitivity matrix are derived in detail. Moreover, several regularisation algorithms are introduced, where Tikhonov and SBTV are represented as methods for static imaging, and STTV and TOS are used for solving dynamical imaging. Finally, quantitative parameters are introduced for evaluating image quality. In general, this chapter covers basic theory, and all of the simulation and experimental studies discussed in the following chapters are based on the contents introduced in this chapter.

Chapter 3 Multiphase Flow

Liquid, gas, and solid are three forms of substances in nature, known as phases. Multiphase obviously refers to more than a single phase emerging simultaneously. For flows that involve two or more phases, they can be termed multiphase flow. Classification of multiphase flow depends on various combinations of phases, given by single-phase flow, two-phase flow, and three-phase flow. Single phase flow is difficult to produce in the industry as phase mixture is encountered. Many two-phase flows are encountered in flow pipelines, such as, gas-liquid flow, solid-liquid flow, liquid-liquid flow. Although the liquid is the only phase present in liquid-liquid flow, examples, such as, oil-water, show different chemical characteristics produce a separation between materials, therefore, it also considered as two-phase flow. Three-phase flow is more complicated as more materials are involved, which also pose challenges to visualization for electrical tomography as a single tomographic modality may not work for recognizing two non-conductive phases. In industrial process, a few types of multi-phase flows are present, such as, air-water two-phase flow, oil-water two-phase flow, and solid-water two-phase flow and air-oil-water three-phase flow. Generally, depending on the proportions of phase ratio or motion, one of the phases in the flow dominate it, this is called the continuous phase, while the other is termed the disperse phase. For example, water can be a continuous phase in many types of air-water flow. For the case of oil-water flow, it can be divided into oil-in-water and water-in-oil, and the dominating one will be the continuous phase. Multiphase flow involved fluid mechanics, heat transfer, and a combination of phase and pressure change, these varying concepts lead to its complexity [86].

3.1 Background and applications

There are many examples of multiphase flow present in a variety of applications. First, the multiphase flow may appear by phase transferring phenomenon between water and steam, which generates gas-water two-phase flow in some industrial system and daily life production processes, for example, inside a boiler by a steam generator or water condenser

of modern large systems. In modern power generation systems, shown in Figure 3.1, multiphase flow occurs in steam cycles, which is produced by heating high-pressure water and then liquefying it in a cooling tower or condenser. In a carbon capture and storage cycle system (Figure 3.2), reduction of carbon from the fuel is demanded prior to burning to help reduce environmental pollution, the multiphase flow appears in the process of water cooling or gasification for the requirement of condensed water or steam in the cycle. Moreover, oil-water two-phase flow occurs due to the mixture of phases during the extraction of crude oil (Figure 3.3) this also produces multiphase flow, where crude oil, hot steam/ gas, and driving water are mixed during the steam injection applied to the oil field. The circumstances of the multiphase flow in a pipeline can suggest the operational conditions of an industrial processing system. In the process of solid material transportation, where materials carried by liquid material produces a solid-liquid flow. Parameter control, such as, flow velocity, percentage of gas/oil, is always demanding in industrial applications. Proper speed control on materials transported in pipelines can not only reduce the damage of the pipeline inner-wall and save costs and energy, but it can also help avoid the occurrence of pipeline blockages or more serious dangerous accidents, and real-time measurements of multiphase flow can suggest daily yields of oil/gas production. Therefore, control of entire industrial systems can be implemented by monitoring and controlling the numerical parameters from the multiphase flow. However, flow must be visualized or quantitatively evaluated for people estimating the interior information to reach control purposes. Hence, it is necessary to develop methods that can effectively image such a dynamic process and make measurement of quantitative parameters that can be implemented by an image-based method if good-quality images are guaranteed. ERT is one of the electrical tomographic methods for visualizing and can potentially suggest measurements based on reconstructed images and has great potential as an imaging technique of high time resolution, which is also easy to operate and low cost.

In this chapter, some of the backgrounds of multiphase flow is reviewed and introduced. In section 3.1, flow regimes in different pipelines are presented, in addition, some common numerical parameters regarding multiphase flow are introduced. Moreover, literature about multiphase imaging and measuring using ERT are reviewed.

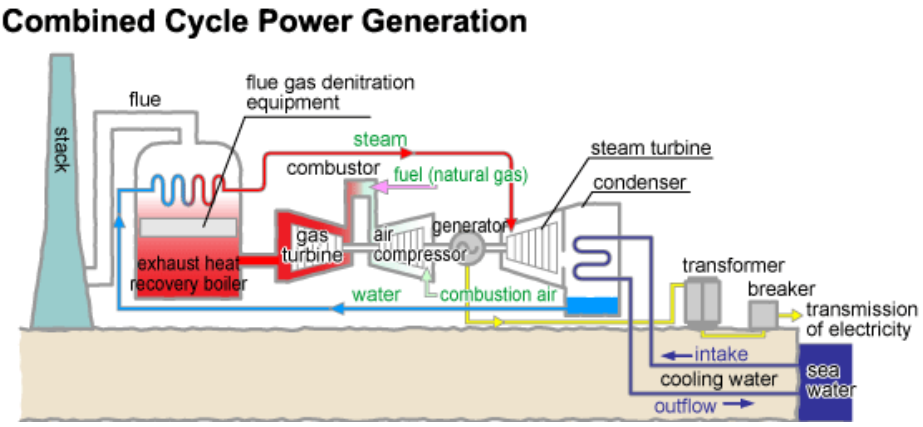

Figure 3.1: Diagram of power generation with steam cycle [87]

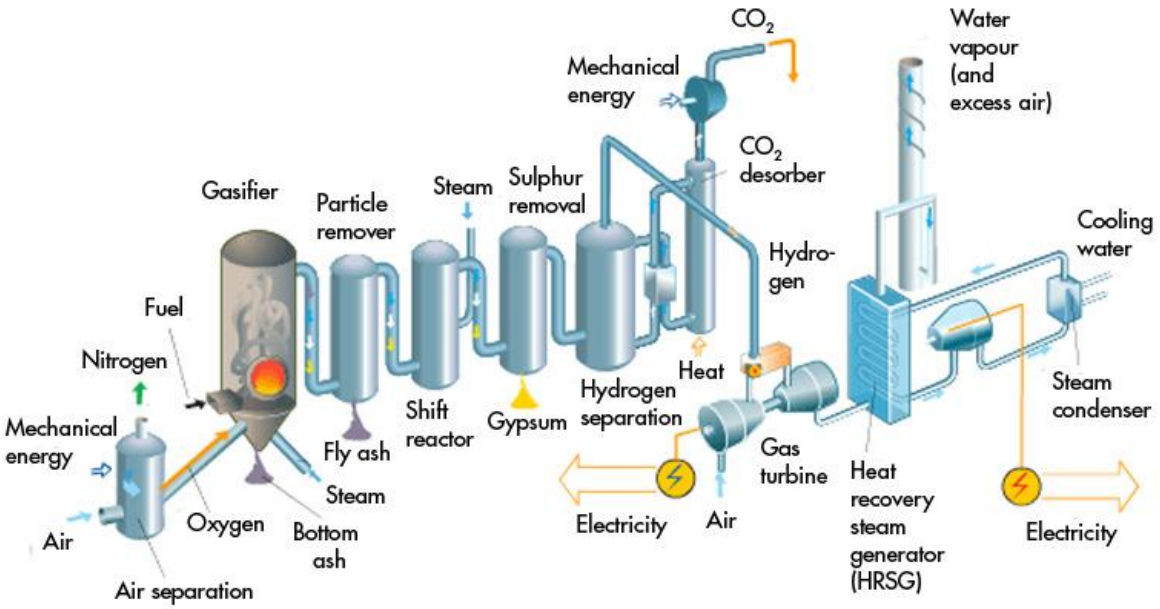

Figure 3.2: Diagram of pre-combustion capture system for carbon capture [88]

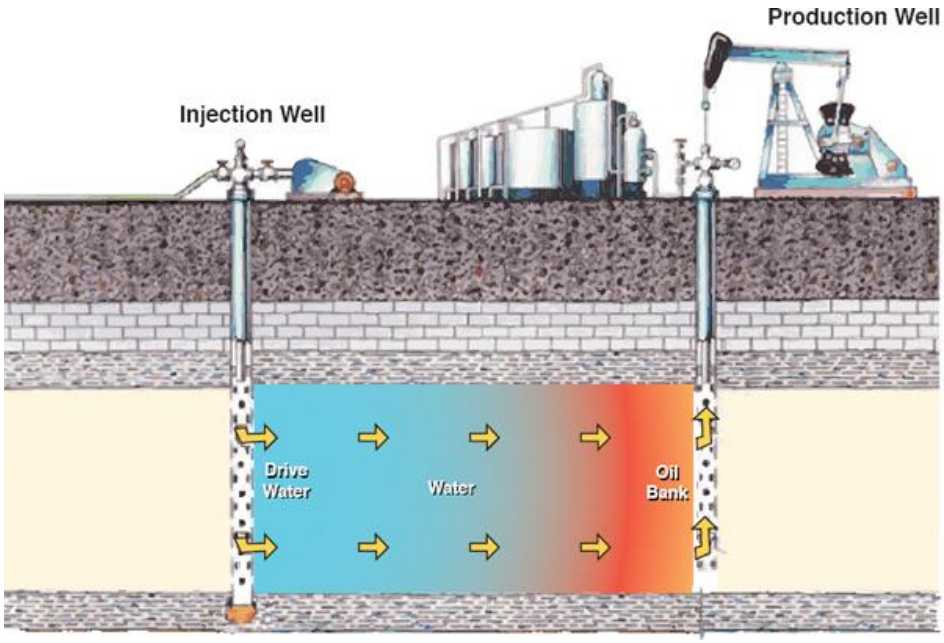

Figure 3.3: Diagram of crude oil extraction by applying flood injection [89]

3.2 Flow regime

In flow pipelines during industrial processes, classification of multiphase flows depends on the flow direction, resulting in flows in horizontal pipes, vertical pipes and inclined pipes (of different angles). Each of these is also divided into a few flow patterns, also known as flow regime. The behaviour of phases in multiphase flow is affected by many factors which are unpredictable, and situations even fluctuate under the same conditions. Visualization of flow allows people to gain fluid interior information, such as, phase distribution, state of phase interface, void fraction, and velocity profile. Different reasons, such as, types of materials, the flow velocity of phases, geometry (such as pipeline diameter or the angle of pipe), pressure, affect the behavior of flow configurations. Determination of flow patterns can help access knowledge of the flow internal situation. In this section, flow regimes of air-water flow and oil-water flow in horizontal and vertical orientations are investigated.

3.2.1 Air-water two-phase flow pattern

- Air-water flow in a horizontal pipe

The most commonly occurring flow configurations of air-water two-phase flow have the following types, shown in Figure (3.4), these are dispersed bubble flow (bubbly flow),

annular flow, elongated bubble flow, and slug flow [90]. Stratified flow and wavy flow can also emerge for cases with a lack of water. Mostly, the relative phase volume and flow rate affect the flow patterns in horizontal pipes. Dispersed bubble flow features many small bubbles with a relatively uniform distribution within the liquid phase. Its formation requires a low flow rate with a sufficient quantity of water. Increasing the air volume and gas-phase velocity, the size of bubbles becomes bigger, which produces elongated flow. In such a flow pattern, the liquid phase is partially separated by large bubbles. These large bubbles can even block the pipe and break the pipeline into a few sections, which bring on slug flow. If the air quantity is further increased, the flow in the pipe cannot reach the top due to a lack of liquid, and the space inside the pipe will be separated into gas and water completely. Stratified flow can be produced under such a situation with a low velocity and this results in a smooth interface, whilst wavy flow appears with higher flow rates. Annular flow is characterized with liquid attached to the wall and the air phase flowing through the core with some water droplets.

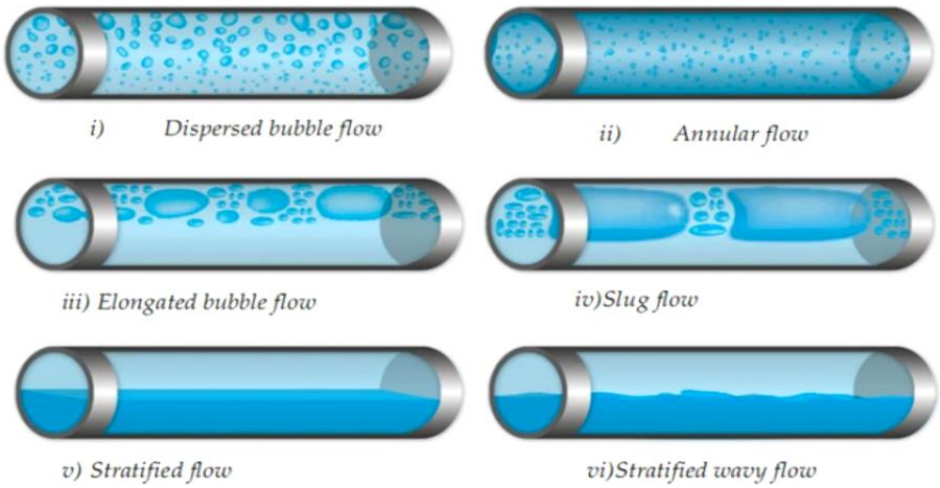

Figure 3.4: Flow regime of air-water two-phase flow in the horizontal pipe [90]

- Air-water flow in a vertical pipe

In vertical pipes, the phase distribution is relatively simple due to the symmetrical feature of flow patterns. Based on the literature [91], classification of air-water two-phase flow has 5 different configurations:

(1) Bubbly flow: Tiny bubbles are dispersed in the liquid phase, and phase velocities are fairly uniform.

(2) Cap-bubble flow: The quantity of bubbles is increased, and some bubbles combine into cap-shaped bubbles of a bigger size.

(3) Slug flow: Bullet-shape bubbles are formed with the further increase of air quantity. These big bubbles move upwards in the pipe core and break by liquid phases with some small bubbles in between. Slug flow is unstable.

(4) Churn-turbulent flow: Instability of the flow pattern lead to the breakdown of the slug flow structure and form a flow regime pushing the liquid upwards. For a pipe with a small diameter, the flow regime is characterized with a gas path in the core, which requires a high gas-phase velocity.

(5) Annular flow: liquid attached to the pipe wall moving upwards. Gas-phase in the core and moving upwards with tiny liquid droplets.

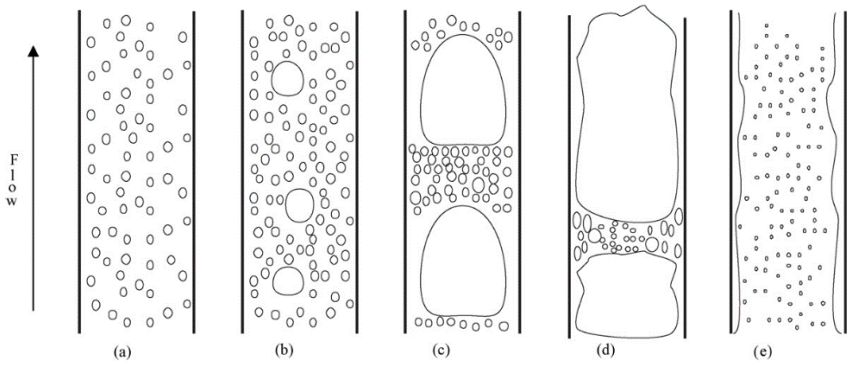

Figure 3.5: Flow regime of air-water two-phase flow in a vertical pipe

3.2.2 Oil-water flow pattern

Flow regimes of oil-water two-phase flow occur in different situations to air-water flow due to the floating of the oil phase. Classification of oil-water flow is more complicated due to the diversity of oil characteristics. The viscosity ratio of oil and water can vary from below one to up to a million, which leads to a considerable variety of flow patterns [92]. In recent decades, many groups have carried out several experiments to observe the flow patterns of oil-water two-phase flow. Xu Summarised observed flow patterns in horizontal pipes in previous works from 1959 until 2006, and they made conclusions on the flow patterns of heavy oil and light oil, where flow patterns also have a difference between water dominated and oil dominated [93]. Ahmad reviewed current research into the state of oil-water two-

phase flow and reviewed flow patterns in vertical pipes based on previous works [94]. Several main types of flow pattern are summarised below:

(1) Stratified flow

(2) Stratified flow with a mixture of oil and water on the interface

(3) Dispersed flow (water dominated / oil-dominated): oil in water, water in oil, dual dispersion, oil in water and water

(4) Churn flow (in the vertical pipe)

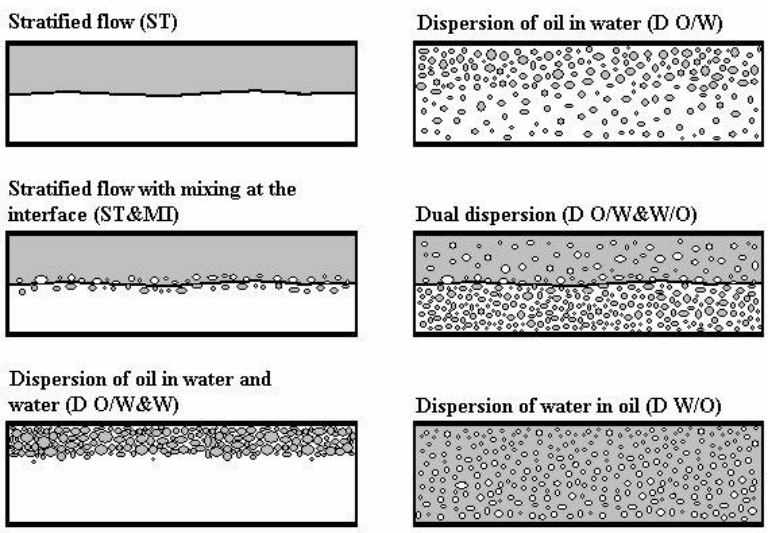

Figure 3.6: oil-water flow pattern in the horizontal pipe [92]

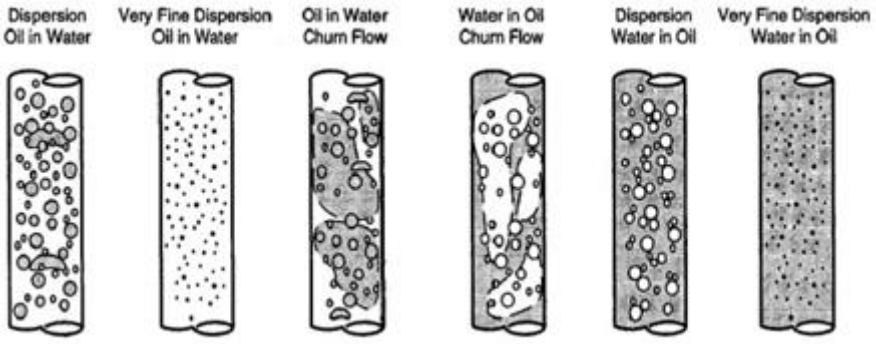

Figure 3.7: oil-water flow pattern in vertical pipe [94]

3.3 Quantitative parameters of two-phase flow

3.3.1 Flow rate and flow quality

The following parameters are commonly defined regarding flow rate.

(1) Mass flow rate M: flowing mass (kg) of the fluid in unit time (s)， given by kg/s

(2) Volumetric flow rate V: volume (m^3) of the fluid in unit time (s), m^3/s

(3) Flow quality: the ratio of mass flow rate of phase (M_G, M_L) to total mass flow rate M

In terms of a gas-liquid two-phase flow, these parameters are termed: total/gas-phase/liquid-phase mass flow, total/gas-phase/liquid-phase volumetric flow, flow quality of gas/liquid. These parameters have the following relationships:

$$M = M_G + M_L \tag{3.1}$$

$$V = V_G + V_L \tag{3.2}$$

$$\rho_g = \frac{M_G}{V_G} \qquad \rho_l = \frac{M_L}{V_L} \tag{3.3}$$

$$\chi = \frac{M_{g/l}}{M} \quad , \quad \chi \in (0,\ 1) \tag{3.4}$$

3.3.2 Void fraction

Void fraction is another important parameter to evaluate in multiphase flow. In terms of gas-liquid two-phase flow, void fraction is the ratio of gas phase to the fluid in the pipe, classified into Mass void fraction α_m, volumetric void fraction α_V, and cross-sectional void fraction α_A [7]. Normally, void fraction is presented as a percentage, which is expressed below:

$$\alpha_m = \frac{M_G}{M} \tag{3.5}$$

$$\alpha_V = \frac{V_G}{V} = \frac{V_G}{AL} \tag{3.6}$$

A is the cross-sectional area of the pipe, L is the effective length

$$\alpha_A = \frac{A_G}{A_G + A_L} \tag{3.7}$$

A_G and A_L are the cross-section occupied by the gas-phase and liquid-phase respectively

The void fraction of the dispersed phase can be determined by Maxwell's relationship equation if the conductivity distribution is already worked out. Conductivity can be calculated either by image reconstruction or a data processing method [95]. The dispersed phase fraction on each pixel can then be given by:

$$\alpha_d = \frac{2\sigma_c - 2\sigma_{mc}}{\sigma_{mc} + 2\sigma_c} \tag{3.8}$$

The overall dispersed phase fraction is determined by the average pixel void fraction. In equation 3.8, α_c is the conductivity of continuous phase which is usually a constant, such as the conductivity of water, and σ_{mc} is the local mixture conductivity given by the determined conductivity distribution from either images or a data processing method of ERT [96].

3.3.3 Velocity in two-phase flow

Many studies defined superficial velocity to describe two-phase flow, and it also categorized flow rate flux. The superficial velocity is expressed as a volumetric flow rate per unit cross-sectional area. Gas and liquid superficial velocity j_g and j_l are:

$$j_g = \frac{V_g}{A} \qquad j_l = \frac{V_L}{A} \tag{3.9}$$

The total velocity (total volumetric flux)

$$\mathrm{j} = \frac{V_g + V_l}{A} = j_g + \ j_l \tag{3.10}$$

In two-phase flow, the velocities of phases are different due to relative motion between the disperse phase and continuous. The phase velocities are given separately by the volumetric flow rate that has been defined in subsection 3.2.1. For the velocity of the gas phase $\mu_g$and the liquid phase μ_l:

$$\mu_g = \frac{V_g}{A_g} \qquad \mu_l = \frac{V_l}{A_l} \tag{3.11}$$

And relative velocity μ_r and slip ratio S:

$$\mu_r = \mu_g - \mu_l \tag{3.12}$$

$$\mathrm{S} = \frac{\mu_g}{\mu_l} \tag{3.13}$$

3.4 Flow models

Flow measurement is a complicated subject in industrial processes and scientific research. Interaction between phases leads to complexity in prediction or measurement of flow movement modes and flow parameter changes. Mathematical modelling of multiphase flow is normally based on fluid mechanics and flow characteristic by writing conservation equations, then solving the problem with effective simplification. In addition, experiments based on multiphase flow can be conducted to discover the relationship of various parameters in a flow system. According to different flow patterns, various proposed flow models are reviewed [97] [98]:

(1) Homogeneous flow model: Velocity of phases are considered to be identical, and the entire two-phase flow is treated as an integrated object. Such a flow model must satisfy the conditions of the slip ratio being equal to 1, and thermodynamic equilibrium. This flow model is suitable for dispersed bubbly flow or annular flow with a high gas-phase velocity.

(2) Drift-flux model: Relative motion of two phases is considered, and the resulting drift velocity. In conservation equations, the relative velocity is replaced by drift velocity, and a mixture equation is taking place by momentum equation. Drift-flux is appropriate for slug flow.

(3) Separated flow model: For cases of stratified flow where the motion of gas and liquid phases are separated, the separated flow model can be used and treat each phase independently. The constant velocity of the two phases is assumed.

(4) Two-fluid model: It is assumed the two phases are continuous, and exchanging mass, momentum, and energy on the interface. This flow model can describe two-phase flow more completely, but introduces a variety of variables and also corresponding

equations based on mass continuity, momentum conservation, and total enthalpy conservation, therefore, the two-fluid flow model is more difficult to solve.

3.5 Multiphase flow with ERT

Quantitative measurement and visualization of multiphase flow have been investigated for decades because of its importance in practical industrial applications. Multiphase flow is complicated since phase distribution and transferring are diverse, and transfers of heat, momentum, and energy are taking place dynamically. Benefiting from electrical resistance tomography that is capable of imaging spatial distribution without a high equipment cost or exposing materials to radiation, many previous works employed it as process tomography for purposes of visualizing or quantitative analysis attempting to figure out practical problems.

3.5.1 Flow regime recognition

In industrial processes, flow regime suggests the situations in flow systems, which is an important factor for reflecting actual conditions and solving practical problems. ERT is an appropriate technique to evaluate two-phase flows with a conductive medium as the continuous phase. Theoretically, the visualization capability of ERT can contribute to flow regime identifications by showing dynamically reconstructed images. However, image reconstruction may be time-consuming, and most algorithms are difficult to use for practical applications that require in-line observations. As a substitute, many works applied feature extraction on ERT raw data for identifying flow regimes. A group at Tianjin University identified gas-liquid flow regimes using ERT measurement data with accuracies over 80% [99], where a machine-learning algorithm known as SVM was applied with the extraction of fusion-feature vectors from ERT data. In 2009, this research was further studied with the combination of features using a V-cone meter for the recognition of different types of flow patterns [100]. In addition, Y. Zhang presented flow pattern recognition using SVM with principal component analysis (PCA) for feature extraction [101], and Neutral Network method with linear discriminant analysis (LDA) for feature extraction [102]. Moreover, B. Karki presented their research on horizontal-pipe flow pattern identification using ERT in

[103]. In their work, they used a method of information integrated from signal thresholds and frequency decomposition for the classification of flow regimes.

3.5.2 Velocity profile

Dual-plane ERT sensors were designed and investigated for calculating the velocity profile of two-phase flow, where people used cross-correlation, a method of signal processing, dealing with information from both electrode-planes aiming at determining the time delay. The velocity measurements can be determined for a constant distance between electrode planes. The reflected information from electrode planes can be either visualized 2D ERT images or raw data with feature extraction. The reconstruction-based method commonly termed the pixel-pixel cross-correlation method, where corresponded pixels are correlated to conduct point-to-point velocity profile calculations, while the other correlates extracted features from ERT measurement data on electrodes instead. In comparison, the feature-value based method can be faster since it avoids the process of regularisation, but the image-based method can show a more detailed velocity distribution. Literatures [104] [105] [106] presented works of dual-plane ERT system design with velocity profile quantitative studies using the feature-extraction method. In addition, velocity measurement based on ERT image reconstruction is also proposed for determining rheological behavior [22] and velocity vector distributions [107].

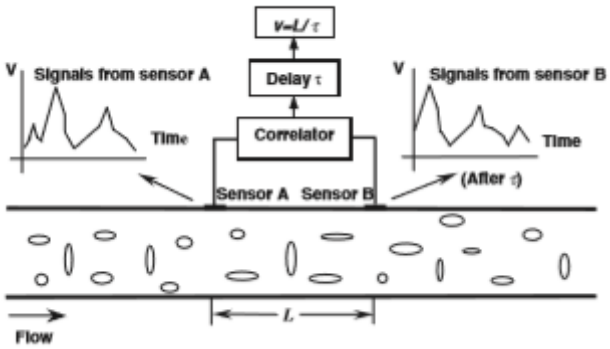

Figure 3.8: Dual-plane ERT for velocity measurement of two-phase flow [104]

3.5.3 Visualization

In industrial applications, evaluation of the flow behavior is helpful for understanding, situation prediction and control of multiphase flow. Visualization of multiphase flow is useful in practical applications for the characterization of flow process, and flow imaging analysis can explore the information of phase distribution, phase interface, void/volume fraction, and flow patterns. ERT has great potential in showing spatial and temporal information of flow processes, previous works were aimed at reconstructing cross-sectional 2D images with dual-plane sensors or using multi-plane sensors for 3D images. For example, swirling slurry flow has been investigated by ERT visualization for studies of phase distribution [108] [109]. Shang-Jie Ren simulated annular flow and evaluated phase distribution within an annulus tube with bubbles and liquid by visualizing ERT 2D images [110]. ERT visualization has also been applied in the milk processing industry for monitoring mixture dynamic processes using 3D reconstructions [111]. Moreover, different specific flow patterns are also investigated with ERT imaging, such as, stratified flow [112], slug flow [113], annular bubble flow [114], and swirling flow [115].

3.5.4 Phase concentration

Phase concentration (void/volume fraction) is one of the critical quantitative parameters of multiphase flow. In transportation processes, phase concentration influences flow quality. Moreover, phase fraction affects flow regimes, and its numerical determination also contributes to flow rate measurement in flow industries. In multiphase flow, the phase concentration accounts for the ratio of areas of a phase and the entire area. Tomographic methods are capable of determining phase fractions by 2D/3D flow imaging of cross sections or the entire medium, hence they have received much attention in the past few decades. ERT has been proven to be a feasible approach for measuring phase fractions [29] [95] [96]. Two ERT-based methods are commonly employed for the calculation of phase fractions. Obviously, image reconstruction of ERT is straightforward for achieving the proportion of dispersed phase. However, image-based phase concentration measurements

may suffer from low spatial resolution if regularisation is not optimal which can lead to errors. Therefore, image quality must be high enough to improve the accuracy to yield a qualified numerical phase fraction. Another type of ERT-based method uses measurement data, and the estimation of phase concentration is operated by deriving Maxwell's relationship equation (equation 3.8) without image reconstructions.

3.5.5 Dual-modality methods

Multi-modality means multiple tomographic techniques are working together for either improvement of zvisualization or measurement, or for more complicated situations, for example, phase distribution of three-phase flow might not be distinguishable properly with ERT only, because ERT cannot zrecognize two different non-conductive phases (such as, oil and bubble). For the case of oil-water flow, the oil phase cannot conduct injected current from ERT electrodes if oil becomes the continuous phase. Utilization of one modality of ERT cannot satisfy the expectations for those types of situations. However, for three-phase flow, ECT is capable of distinguishing gas and two liquid phases by determining the ratio of water and the other two non-conductive phases, in addition, ECT can detect water-in-oil flow via conducting displacement current to the non-conductive medium. The dielectric property of the medium contains information that accounts for resistivity and permittivity, and ERT and ECT are literally using the real part and imaginary part of the measurement data as input. In addition, both ERT and ECT have the advantage of high temporal resolution and non-radioactive exposure for the medium. Therefore, ERT-ECT dual modality has developed into a typical combination. Some literature have reported the state of research of such a method. In the past few decades, some ERT-ECT dual-modality systems were designed [116], and some works aiming at sensor integration have also been proposed [117] [118]. In particular, in [119], gas-oil-water flow with six different flow regimes in horizontal pipe is visualized based on data fusion of ERT/ECT. Q. Wang et al. evaluated the dual-modality method for gas-oil-water three-phase flow imaging. In their work, the capability of visualization is compared with ECT and ERT by conducting experiments with different water-liquid-ratio (WLR) on various flow patterns [120], and their results suggested the capability of each of the tomographic techniques against the percentage of water-phase (Figure 3.6).

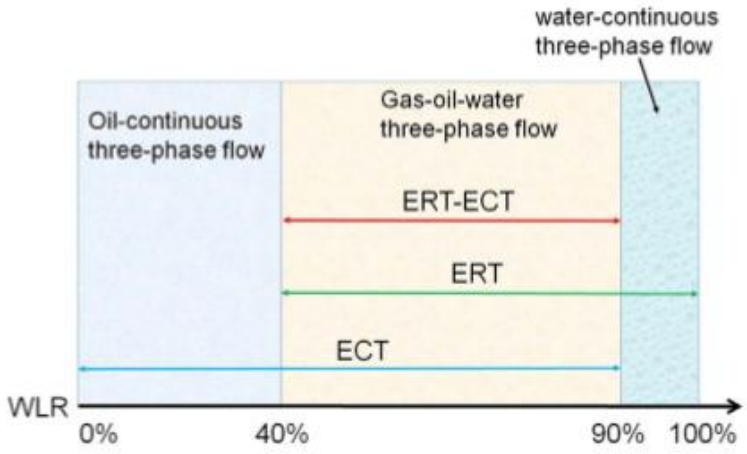

Figure 3.9: Capability of different electrical tomographic techniques against water-liquid-ratio [120]..

3.5.6 ERT with flowmeter

As demand grows from the many diverse industrial applications, the application of single detection technology is difficult to meet all the measurements needs. Emergence or fusion-sensory methods can provide more complete information from more aspects, and as a result have received the attention of many scholars. Literature has shown that ERT can combine with Electromagnetic flowmeters (EMF). An ERT-EMF based oil-in-water flow measurement has been presented in [121], where estimated oil-phase concentration from ERT provides assistance for EMF to measure water flow rate. Such combinations have also been applied for the examination of counter-gravity slurry flow for the measurement of phase flow rate [122], where ERT provides the fraction and velocity of the dispersed phase. Another flow meter known as the Venturi flowmeter provides information based on differential pressure. Combination with ERT can provide supplement knowledge of flow pattern and phase fraction, resulting in more reliable measurements of mass flowrate [123].

3.6 Conclusion

Multiphase flow with different constituent substances is encountered in many applications. Diversity of flow patterns and complicated situations of multiphase flow including heat, momentum, and energy transferring impose challenges on solving practical problems in the

industry. Research works focusing on many industries such as petroleum, transportation processes, and chemical engineering have shown the importance and necessity.

In this chapter, the background and situations of multiphase flow in real life are introduced, and related literature regarding ERT are reviewed. In general, this chapter includes four sections. Above all, flow patterns of two common two-phase flows, i.e. air-water, oil-water flow, are introduced, then some critical parameters of flow measurement are presented based on previous works in the first two sections. In addition, flow models that have been proposed in previous research are briefly concluded. Moreover, in section 3.4, applications of ERT related to flow visualization and quantitative measurement are reviewed from six aspects, which summarize and point out the status of current research stage.

ERT has shown great potential in visualizing two-phase flow or providing quantitative parameter measurements in industrial processes, although ERT has not yet become a mature technology. In terms of flow visualization based on image reconstruction, improvements in optimizing image spatial resolution are necessary and precise flow parameter measurement also benefits from a high image-quality. Improvement in visualizations can be made by different aspects, where optimizing regularisation algorithms is one of the approaches that can contribute. In addition, in the following three chapters, some work on visualizing phase distribution aiming at two-phase flow are presented.

Chapter 4 Temporal TV for ERT dynamical imaging

Electrical resistance tomography (ERT) is an imaging technique to recover the conductivity distribution with boundary measurements via attached electrodes. There is a wide range of applications using ERT for image reconstruction or parameter calculation due to high-speed data collection, low cost, and the advantages of being non-invasive and portable. In terms of process tomography of a two-phase flow, the object being detected is dynamical. ERT is considered a high temporal resolution method, a temporally regularized method can greatly enhance such a temporal resolution compared to frame-by-frame reconstruction. In some of the cases, especially in the industrial applications, dynamic movement of an object is critical. In practice, it is desirable for monitoring and controlling the dynamic process. ERT can determine the spatial conductivity distribution based on previous work, and ERT potentially shows good performance in exploiting temporal information as well. Many ERT algorithms reconstruct images frame by frame, which is not optimal and would assume that the target is static during collection of each data frame, which is inconsistent with the real case. Although spatiotemporal-based algorithms can account for the temporal effect of dynamic movement and can generate better results, there is not that much work aimed at analyzing the performance in the time domain. In this chapter, we discuss the performance of a novel STTV algorithm in both the spatial and temporal domain, and Temporal One-Step based on Gauss-Newton algorithms were also employed for comparison. The experimental results show that the STTV has a faster response time for temporal variation of the moving object. This robust time response can contribute to a much better control process which is the main aim of the new generation of process tomography systems. This chapter is based on the published journal paper [33].

4.1 Introduction

Considering ERT for dynamical cases, most of the traditional algorithms can reconstruct images using individual frames of data, such as, Tikhonov, Gauss-Newton one-step, etc. However, to reconstruct images with the regularization methods that working frame by frame may not be an optimal choice, as high temporal resolution is one of the advantages of

ERT system, and information of the correlation between individual frames might worth to be explored to contribute to the image quality. Traditional regularizations solving spatial distribution of the conductivity across a single frame, which regularized the spatial distribution in that frame only. However, the target is always dynamical including the time during collecting each frame data, which lead to noisy data. For the purpose of process tomography, it requires an ERT system with very high speed such that such effect minimized since these types of algorithms cannot make effort on correlating between neighboring frames. Temporal algorithms can regularize it to optimize visualizations along with time series. There were few methods tracking the moving object using the spatiotemporal information. First of all, Kalman filtering has been used in different tomographic techniques. For example, in 1998, M. Vauhkonen proposed Kalman filter method to track fast changes in electrical impedance tomography (EIT) [44]. Following that, P. J. Vauhkonen and M. Vauhkonen evaluated the Kalman filter and smoother approach and compared it with traditional algorithms using phantom experiments data [46]. In [124], M. Soleimani and M. Vauhkonen were using Kalman filter on electrical capacitance tomography (ECT) and electromagnetic induction tomography (EMT), and demonstrated Kalman filtering approach could improve the spatiotemporal resolution. In addition, another algorithm is known as temporal one-step solver (TOS), which is based on GN one-step method has been proposed by A. Adler and T. Dai in [43], and has been investigated by comparing with other approaches, such as, Kalman filter and conventional GN one-step method. A 4D regularization was proposed afterwards, which combined both spatial (3D) and temporal priori, and using simulation method based on EIDORS [125]. Temporally correlated algorithms such as the ones shown in above are providing an opportunity for faster speed and less averaging in ERT data. A non-temporal regularization however will limit the time resolution. A temporal algorithm with TV regularization in time can overcome this problem, providing both high speed and sharp temporal responses.

In practice, ERT could potentially be combined with a tomography-based control system. To reach the requirement of controlling application, high-quality images from ERT would be needed, and useful information is supposed to be extracted based on these reconstructed results for the proposes of, for example, implementation of emergency operation to avoid undesirable condition, velocity control of two-phase flow to avoid damage of pipeline

caused by over fast mean flow speed . In this chapter, we particularly interested in the temporal and spatial performance of spatiotemporal total variation (STTV) method that has been proposed in [45]. By comparing it with TOS algorithm, which has been used in [43], we want to explore spatiotemporal information along with the time domain. The results of this chapter are based on 2D phantom experimental tests with the dynamical movement of inclusion. For each set of the results, STTV and TOS are employed using the same measured data set to ensure the consistence.

4.2 Method

In this chapter, we test the performance of dynamic cases. Time difference ERT imaging is used in this chapter. Considering dynamic case over static imaging, the object keeps moving its position, which makes the electric field change distribution at the same time, where the effects of magnetic fields are not considered in order to simplify this physical model. Because the process of current injection, as well as the conductive field, remain, both cases would have the same forward model. However, the time step of data collection cannot be neglected in practical dynamic cases as the dynamic electric field would affect the data measurement although this could be very fast. The condition of experiments is under low excitation frequency, which creates the assumption for the physical model that the effect of magnetic induction could be neglected for such a pure resistive model in a quasi-static electric field.

In the static ERT, the electrical conductivity can be described by $\sigma(x,y)$, whilst a time-varying conductivity in dynamical ERT means that the conductivity can be described by $\sigma(x,y,t)$. In the actual ERT experiments, we are dealing with a discrete number of spatial and time steps, which can be described by spatial and time resolutions. In dynamic ERT, with moving inclusions, the assumptions of forward modeling described in chapter 2 are still valid, and conductivity changes from $\sigma(x,y)$ to $\sigma(x,y,t)$. Further extension of static inversion to temporal inversion is described in the following section. Temporal algorithms have been used in this chapter are STTV and TOS, detailed information of the calculation scheme is demonstrated in section 2.3.3 and 2.3.4.

4.3 Experiments and results

4.3.1 Experimental setting up

Data collection of experiments in this chapter would require a complete ERT system, which composed with an ERT Hardware system, PC (with software) and a sensor.
The hardware system has been used in this chapter is known as EIT Swisstom Pioneer system [126] with 32 channels, which has following main components:

- 16 double-channel EIT chips to control 32 electrode
- Smart Sensor Belt Connector that integrated with AC current injection (1-7mA, 50KHz-250KHz), voltage signal demodulating, high-speed data collection (up to 80 frames/second)
- Interface module: Frame synchronization input and output, synchronization signal, power management between Sensor-Belt and Sensor-Belt-Connector
- Power supply

The data collection software is running with the Swisstom EIT Pioneer to collect data, where the excitation frequency, current peak value, data collection speed, and current pattern are available to be adjusted. In addition, the connection with the electrode could easily be checked via Sensor Quality panel, and the real-time dynamical image is also available.

- Sensor

The 2D sensor has been used in experiments is a cylinder-shape PMMA container, with diameter of 19cm and height of 25 cm. On the side wall of the sensor, 16 electrodes (2cm x 4cm) are evenly fixed along the surface as an electrode-plane. A heavy circular metal board is sitting on the top of the container, connected by three long screws with the base board, in order to avoid leaking of any liquid.

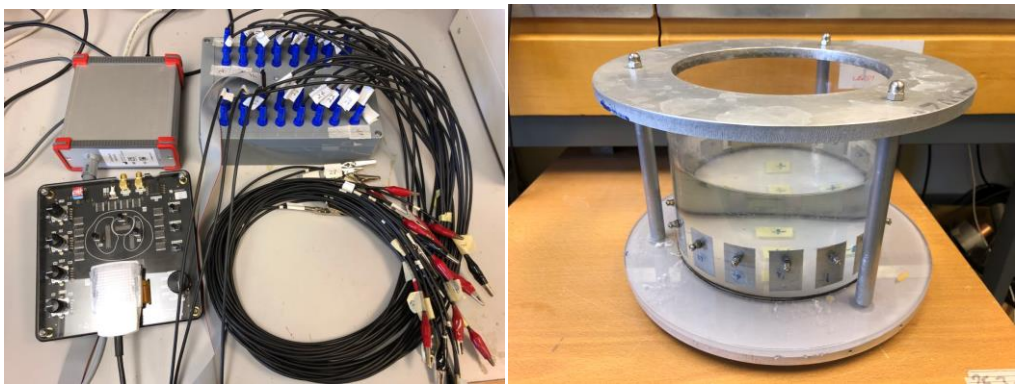

(a) (b)

Figure 4.1: Experimental devices and sensor. (a) Swisstom EIT Pioneer system (b) experimental tank

4.3.2 Experimental tests

In this section, we are showing reconstructed images of different tests. Tap water and a plastic bar (3.1 cm diameter) were used as background and the moving object under tested respectively. Cross movement and circular movement were considered as two types of movement in the dynamical test. In all of the experimental tests, the peak value of exciting current has been used is 7mA, and operation frequency is 270 KHz. To well compare two algorithms, lots of data has been collected under various data collection rate on various dynamic cases for image reconstruction. In this section, we only displayed some typical results here in each part. Different dynamical movement type has been setting up, and results from each type of dynamical movement using both algorithms are displayed. Regarding the image reconstruction, there are 6 images are extracted from the generated dynamical image of each movement type to demonstrate the performance of both algorithms.

Dynamical test is divided into two types of movement in this chapter: cross movement and circular movement. Cross movement is the case that the inclusion moving crosses the domain through the center along the diameter from one side to the other, and the circular movement is the type of the movement that the object moving along a circle near the

boundary of the domain. The illustration of the dynamical movement can be seen in the figure below.

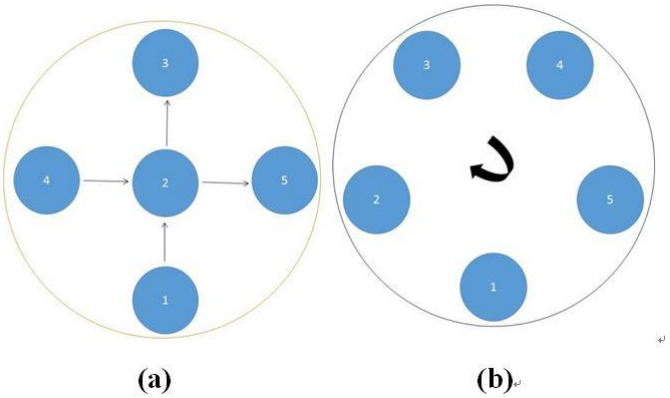

Figure 4.2: Illustration of the dynamical movement type. The cross movement is showing in (a), and (b) illustrates the circular movement.

- Test 1 Cross movement

In the first dynamical test, it was setting up that the plastic bar was driving manually to move from bottom to the top, then from left to right cross the domain respectively. As showing in figure 4.2 (a), the inclusion movement cross the domain from 1 to 3 via position 2 in the center, then it moves from 4 to 5. The excitation current was using 7mA with frequency of 270 KHz, and the data collection rate has been used is 24 frames/second. On both tests of the cross movement, 850 and 950 frames of measurement data has been collected with background data included. The measurement data that taken from the background (with tap water only) is more than 100 frames when we keep more than 5 seconds before we start to put the plastic bar into the tank, so the average background data of the first hundred frames would be used for the propose of removing some noise. By using STTV and TOS algorithms respectively, reconstructed images are produced, as displayed in the Table below, where the second column of the Table showing the images of TOS algorithm, and results from STTV are placed in third column. Images produced by using frame-by-frame based SBTV algorithm are also represented here. There are 6 slices of images has been included in the Table to demonstrate the recovery images of the movement process using both algorithms.

Table 4.1: Reconstructed images of cross-movement in Test 1, where the inclusion is moving from the bottom to the top.

No.	TOS	STTV	SBTV
1	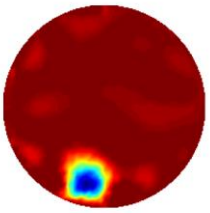	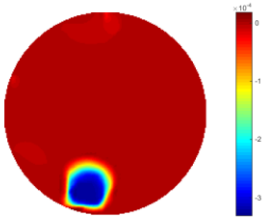	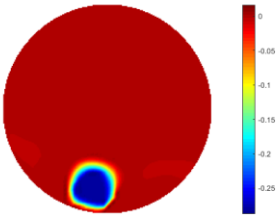
2	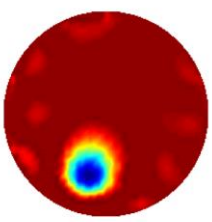	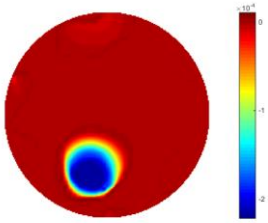	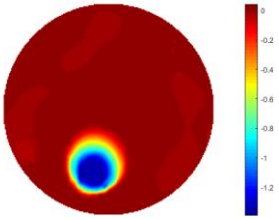
3	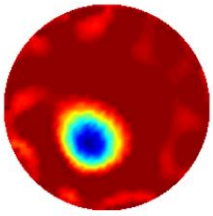	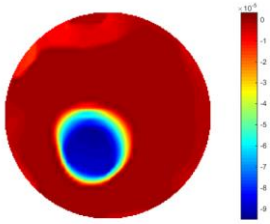	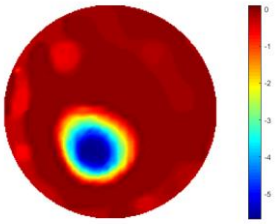
4	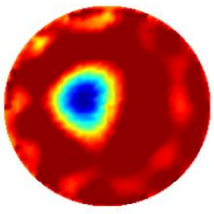	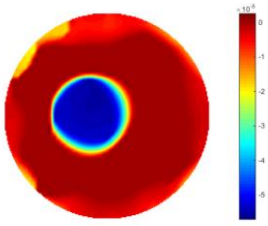	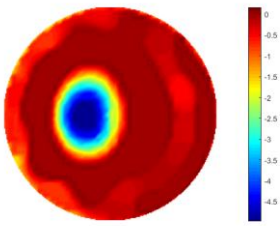
5	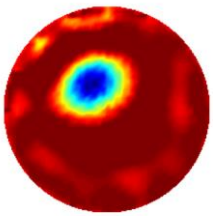	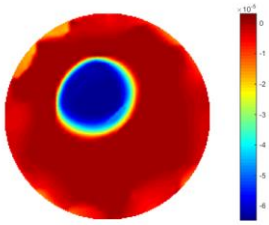	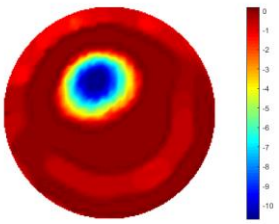

6	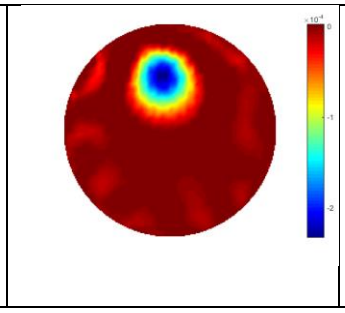	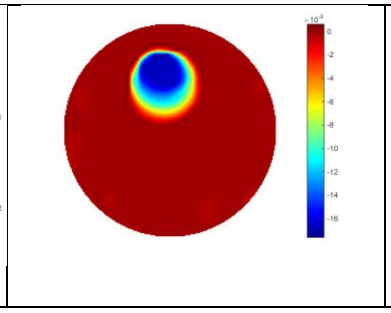	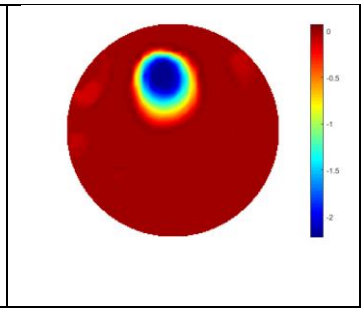

Table 4.2: Reconstructed images of cross movement in Test 1, where the inclusion is moving from left hand side to the right-hand side

No.	TOS	STTV	SBTV
1	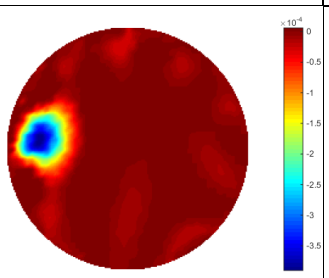	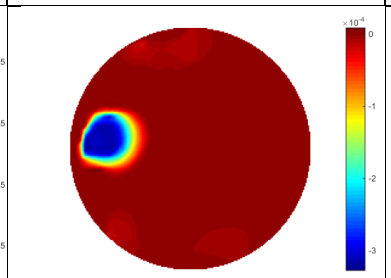	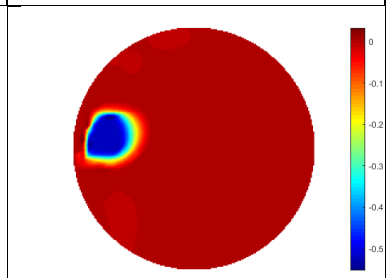
2	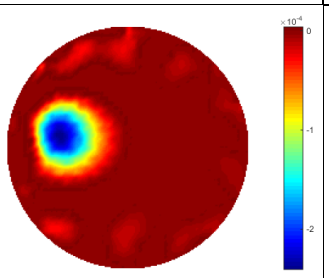	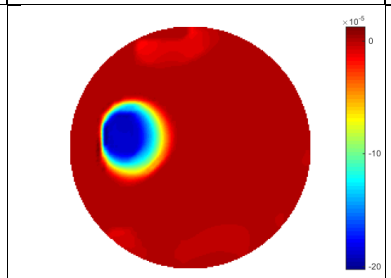	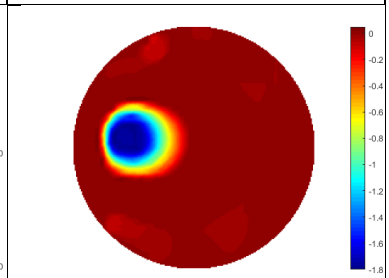
3	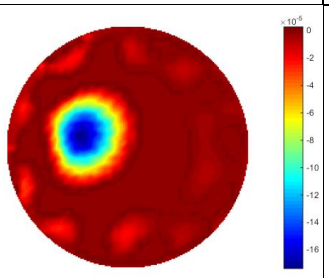	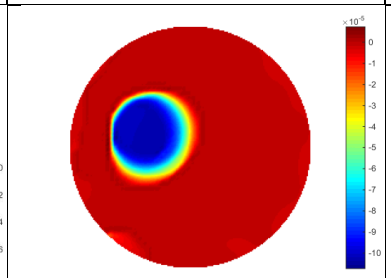	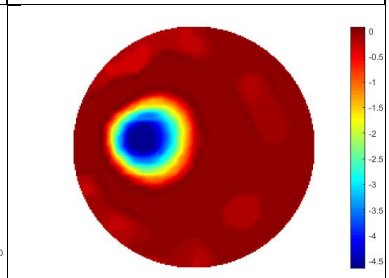

4	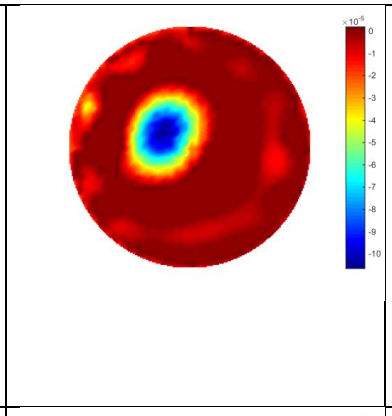	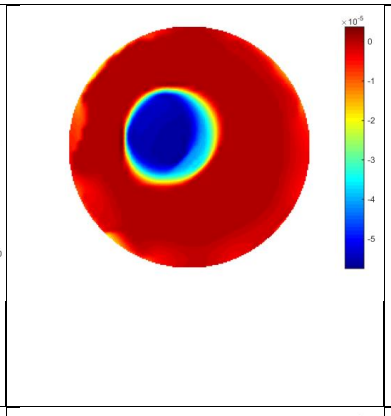	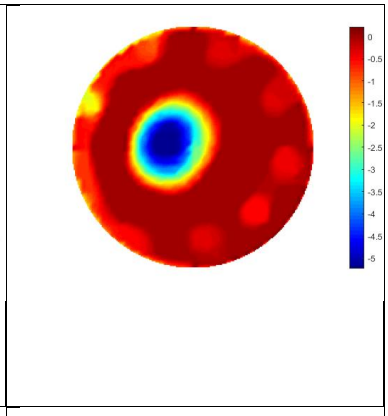
5	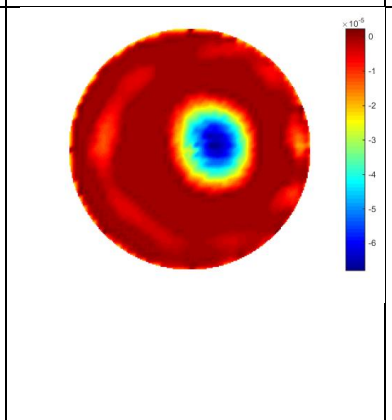	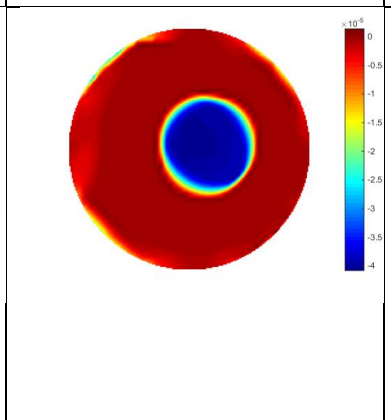	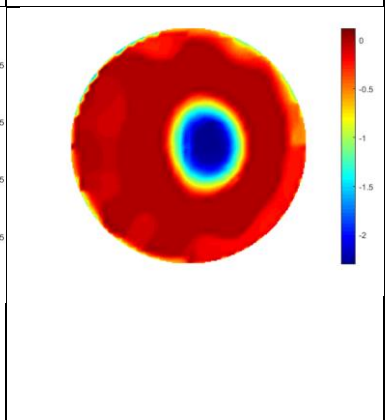
6	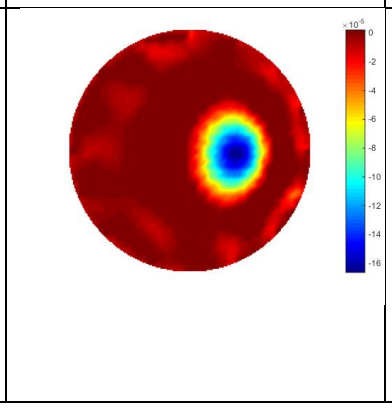	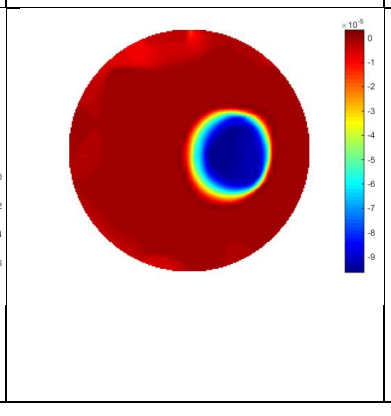	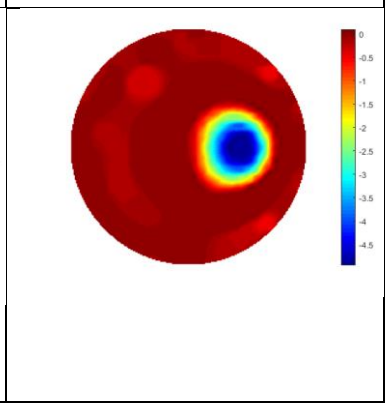

From the results that displayed on both Tables, it could be found that the moving process is monitored successfully with three different algorithms, and results are keeping consistent with the movement of the plastic bar within the tank. Regarding the quality of reconstructed images, images from using STTV have sharp object boundary and very smooth inside the object or on the background area, while images of using TOS have blurred object edge. In terms of reconstructed images of SBTV, images that near the boundary of the region are quite sharp, but degraded in the center area where the sensitivity is low. In terms of the performance of the temporal domain, many previous work using the methods to produce dynamical images with individual frames of data. However, what can be seen from

the Table is the object is keeping consistent on its shape with both algorithms without any streching along the movement direction.

- Test 2 Circular movement

The implementation of the circular movement is similar to the Test 1, where same excitation current value, frequency are employed. Data collection speed of 50 frames/second has been used for the boundary data measurement. The bar was moving clockwise along the circle that close to the boundary and start with the location at the bottom that showing in figure 4.2 (b). There are 530 frames of boundary collected with about 150 frames of background data. In terms of the implementation of using STTV algorithm, only effective data can be used as it is not a frame-by-frame anymore. Reconstructed images from STTV and TOS are compared in the Table below. Reconstructed images by using SBTV is displayed here for making a reference. The reconstructed images in this type of movement are quite stable compare with the result from cross movement test. From these pictures, STTV still shows a better sharpness and a more smooth background than TOS.

In conclusion, all algorithms show good performance on dynamical test regarding the visualizations. In comparison, images of using temporal-based algorithms are showing consistence, and images reconstructed using STTV indicates better quality due to its sharpness and less noisy of the images. However, the discussions in this chapter are based on visualizations only. To further support the good performance of STTV, some parameters about exploiting spatial and temporal information will be calculated, and some quantitative analysis based on these calculation will be carried out.

Table 4.3: Reconstructed images from circular movement test

NO.	TOS	STTV	SBTV
1	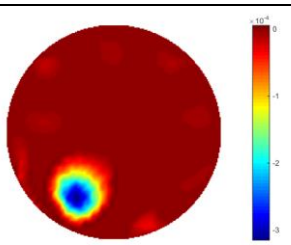	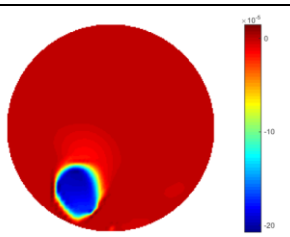	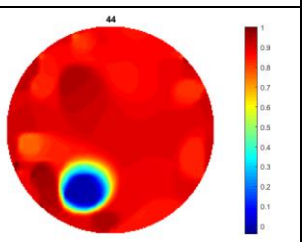
2	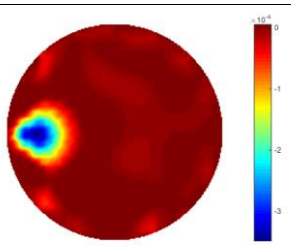	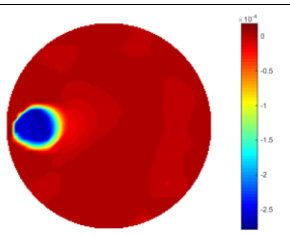	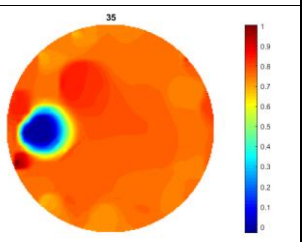
3	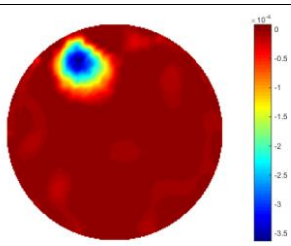	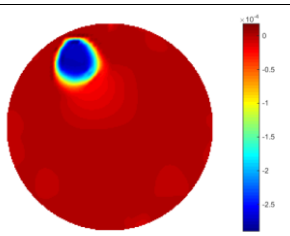	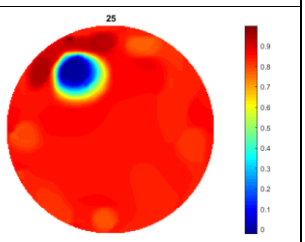
4	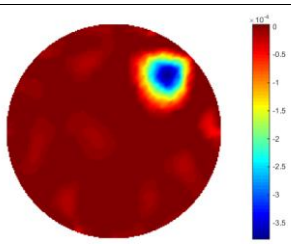	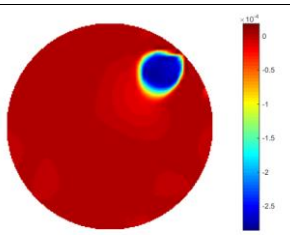	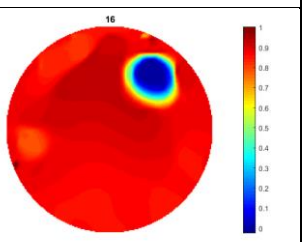
5	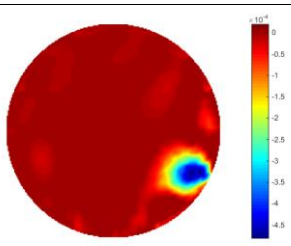	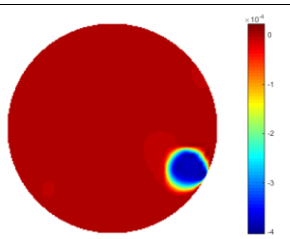	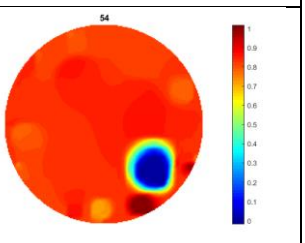

6	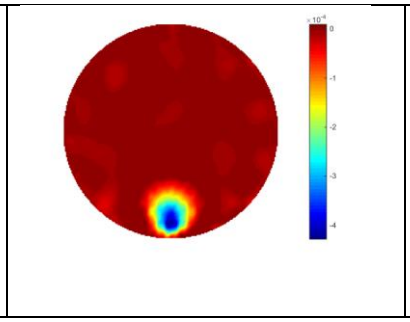	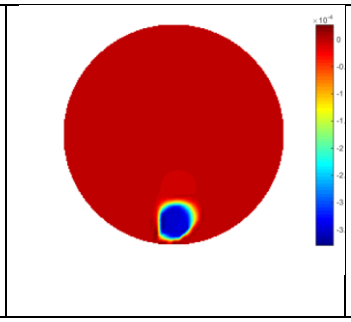	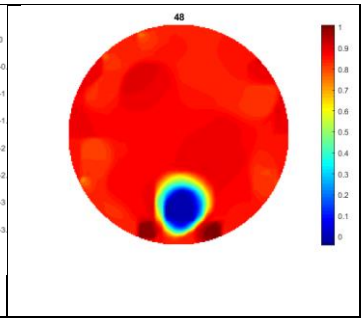

4.4 Analysis and Discussion

As what has been shown in the last section, images generated from TOS algorithm are slightly suffering from the blurred boundary of the recovered object, but STTV could produce higher-quality images, as those image benefit from its sharpness and less noisy. To analyze the advantages and drawback of both algorithms, in this section, some quantitative information would be extracted and displayed to compare two algorithms. The analysis would base on calculated results of the gradient, where spatial and temporal gradients are discussed separately. The time response is proposed and worked out for results from using both methods in order to further demonstrate how both contribute to the performance on time domain. Since frame-by-frame based SBTV algorithm does not consider any temporal information, temporal-based algorithms, STTV and TOS algorithms, are compared in the following sections.

4.4.1 Definition of Gradients and time response

- Spatial Gradient

In this chapter, the 2D image produced by temporal algorithms has a dimension of (x, y, t). The spatial gradient of an image means how the conductivity is changing in space, which would normally be calculated along a direction (x, or y) of each frame. The x/y-gradient could also be understood as the change of the slope value of the spatial distribution along x/y direction. For image u, the gradient of x and y-direction could be calculated by:

$$\nabla_x u \approx \frac{\Delta u}{\Delta x} \tag{4.1}$$

$$\nabla_y u \approx \frac{\Delta u}{\Delta y} \tag{4.2}$$

Where $\nabla_x u$ and $\nabla_y u$ are spatial gradient of x and y direction, and Δu is the conductivity step-change between 2 pixels. u is a slice of the image with 51 by 51 pixels, and $p = 51$. In this chapter, the magnitude of the gradient was calculated, which is given by:

$$\nabla_{xy} u = \sqrt{(\nabla_x u)^2 + (\nabla_y u)^2} \tag{4.3}$$

- Temporal Gradient

Temporal imaging is defined as dynamical image reconstructions along with the time series. Time gradient is describing the conductivity change along with the time series of a pixel, which is useful for evaluating the dynamical performance as it describes the step changes of the whole variation process. The time gradient of dynamical image could also be explained as the variation of the variations of conductivity in a pixel in the time domain. The dynamical process of the object could react to the temporal change in pixel values.

If we extract pixel values along time sequence, the conductivity change on this pixel would be plotted as a 1-D line graph, where the pixel value variation could illustrate the circumstance of the object movement. The temporal gradient could be defined as how much variation has been made on each time step with the time sequence, which is also a discrete gradient as data set is combined with individual frames of data, although they are time correlated. The gradient on time could be calculated by:

$$\nabla_t u \approx \frac{\Delta u}{\Delta t} \tag{4.4}$$

- Time Response

Time Response is defined by how fast it is capable of reacting to temporal change, which could be used to determine the dynamical performance of the result quantitatively. Regarding the temporal change in a pixel that the inclusion has experienced during the moving process, the algorithm that shows faster response would be an optimal choice. The

expression of Time Response could be given by a time interval that corresponds to where the conductivity decay from the background value to the peak value.

4.4.2 Spatial and temporal gradients

- Spatial imaging

In the Tables 4.4-4.6, there are few items are displaying here: images of the spatial gradient, 1-D plots of spatial distribution and the corresponding plots of the spatial gradient. There are 3 Tables in this part, where 3 slices are extracted for the analysis.

For an ideal case, the boundary of the object is supposed to be clear, so the spatial distribution on the object boundary is expected to be sharp, and the whole object area and also the background should remain at its corresponding conductivity values. A 1-D Plot of Spatial distribution of a perfect ideal case would show a square-shape wave, which results that only two sharp changes would be seen between the object and background. Some comparisons have been made between STTV and TOS algorithms, as displayed in the Tables 4.4-4.6.

From the images of the spatial gradient on three different positions (the data has been used in this part are consistent with the tests in the last chapter) within the tank, regarding the results using TOS, the object area is unevenly distributed in the images of spatial gradient distribution, however the results from STTV are showing very clear object boundary. The comparison of the conductivity distribution is given by the 1-D plot in the third row of each table, where images have been normalized in order to make contrast. The blue and red colored line in the plotted line graphs is indicating the result that recovered from STTV and TOS respectively about the spatial distribution and gradient changes. It could be seen from the conductivity distribution using TOS that the lowest value is always in the middle of the wave, and it is dropping down gradually and come back up slowly again, which indicates unclear boundary between the background and the object, as it would be hard to recognize where exactly corresponds to the boundary. The plots from STTV are given by nearly square-shape waves. The plotted line is always keeping flat either in the background or the object

Table 4.4: Spatial gradients of the results produced from STTV and TOS algorithms

Algorithm	TOS	STTV
Spatial gradient	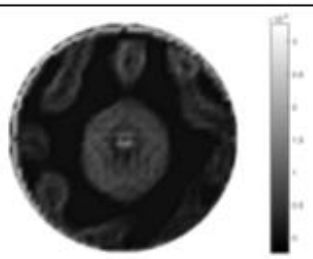	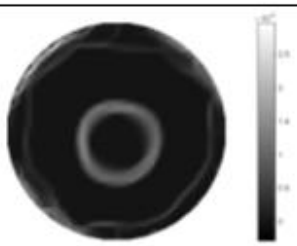
1-d plot of spatial distribution	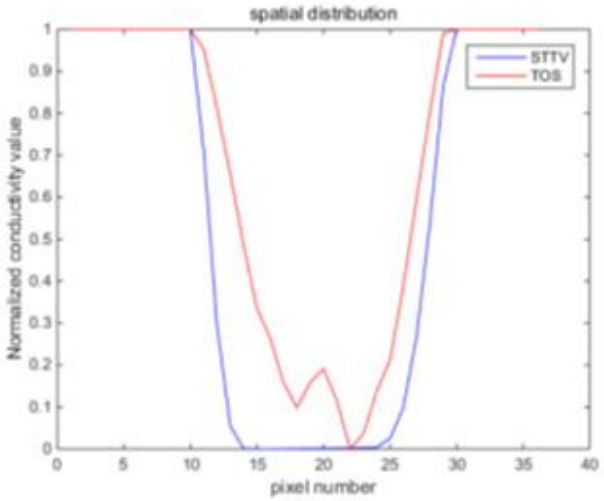	
1-d plot of spatial gradient	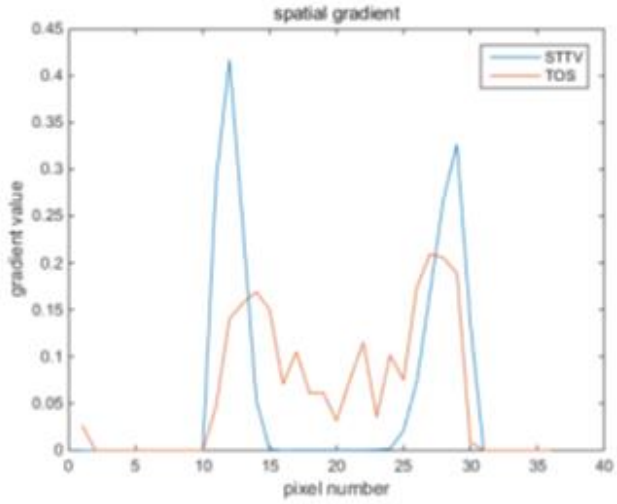	

area, and a very shape change is observed between the background and the target. The last graph is showing the comparison of the spatial gradient, in which the plots of STTV always display two sharp change which has the same wave shape of the

plot from the true image, but the gradient plot of TOS result are deforming due to its less sharpness of the recovered target.

Table 4.5: Spatial gradients of the results produced from STTV and TOS algorithms, where the reconstructed object is coming to the second position.

Algorithm	TOS	STTV
Spatial gradient	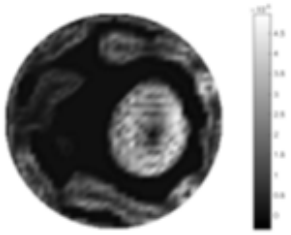	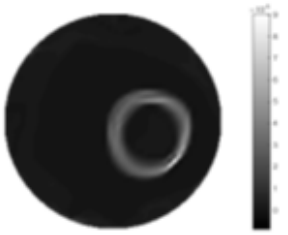
1-d plot of spatial distribution	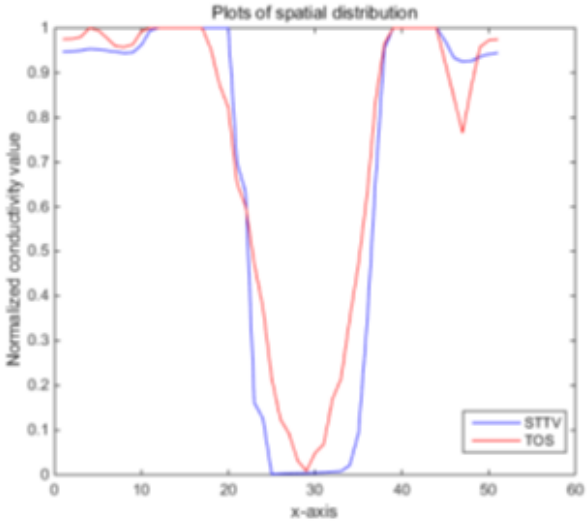	
1-d plot of spatial gradient	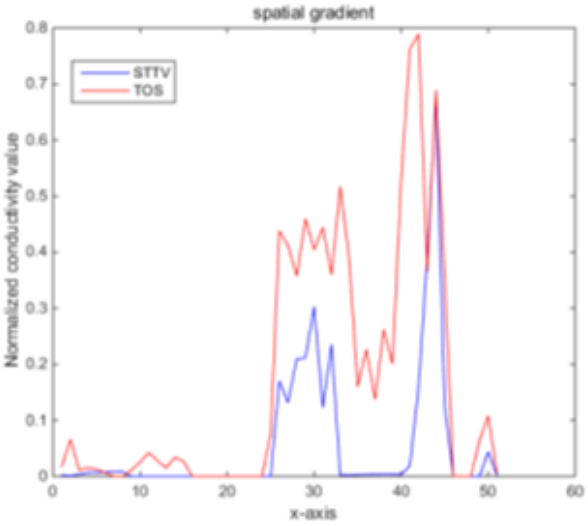	

Table 4.6: Spatial gradients of the results produced from STTV and TOS algorithms, where the reconstructed object is coming to the edge of the domain.

Algorithm	TOS	STTV
Spatial gradient	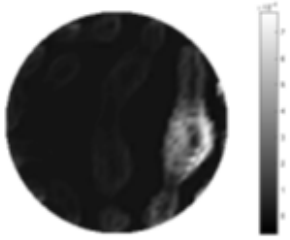	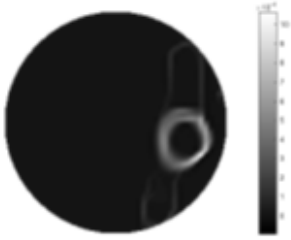
1-d plot of spatial distribution	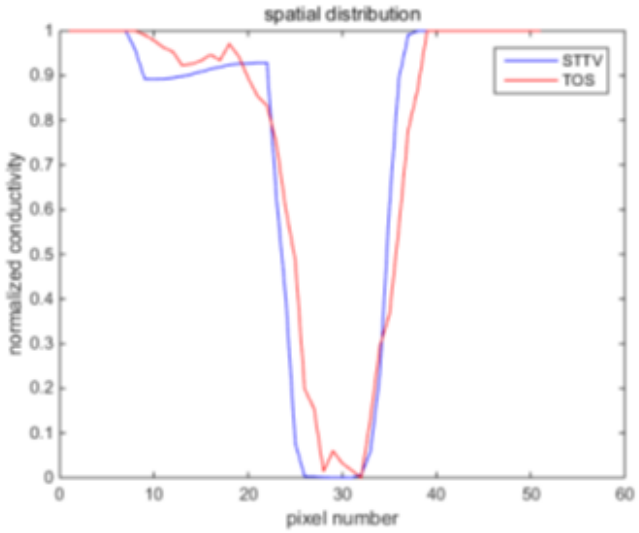	
1-d plot of spatial gradient	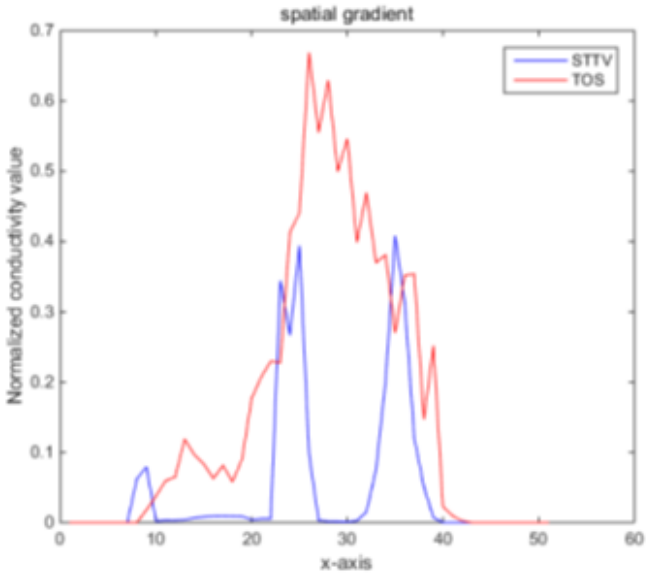	

- Temporal imaging

Reconstructed results from the cross and circular movement tests (images has been shown in the last chapter) using TOS and STTV are displayed in this part for analyzing the spatiotemporal performance. First of all, the spatial and temporal gradient are displayed and compared. In addition, the temporal variation of both dynamical setting using two different algorithms has been taken into account for discussing the time response.

In fact, the spatial gradient is the change between the current pixel value and the next neighboring pixel value along the defined direction, whilst the temporal gradient is the variation between two adjacent frames (variation along with the time series). The images of gradients in this section are based on a random frame N during the dynamical process, so the spatial gradient would be from the reconstructed image using frame N and the temporal gradient would be the difference between image numbers N and (N+1). According to the results of gradients, on spatial, obvious change of the conductivity distribution along x, y directions could be observed with a clear boundary between the background and inclusion. On the background or inside the object area, the conductivity variation between consecutive pixels is very small as it could be seen that the spatial gradient in this area is tend to 0. By comparing with TOS, results showing that the object is observable and recognizable, however, the conductivity value keeps changing inside the object in both directions, and the less sharpness of the boundary indicates the graduate variation between the background and the inclusion.

Regarding the temporal change between adjacent frames, relatively small variation between consecutive frames should be shown in the temporal domain due to a high data collection speed has been employed. In this case, it would be expected a very little shift on the object boundary, and almost zero change should be detected in the rest of the domain the consecutive frame data should be very similar. As shown in the figures of both dynamical movement type that STTV results are proved that it is more immunity to the noise, and its change in the time domain is more consistent compared with the results of TOS. In terms of the decay of the absolute spatial/temporal gradient that based on the gradient images in the second row of the table, the line graph of the result using STTV is showing faster decay than the one using TOS method. The plot of decay is actually

displaying the extent of the variation from the maximum value to 0, which numerically indicates the performance of spatial and temporal change between neighboring frames. This result is quantitatively demonstrating that STTV would potentially reconstruct high-quality images of dynamical case.

- Circular movement

Table 4.7: The results of spatial and temporal gradients of circular movement test using STTV and TOS algorithms.

	spatial gradient	temporal gradient
TOS	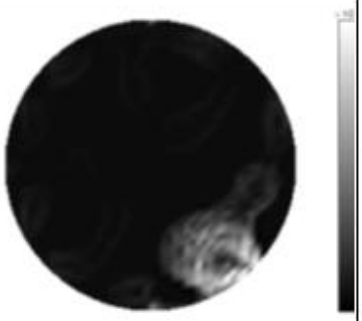	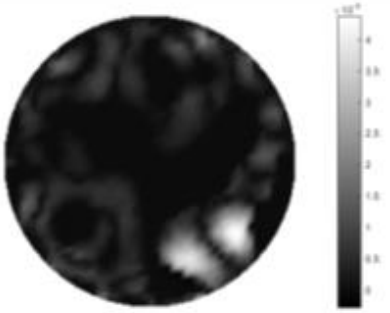
STTV	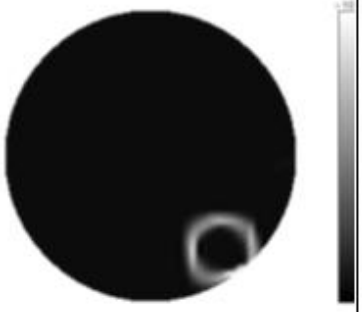	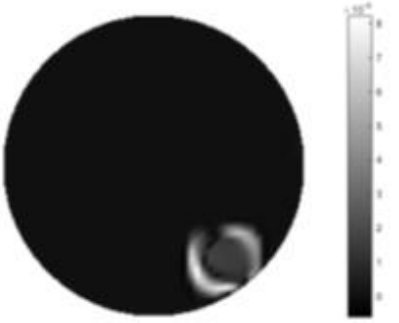

Decay of coefficients in spatial	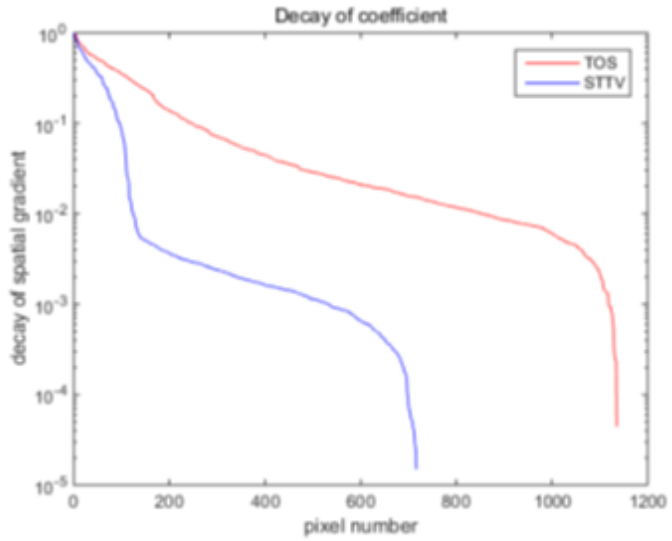
Decay of coefficients in time	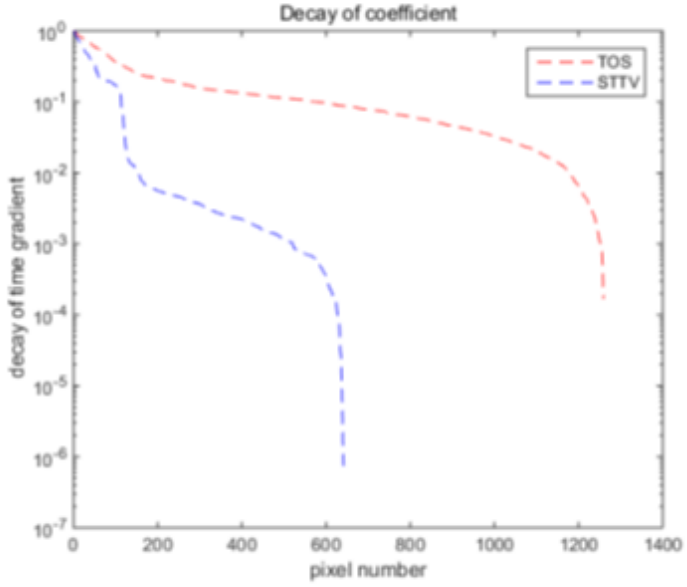

- Cross movement

Table 4.8: The results of spatial and temporal gradients of cross-movement test using STTV and TOS algorithms.

	spatial gradient	temporal gradient
TOS	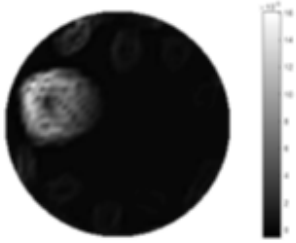	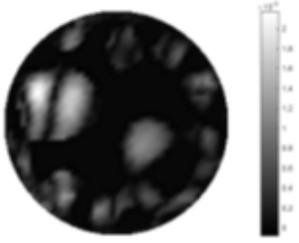
STTV	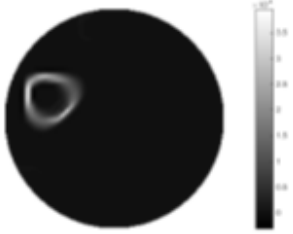	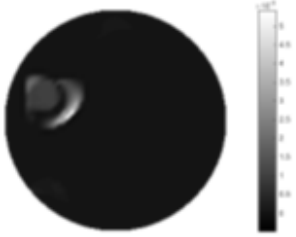
Decay of coefficients in spatial	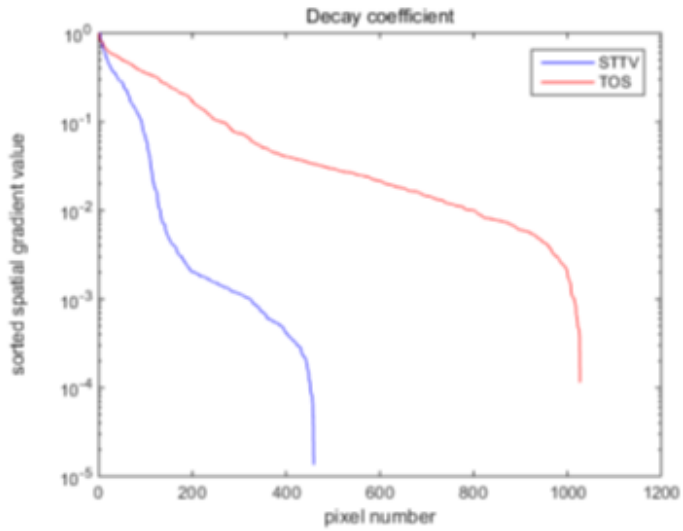	

Decay of coefficients in time	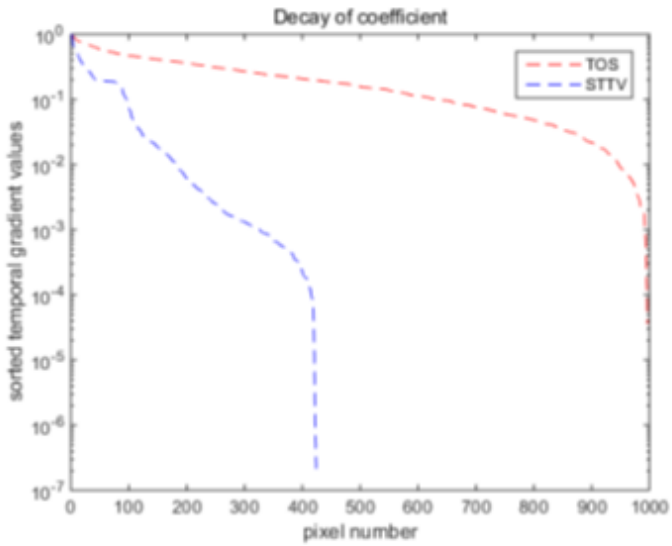

4.4.3 Time response

To further illustrate the performance in the time domain, the conductivity variation on pixels along the time series has been emphasized and taken into a further study about the time response. During the dynamical process, when the inclusion come to and then left a pixel, a dynamical change on such pixel would be generated. For a tomography-based control system, it will be quite important that whether an algorithm could well react to a moving inclusion or not, as a timely response is definitely required for making a decision and taking implementation in a proper time.

Based on the results from two dynamical movements using both algorithms, conductivity changes along the time series from selected pixels as well as the corresponding temporal gradient are showing in the below two figures. From the time variation plots of both results, it is obvious that they are displaying how fast the conductivity is varying from maximum value (corresponding to the background conductivity) to nearly zero and back up again, where 0 indicates when the object went through the pixel. In comparison, STTV would take slightly shorter to meet its lowest. Numerical calculations of response time of both algorithms are worked out. In the cross movement, the displayed results are from using the data collection speed of 24 frames/second. The response time of both algorithms, in terms of the case that the object entering the pixel, is 2.12s and 3.21s, and in the other

movement, the frame speed of 50 frames/second has been used, and STTV shows a time of faster response than TOS. The results stated above indicates STTV got a faster response to the conductivity change in the time domain.

- Cross movement

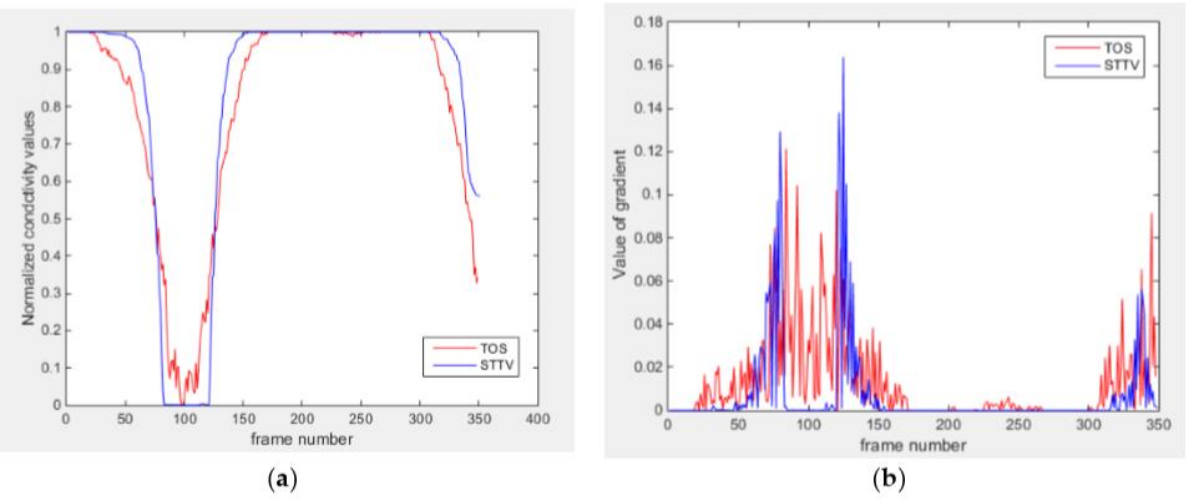

Figure 4.3: Results of time variation and temporal gradient. (a) time variation of a pixel extracted from the results of the cross movement (b) the plot of the corresponding temporal gradient. The red line stands for the result from using TOS, and the blue line indicates the results of STTV.

Table 4.9: time response of both algorithms from testing the cross movement

Algorithm	**STTV**	**TOS**
Time response	**2.12s (49 frames)**	**3.21s (77 frames)**

- Circular movement

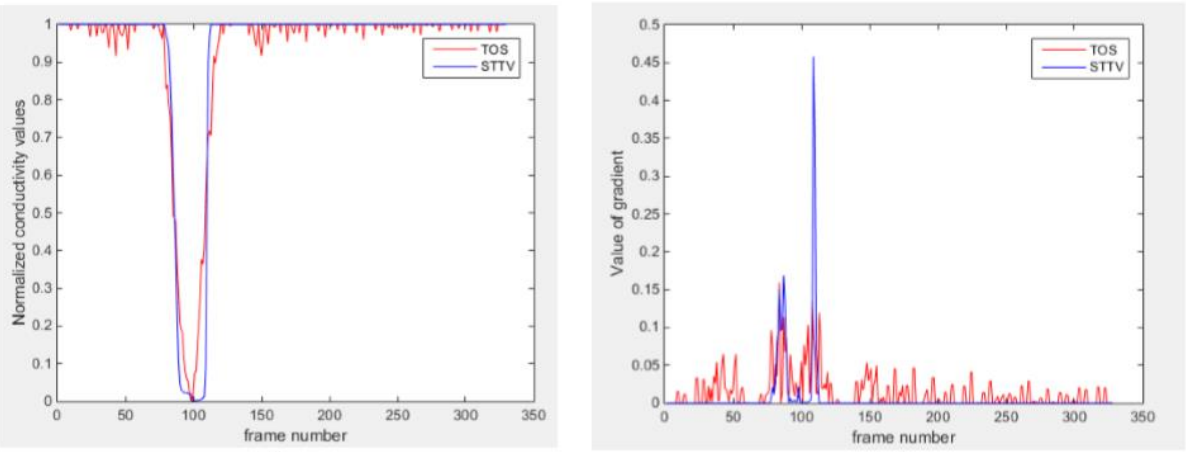

Figure 4.4: Results of time variation and temporal gradient. (a) time variation of a pixel extracted from the results of the circular movement (b) the plot of the corresponding temporal gradient. The red line stands for the result from using TOS, and the blue line indicates the results of STTV.

Table 4.10: time response of both algorithms from testing the circular movement

Algorithm	**STTV**	**TOS**
Time response	**0.26s (13 frames)**	**0.52 s (26 frames)**

4.5 Conclusion

Dynamical imaging is a very important topic to be investigated due to the fact that there are many requirements regarding moving objects inside the bounded domain in real life for monitoring and systematic controlling purposes. ERT benefits from its high temporal resolution, and would potentially have temporal information to be exploited along with the time domain. In terms of the reconstruction algorithms, the ones using individual frame data are not optimal, as it would ignore the dynamical change and the variation on each time steps. Although it is still capable of showing current positions, individual-image based results do not include any temporal information, in other words, it is showing lots of single

images instead of ‘movie’. Therefore, a temporal algorithm is a better choice as it regularizes ERT image with spatial and temporal information.

In this chapter, we investigated the performance of 2D dynamical movement using laboratory-based experimental data. To evaluate both spatial and temporal performance of STTV algorithm, results from using both STTV and TOS regularization methods are displayed for making comparison. In spatial domain, both algorithms show good performance, but TV-based temporal algorithm preserved the edge of the target. According to the analysis of dynamical experiments results, it could be concluded that STTV would generate sharper and less noisy images, but both algorithms showing the consistent result to the movement. However, the parameter selection is still required for STTV to be studied in future work, and it would have the potential to upgrade visualization results. Performance in the time domain of both methods was emphasized compared using temporal gradient and response time, where STTV shows a faster response time on the dynamical change of conductivity based on the quantitative calculation of time response of different dynamical movement. Time response would be an important parameter for evaluating a process tomography, and it can describe how fast the algorithm can react to the dynamical change of the target, which can provide a quantitative reference time to system. Sharp images would be preferred as it closer to the actual situation. This study can be extended to a real two-phase flow system for visualization and control purposes, and high-quality flow visualizations would potential contribute to more accurate flow measurements.

Chapter 5 ERT for velocity profile using STTV Algorithm

Electrical resistance tomography (ERT) has been considered as a data collection and image reconstruction method in many multi-phase flow application areas due to its advantages of high speed, low-cost and being non-invasive. In order to improve the quality of the reconstructed images, the Total Variation algorithm attracts abundant attention due to its ability to solve large piecewise and discontinuous conductivity distributions. In industrial processing tomography (IPT), tomographic techniques have been used to extract important flow measurement information. For a moving object inside a pipe, velocity of the target can be calculated from the cross-correlation between with ERT sensors. Some previous proposed image-based method has used two sets of 2D ERT measurements and produce two images simultaneously from both electrode-plane, and velocity measurement is based on pixel-to-pixel cross-correlation. This method requires a double-channel ERT system working with dual-plane electrode patterns. In this chapter, a method for carrying out flow velocity measurement using a single-channel ERT system is proposed. A novel spatiotemporal total variation regularization approach is utilized to exploit sparsity both in space and time in 4D, and a voxel-voxel cross-correlation method is adopted for measurement of flow profile. The result shows that the velocity profile can be calculated with a single ERT system and movement can be monitored using the proposed method. This study is a laboratory-based phantom test. Both static simulation studies and semi-dynamic experiments conducted by tank verify the suitability of the proposed method. For in-plane velocity profile, a 3D image based on temporal 2D images produces velocity profile with an accuracy of less than 1% error and a 4D image for 3D velocity profiling shows an error of 4%. This work has been published in [45]

5.1 Introduction

In the process of production, transportation and distribution of fluids, in particular, in the petroleum industry, multiphase flow is commonly present. The measurement of velocities in different phases is an important factor and treated as quantitative controlling for cost

minimizing, risk reduction of the flow. The velocity profile measurement technique using electrical resistance tomography (ERT) and based on cross-correlation has been established for many years. ERT techniques are growing rapidly with the fast development of computing power. In particular 3D ERT, which is now feasible as a non-invasive detection method, where the interior distribution can be displayed with high-speed data collection. ERT could be applied to several fields that could benefit from its property of being non-invasive, low cost of the hardware system and good mobility.

Electrical Tomography and cross-correlation based flowmeters are ideally suited for measuring multiphase flows and have been adopted in the past few years [127]. Many applications have been suggested, for example, B Gurau and P Vassallo [128] proposed the use of cross-correlation to calculate the phase velocity of air-water two-phase flow, from the output signals of hot-film probes, and A. Saoud, V. Mosorov [129] utilized cross-correlation with ECT in velocity measurements of gas/solid swirl flow. Some of the previous research about velocity profile was based on 2D ERT with a dual-plane model, where a double-channel ERT system was applied and cross-correlation was used between outputs signals obtained from two electrode channels. X. Deng and F. Dong (2001) [104] designed a dual-plane system for the measurement of gas and liquid bubbly flow. With the extracted eigenvalue of the data from the gas/liquid flow in the vertical pipe, the dispersed phase velocity was measured accurately by F. Dong, Y.B. Xu [105] in 2005. Y Wu and H Li (2008) [106] compared the dynamic distribution and velocity among different flow regimes. However, the flow being measured is a 3D structured object, in other word, 2D modelling and measurement methods are apparently a simplification. Many contributions have also been made for 3D imaging with electrical tomography, such as, ECT [130] [131] and ERT [132], however, for many cases, especially ERT, 2D imaging technique are always considered for saving computational cost, and 3D ERT imaging may suffer from being more sensitive to error and high complexity. However, in some special cases, the information in the axis-direction is quite important and the simplifications of the 2D method may not be enough to describe what we are expecting. Although 3D image reconstruction is still challenging, it worth to put more effort into a 3D image that allows a more complete visualization on target under estimated.

We are particularly interested in a two-phase flowing system with liquid and heavy oil. For oil-in-water flow, oil-phase is possible to attach the wall of the pipeline. The flow velocity can be slow down, and the pipe can even be blocked if the oil on the wall accumulated. It is expected that the location of such an occurrence inside the pipe will be found using the capability of ERT 'to see inside'. When the fluid is transported, an average flow speed can be reconstructed with the position of the inclusion. In the industrial process, the flow velocity is controlled within a reasonable range to ensure normal operating conditions of flow system. ERT can provide a numerical reference of mean speed with the measurement of the velocity profile, the situation could be recognized and amended promptly. In addition, the visualization capability of ERT can also provide information on the phase distribution interior of the pipe for monitoring the flowing process.

In this chapter, we present a new method using a single-channel ERT system in temporal 2D imaging mode for 2D flow visualization and angular speed, and in temporal 3D ERT (4D) mode for axial velocity measurement. In the last chapter, good time response of STTV has been discussed. Therefore, the spatiotemporal TV algorithm is employed for dynamic flow visualization by ERT image reconstruction, and together with a cross-correlation for velocity profile calculation. Simulation was carried out for feasibility study, and experimental validations are conducted by detecting a moving sample in the laboratory phantom. Cross-correlation was used based on reconstructed images for calculating the flow parameter. In order to analyze the cross-correlated result, the actual speed was measured experimentally, and the relative error was calculated and further discussed.

5.2 Method

Time difference ERT temporal imaging has been conducted in this chapter. The linear inverse problem in ERT can be defined as the recovery of a change in conductivity $\Delta\sigma$ from a change in measured boundary voltage Δu, where $\Delta u = J\Delta\sigma$. The Jacobian J is computed by the Fréchet derivative of u with respect to σ as demonstrated in subsection 2.2.d. In this case, a reference boundary voltage u_0 is available from measurement on background, and

data u_i is given by the target with the background medium, where $u_0 = f(\sigma_0)$, $\Delta u = u_i - u_0$ and $\Delta\sigma = \sigma_i - \sigma_0$.

In a 4D flow imaging situation, the unknown conductivity changes and data are 4D objects, where time-varying conductivity in 4D dynamical ERT can be described by $\sigma(x, y, z, t)$. Redefining the conductivity and data, we have $\Delta\sigma = [\Delta\sigma_1, \dots, \Delta\sigma_n]$ and $\Delta u = [\Delta u_1, \dots, \Delta u_n]$ to allow $\Delta u = \tilde{J}\Delta\sigma$ valid for a number of temporal frames of n. The temporal TV algorithm is capable of correlation the information with consecutive frames, and it regularizes the conductivity mapping in the spatial and temporal domain. Detailed information on STTV algorithms with ERT inverse problem is demonstrated in section 2.3.3.

5.2.1 Cross Correlation for Velocity Profile

A signal processing method termed cross-correlation can demonstrate the relationship of the time series by calculating the cross-correlation function and discover where they are best correlated where corresponds to a highest-similarity element. The most similar element can suggest the time lag of that two time series [27] [127]. In terms of time series $x(t)$ and $y(t)$, the cross correlation function C_{xy} describes the similarity extent defined as:

$$C_{xy}(\tau) = \lim_{T\to\infty} \frac{1}{T} \int_0^T x(t).\ y(t+\tau)dt \tag{5.1}$$

In practice, the time period cannot be infinite, and the equation can be modified without a limitation, and cross-correlation of both signals on time period of T is described with:

$$C_{xy}(\tau) = \frac{1}{T} \int_0^T x(t).\ y(t+\tau)dt \tag{5.2}$$

Such a technique has been adopted for flow metering, and quantitative velocity profile of two-phase flow has been developed applied to ERT with dual-plane electrode sensor. In terms of an image-based system, such characterization based on cross-correlating the time series from pixels or voxels termed pixel-pixel or voxel-voxel cross-correlation for 2D and 3D ERT imaging, which produces the velocity between pixels of a cross-section or voxels from different 'layers'. The term pixel/voxel is distinct with pixels/voxels of images, but regions composed with image pixels/voxels. Cross-correlation is actually capable of determining the transit time that the moving object travels through the region. Movement is featured on temporal images and characterized on pixels/voxels, and the mean velocity is quantitatively

determined by known distance. In terms of the problem mentioned in this chapter, the discrete cross-correlation function of series x and y is defined as follows:

$$C_{xy}(m) = \frac{1}{N}\sum_{n=1}^{N} x(n\Delta t)y(n\Delta t + m\Delta t) \quad (5.3)$$

Signals x and y are corresponds to the time series of two elements composed with characteristic value from two images. N is the length of vectors equivalent to the time period, and Δt gives time-step depending on data collection rate of ERT system. The transit time is determined by $m\Delta t$.

The procedure of cross-correlation that has been used in this chapter has the following steps:

1. Image reconstructions of the entire dynamical process, resulting images of $\Delta\sigma(x, y, t)$ or $\Delta\sigma(x, y, z, t)$
2. Definition of each pixel or voxel region by domain separation, where the region of 2D images has segmented by 4×4 pixels and 3D images have been separated into voxels of $3 \times 3 \times 3$ (see figure 5.2(a) and 5.10(b)).
3. The characteristic value extracting from each pixel or voxel. (In this chapter, the characteristic value is given by the average value of σ within the area. In each frame, a characteristic value is calculated from each separated 'pixel', so a vector of length N is given by dynamical reconstructed images with N frames in each pixel.
4. Characteristic value vectors are composed of pixels or voxels
5. Pixel-to-pixel cross-correlation or voxel-to-voxel cross-correlation conducted by function (5.1) to find out the transit time from position 1 to position 2. Plot cross-correlation equation between two output vectors and find out frame number **m** on the peak. The transit time is determined with $\mathbf{m}\Delta t$
6. The experienced distance L is determined by the defined imaging region. In this chapter, the vertical distance experienced by the target is defined as 13cm.
7. Velocity profile calculation

The acquired transit time τ corresponds to the peak of the plotted cross-correlation function $R_{xy}(\tau)$. For the case of 16 pixels (2D) and 27 voxels (3D), the velocity profile is given by

$$v = \left[\frac{L}{\tau_1}, \frac{L}{\tau_2}, \cdots, \frac{L}{\tau_k}\right] \tag{5.4}$$

$where\ k = 16\ (2D) or\ 27\ (3D)$.

In this chapter, the average speed of the moving inclusion was calculated and made a comparison between different algorithms. In this case, the speed is given by:

$$v = \frac{distance}{transit\ time} = \frac{Height}{m\Delta t} \tag{5.5}$$

where Height is given by the size of the z-axis of the defined domain, as showing in figure 5.1.

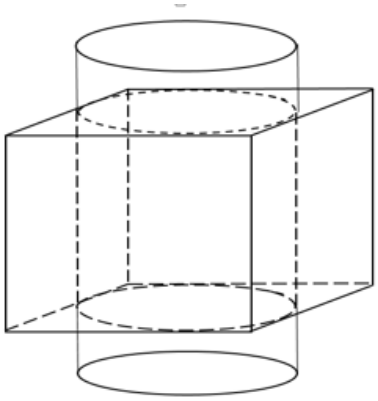

Figure 5.1. The illustration of the ERT visualization domain within the cylinder tank

5.3 Tests and results

In this section, the setting up and procedure of simulation and experiment in both 2D and 3D situation are demonstrated in details, and the results of each part, including reconstructed images and speed calculation, are displayed and will be further discussed in the following sections. The purposes of this section are feasibility analysis on dynamic model monitoring and velocity profile measurement. The proposed Temporal TV algorithm will be used for reconstruction with consecutive frames containing time-related information. In addition, pixels, and voxels, in both 2D and 3D case, will be defined as a specific area in each frame, where the output signal from each of them is composed with extracted characteristic values from every frame. Moreover, the pixel-pixel and voxel-voxel cross-correlation for 2D and 3D cases could be made with these characteristic value vectors in order to work out the speed.

Simulation process:

- Setting up the shape and size of the domain, electrode (size, number, and locations),
- Selection of excitation and measurement method
- Set up the conductivity value of the background (σ_0)and inclusion (σ_i)
- Set up the movement of the inclusion
- Solve a forward model based on FEM:

  Step1. (Forward_model.nodes, Forward_model.elements)=FEM_SOLVER(shape, electrode_position, electrode_shape, stim_pattern, meas_pattern);

  Step2. Vh=BOUNDARY_DATA(σ_0, Forward_model);

  Step3. Vi= BOUNDARY_DATA(movement, σ_i);

  Step4. Data=Vi-Vh;
- Jacobian calculation
- Image reconstruction based on the proposed algorithm
- Using cross-correlation to find out the transit time (τ)
- Feasibility analysis of Speed calculation (v)

Experimental procedure:

- Phantom design according to the setting up
- Data acquisition
- Image reconstruction based on the proposed method
- Using cross-correlation with thresholding data to find the transit time
- Calculation of the speed of the moving inclusion with the transit time
- Analysis

5.3.1. Simulation in 2D

The simulation 2D test was setting up that the inclusion was moving continuously along a circle with a constant angular speed within a 2D circular model, where a 16-electrode circular sensor was applied. The migration path was divided into many steps, where 200 locations were selected homogenously along the path for image reconstruction on each location. The aim of this test is to investigate the performance of visualizations using STTV

algorithm, and the feasibility of speed determination. The forward model was constructed using EIDORS, where the injected current was setting at 1mA. The semi-diameter of the sensing field and the movement path are 7cm and 5cm respectively, and 1.5cm radius of the circular inclusion is simulated as a moving target. The conductivity of the background and object are 1 and 0 respectively. In order to calculate the velocity distribution through the pixel-pixel cross-correlation method, each frame of the image was divided into 16 pixels for characteristic value extracting. The distribution of the big pixels is shown in Figure 5.2(a). In Figures 5.2(b), the movement of the inclusion is demonstrated, and some reconstructed images using proposed algorithm are displayed in figure 5.3. Some plots of cross-correlation result and corresponding pixels are showing in figure 5.4, in which the first 4 plots on the top stand for the plot of cross-correlation results, and the ones below them are showing the plots of the corresponding pixels. These plots are showing the dynamic change of the object movement within each pixel. Satisfactory results are displayed in the top 4 plotted images and the frame number related with each peak value is consistent with the corresponding two pixel plots below them.

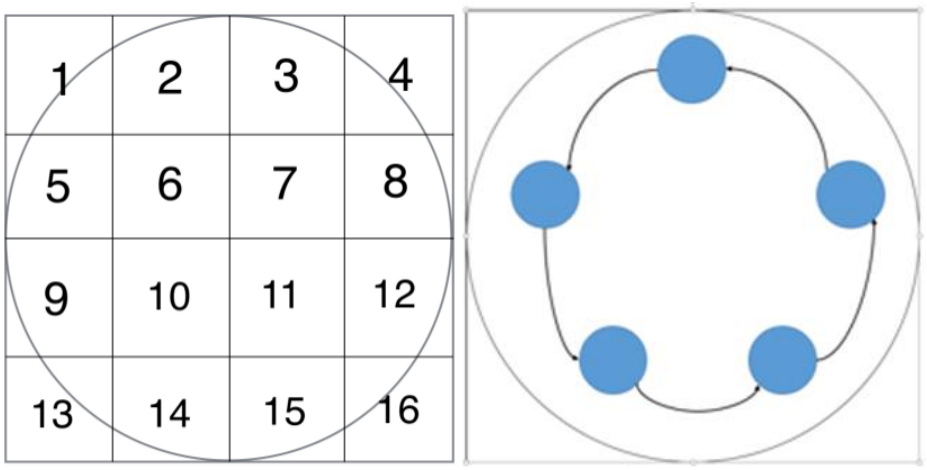

(a) (b)

Figure 5.2. Illustration of pixels and movement. (a) The image of pixel unit (b) The movement of the object in the simulated domain

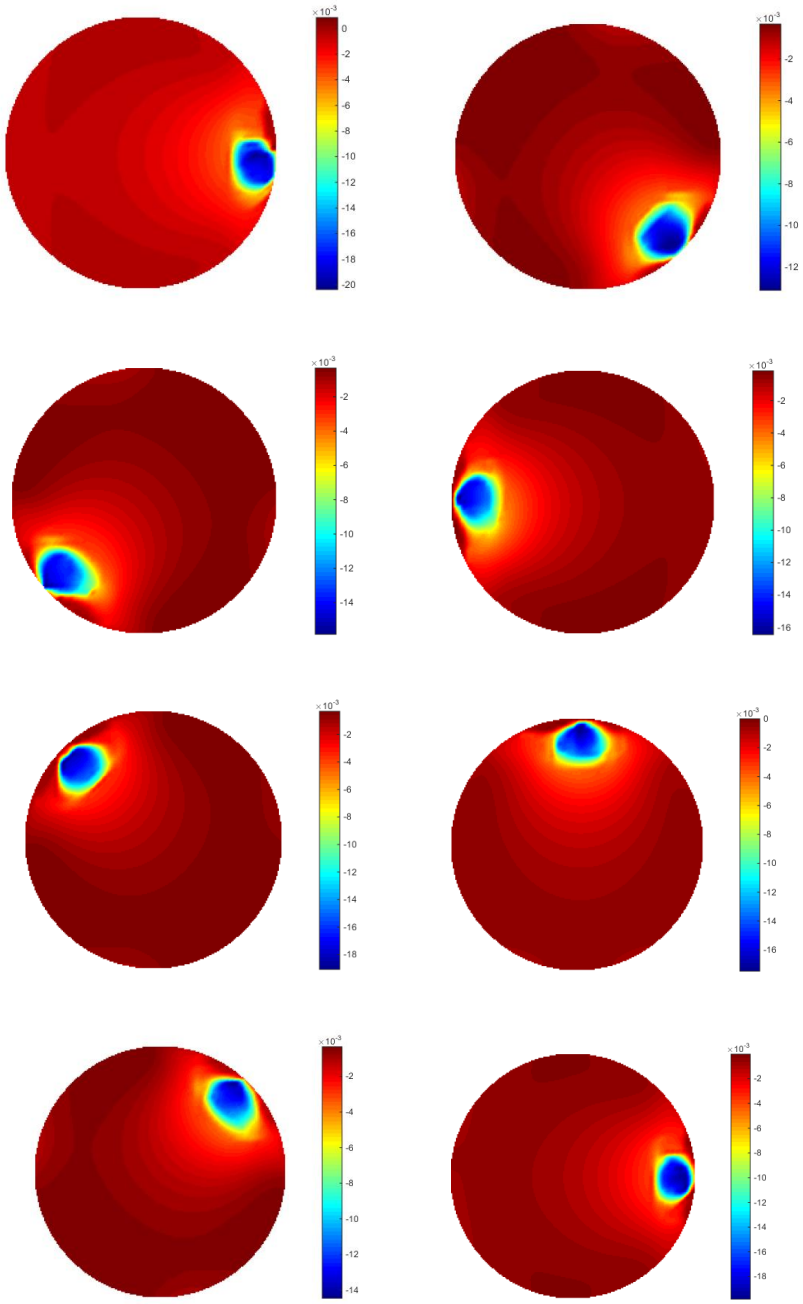

Figure 5.3 Reconstructed images of inclusion in the simulation test using Temporal TV

The transit time could be reflected from the frame number of the peak, as shown in Figure 4, The transit time could be reflected from the frame number of the peak, where the time-step between adjacent frames is known from the hardware system, and angular speed calculation is attainable. As a result, it is verifying the feasibility of movement monitoring

and speed calculating with the proposed algorithm. In the following part, some results from real data will be discussed.

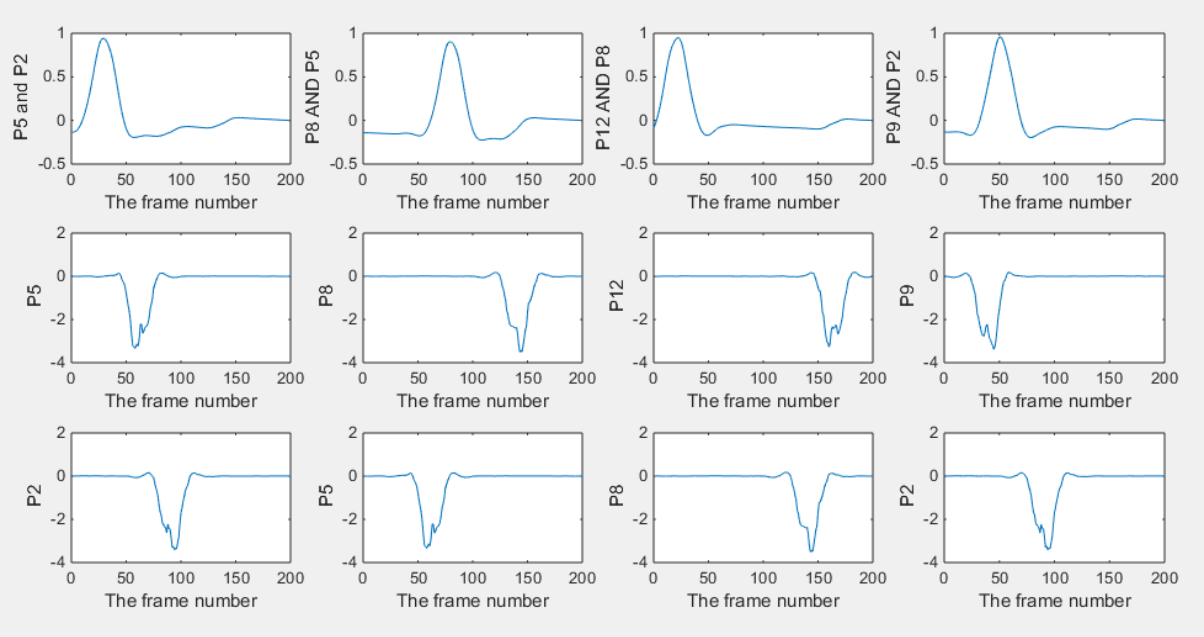

Figure 5.4. Plots of cross-correlation results and the corresponding pixels in the 2D simulation test.

5.3.2. Experiment in 2D

In this part, a series of data were collected from the continuous movement of the inclusion. The phantom adopted (showing in Figure 5.6), is a cylinder-shaped transparent glass container with an inner diameter of 14 cm, and a height of 25 cm. Rectangular shaped stainless-steel sheets (4cm x 3cm) were used as electrodes. Screws were utilized for the purpose of connection and proper fixing on the phantom. An extra screw was installed on the wall above the electrode ring to connect with the ground wire with the data collection system. To be consistent with the simulation, the model is kept to be the same size and same way of circular movement. In the 2D experiment, a plastic bar was used as inclusion and it was moving continuously along the inner wall of the phantom anticlockwise with R=5cm until it came back to the origin. There were 70 frames collected from the ERT KHU Mark 2.5 data collection system with injected current of 1mA and 10 KHz, where neighboring excitation and measurement method were used and 208 individual voltages in total were collected for each frame. The current injection pattern and voltage measurement pattern are summarized in Table 5.1. In this case, 70 corresponding images are produced. As

mentioned in the 2D simulation, Temporal TV algorithm was used for reconstructing images for proposes of movement monitoring, and angular speed calculation was conducted by cross-correlation.

Table 5.1. The illustration of current injection pattern and voltage measurement pattern

	EX 1	EX 2	EX 3	EX 4	EX 5	EX 6	EX 7	EX 8	EX 9	EX1 0	EX1 1	EX1 2	EX1 3	EX1 4	EX1 5	EX1 6
(1,2)	I	×	-	-	-	-	-	-	-	-	-	-	-	-	-	×
(2,3)	×	I	×	-	-	-	-	-	-	-	-	-	-	-	-	-
(3,4)	-	×	I	×	-	-	-	-	-	-	-	-	-	-	-	-
(4,5)	-	-	×	I	×	-	-	-	-	-	-	-	-	-	-	-
(5,6)	-	-	-	×	I	×	-	-	-	-	-	-	-	-	-	-
(6,7)	-	-	-	-	×	I	×	-	-	-	-	-	-	-	-	-
(7,8)	-	-	-	-	-	×	I	×	-	-	-	-	-	-	-	-
(8,9)	-	-	-	-	-	-	×	I	×	-	-	-	-	-	-	-
(9,10)	-	-	-	-	-	-	-	×	I	×	-	-	-	-	-	-
(10,11)	-	-	-	-	-	-	-	-	×	I	×	-	-	-	-	-
(11,12)	-	-	-	-	-	-	-	-	-	×	I	×	-	-	-	-
(12,13)	-	-	-	-	-	-	-	-	-	-	×	I	×	-	-	-
(13,14)	-	-	-	-	-	-	-	-	-	-	-	×	I	×	-	-
(14,15)	-	-	-	-	-	-	-	-	-	-	-	-	×	I	×	-
(15,16)	-	-	-	-	-	-	-	-	-	-	-	-	-	×	I	×
(16,1)	×	-	-	-	-	-	-	-	-	-	-	-	-	-	×	I

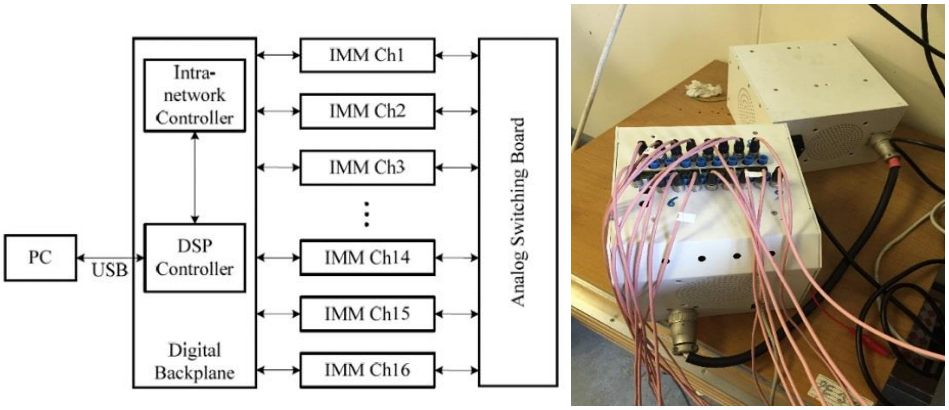

Figure 5.5: KHU Mark 2.5 Hardware system

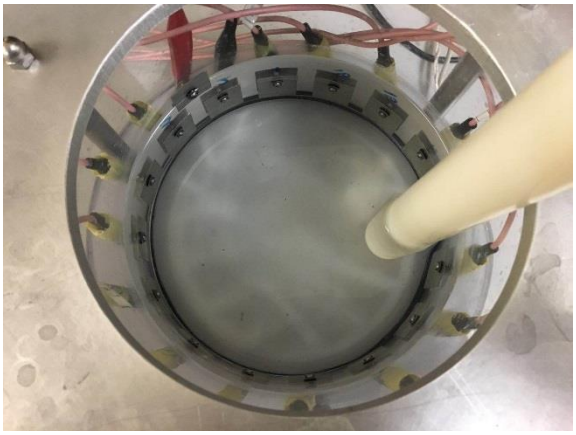

Figure 5.6 The experimental set up with the tank of 2D ERT unit with tap water as a background

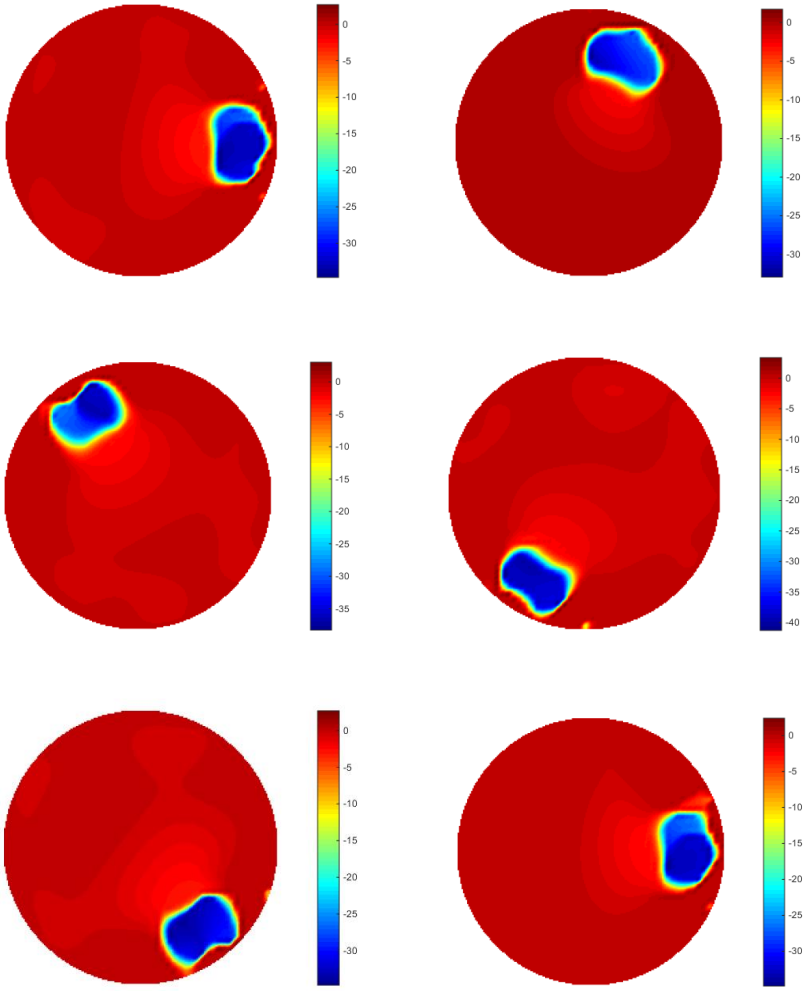

Figure 5.7. Image reconstruction of the 2D experiment using temporal TV

Pictures in Figure 5.7 is showing the result of the reconstruction (only 6 frames are chosen to be displayed here for illustrating the performance of monitoring). The objects that displayed in images got slightly bigger and overlapping comparing with the case of simulation, which would be caused by the generation of inter-frame data from the dynamical moving inclusion. In terms of the plotted line graphs of 16 pixels (Figure 5.8), they are displaying that the inclusion is moving from a location within pixel 12, then experienced most of the pixels (can be found from the peak value) along the phantom edge sequentially until it comes back again at its origin, which demonstrates the monitoring purpose was achieved. The result of cross-correlation is showing in Figure 5.9, where the peak value is indicating that 51 frames were collected during the bar moving through the whole circle. The transit time is 10.71s, which could be given by the system data collection speed. Assuming the moving route was a proper circle, angular speed can be calculated using 360 degrees and the corresponding transit time. The details of the speed calculation and error study are discussed furthermore in section 4.

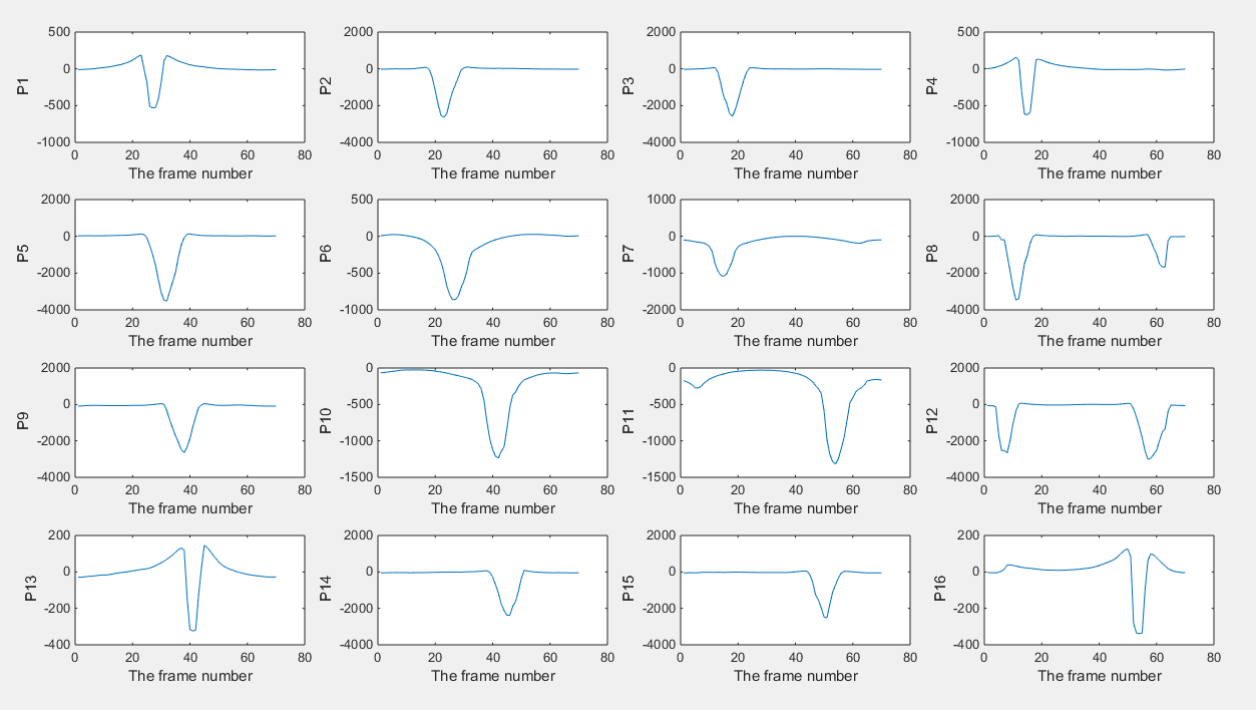

Figure 5.8. Plots of pixels of the result 2D experimental test with phantom inclusion in the ERT unit.

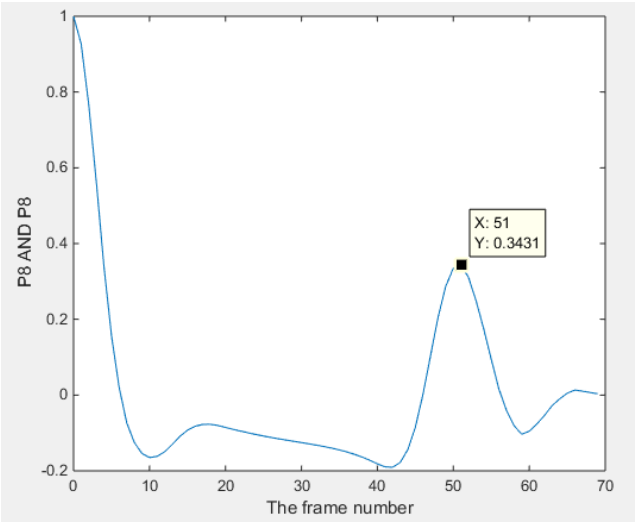

Figure 5.9. Plots of cross-correlated result between pixels

5.3.3. Simulation in 3D

In the 3D simulation test, a 16-electrode cylindrical 3D model with two rings of 8 electrodes was constructed, where the size of each electrode is 3cm×4cm. Two rings were located in a height of 9cm and 16 cm respectively. A neighboring data collecting method was selected for current excitation and voltage measurement. The forward model was built using EIDORS and 3D mesh was generated by NETGEN, where the injected current was setting at 1mA. The inclusion has been simulated is a sphere with a radius of 1cm, and the conductivity value was setting at 0 (non-conductive), while we set the conductivity value of the background at 1.

In the vertical direction, 71 locations of the inclusion were chosen evenly between (5, 0, 16) and (5, 0, 9), where it was assumed that the sphere was dropping 0.1cm down each step, and a frame (208 independent measurements) of the image is produced split into 27 voxels (3×3×3). The drawing of the experimental phantom and voxels distribution are showing in Figure 5.10. The procedure of cross-correlation for 3D is similar to 2D. For all voxels, a vector of length 71 (number of frames) could be composed of 71 average values from each of the frames, and there were 27 vectors generated in total. Frames are time-relate with each other, and the data collection speed of the ERT system and the overall velocity of the movement are both constant. Hence, 27 signals are generated. With the cross-correlation

method, the transit time between two different voxels comes to be available from signals of the different voxel, and the overall flowing speed could be calculated with distance.

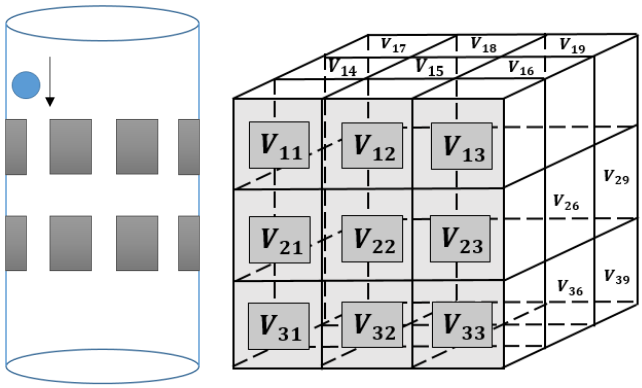

(a) (b)

Figure 5.10. (a) The movement of the inclusion in the 3D phantom (b) Distribution of 27 voxels within the domain

The aim of this test is to find out the feasibility of monitoring and velocity measurement in a 3D model. Based on the setting up of the simulation described above, 3D image reconstruction was conducted by Temporal TV algorithm. The reconstruction result is showing in Figure 5.11, where the overall situation of the sphere movement was being monitored as expected with the object moving down. We can see that the object is moving down gradually with the translocation of the inclusion, which demonstrates the good performance of temporal TV, although the objects in the middle seem weaker than the ones located on the top and the bottom. Comparing with 2D ERT reconstruction, it is obvious that the conductivity value of the object (refer to the color bar) was varying with the location of the inclusion going downwards, especially those that are located in the middle heights of the phantom, are especially suffering from low resolution. When the inclusion on the top and bottom of the domain, the color of the objects from images indicate more non-conductive character of the inclusion, and the character weaken when it came to the middle area, although the inclusion was always the same. The reason for this appearance could be that the intensity of the electric field in the center area is relatively weaker than the area close to the electrodes where the current injected. Noise, would potentially be produced especially in the experimental test, and could also weaken the character of the movement, which may lead to inaccurate result of cross-correlation. To eliminate noise, thresholding is

needed before the cross-correlation, where binary numbers were used instead of decimal data. In this case, 0 and 1 will be the only two values to appear in the matrix of the reconstructed images.

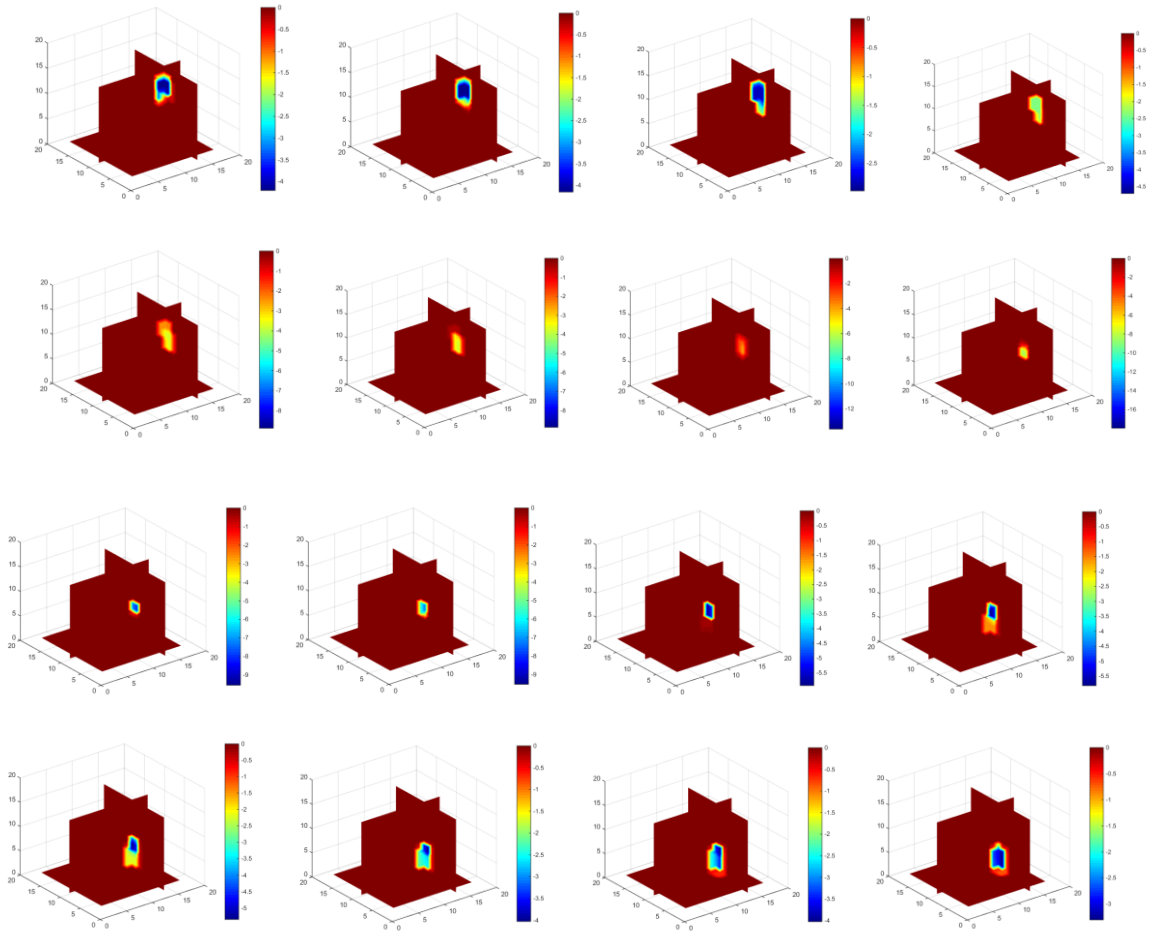

Figure 5.11. Image reconstruction of 3D simulation using Temporal TV

In Figure 5.12, the output vectors of 27 voxels from 71 frames are plotted, which illustrates the moving process of the object within the simulated phantom. From the plot of $vox1_8$, $vox2_8$, and $vox3_8$, it could be seen that the characteristic value is fluctuating, which could be understood as the process that how the inclusion was entering and leaving the specific voxels. The plots of signals from other voxels are a parallel line and the value remains at 0, which indicate the sample did not go through them and it is consistent with the setting up of the simulation test. For cross-correlation of a 3D case, the distance in function (5.5) is a known constant and determined by the size of the height as we defined the sensitivity map (figure 5.1 and 5.10). Considering that the object is moving from $vox1_8$ to $vox3_8$, the experienced time length could be calculated from the peak value of cross-correlation plot

between this two voxels since the object is moving downwards from $vox1_8$ to $vox3_8$. Hence, the speed calculation would be achievable. Figure 5.13 is showing the result of the cross-correlation.

This 3D simulation test discussed the performance of sample movement monitoring via 3D image reconstruction of the simulated dynamic movement of the sphere. Speed calculation using the proposed method is also feasible. It is certified that temporal TV could meet the requirement of being discussed in this section. In the next part, some results from real data will be shown, and the calculated result of speed will be illustrated and analyzed in section 5.4.

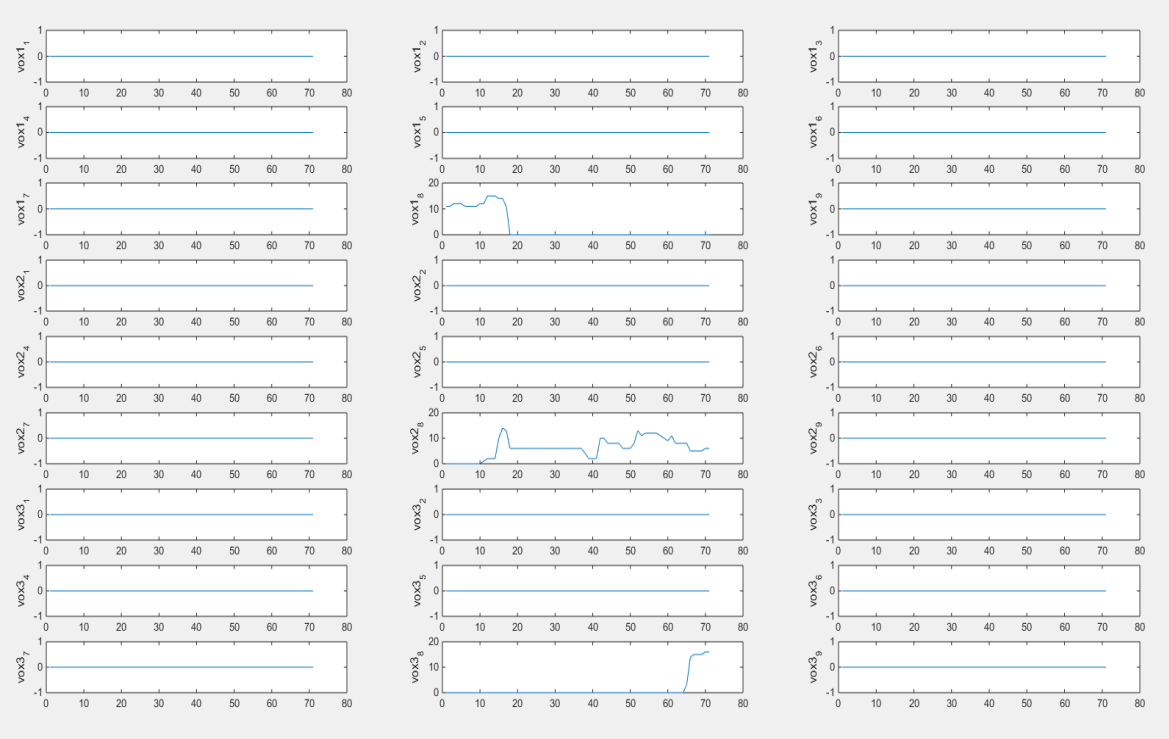

Figure 5.12. Plots of 27 voxels with thresholding data

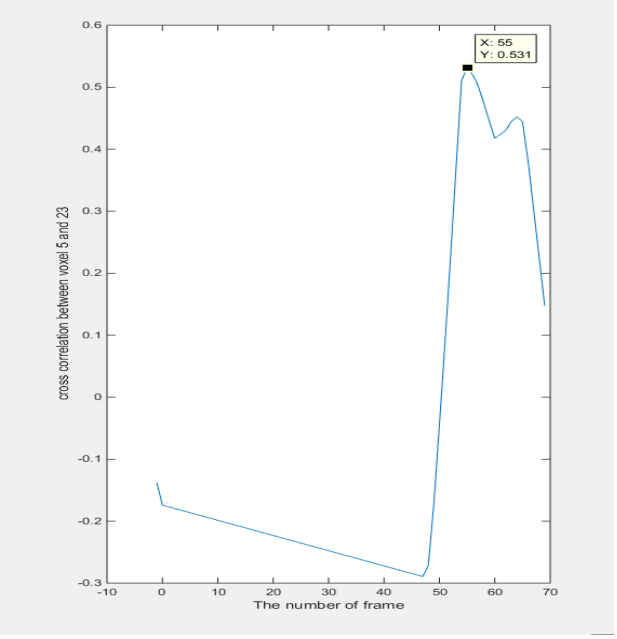

Figure 5.13. Plots of cross correlation between voxel 8 and 26

5.3.4. Experiment in 3D

The phantom used for the 3D experimental test is designed as a 16-electrode cylinder container with a height of 25 cm and a diameter of 14 cm and using the same material with all components as the 2D one. Two rings of 8 electrodes (3 cm x 4 cm rectangular-shaped) are fixed on the wall of the sensor at a height of 9 cm and 16 cm respectively, which is consistent with the situation of the simulation test. A small plastic bottle filled with sands was used to stand for dispersed phase and tap water was poured into the phantom as a continuous phase. To make a relative movement, the bottle was controlled to move up and down continuously using string that connected with the bottle. As shown in the pictures, the bottle was released down and pulled up vertically (starting from the water surface). During the movement, it was on the left-hand side and close to the inner wall of the sensor. The data collection system and method are identical as mentioned before, and the driving frequency was set to be 10 KHz. Figure 5.14 shows the 3D experimental phantom and inclusion.

Figure 5.14. Sensor and tested sample of 3D experiments. (a) Phantom of the 3D experimental test: 16 electrodes composed with 2 rings of 8 are utilized for excitation and measurement. The stainless-steel boards are applied to the tank as the main part for the pipe to sit on, which avoid the problem of leaking. (b) Non-conducting inclusion of 3D experiment test: a plastic bottle filled with sands to make sure the inclusion could sink down to the bottle, where tap water was chose as the background and continuous phase.

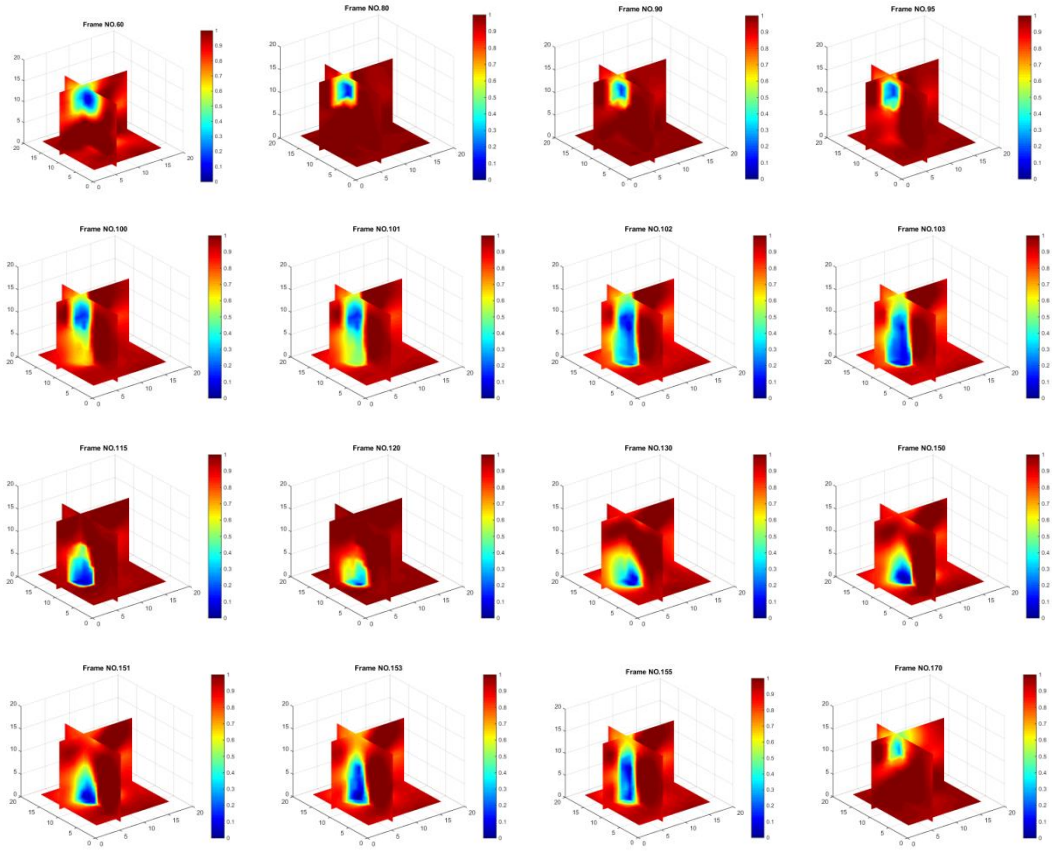

Figure 5.15. Reconstructions of the movement using temporal TV

During the experiment, there were periods of the bottle movement conducted, and 200 frames were collected. The pictures shown in figure 5.15 illustrate the whole movement process. Comparing with the reconstructed images of the simulation test, it seems that the experimental test got a slightly degraded result. However, during the simulation, a certain location of the object corresponds to the calculated boundary voltage data, which contribute to a frame of the image. For the 3D reconstruction of the experiment, the real boundary data is measured by the data collection system, and coming from the dynamic movement of the bottle. It is worth to emphasize that the time of measuring data of each frame could not be neglected, whereas simulation did. During this time interval, the bottle was still kept moving, which lead to inter-frame data produced.

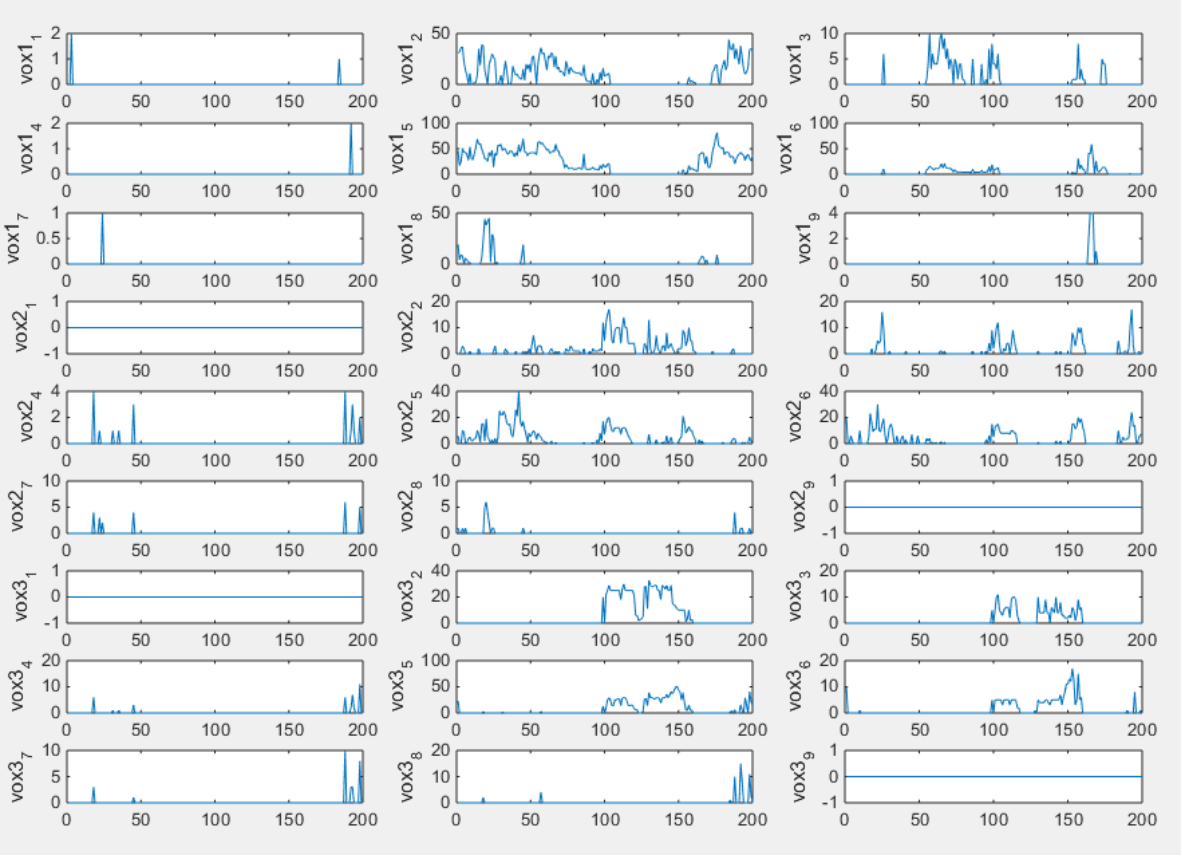

Figure 5.16. Plots of voxels after image thresholding

The plots of voxels are displayed in figure 5.16, which demonstrate how the movement of the inclusion affects individual voxels. The output signal from 27 voxels are plotted here based on thresholded dynamical experimental reconstructed images. The vertical dynamical movement of the target is monitored and reflected via extracted values. The horizontal lines mean the target does not come to the specific voxel during the whole process, otherwise, it suggests how the target emerges and disappears. The first few frames could be ignored as the bottle have not started to move, and it is actually the background data are plotted and would not affect the result of the velocity profile. Since the real data of the 3D experiment contains more unexpected noise, the results shown in Figure 5.15 are not as good as the 2D case. To eliminate the unwanted factors, as what was doing in the 3D simulation that thresholding was conducted.

The voxels used for cross-correlation calculation in Figure 5.17 are from top voxels layer and bottom voxels layer which corresponds to the case that the object was moving through this space. The peak value of the function indicates the moment that two signals have maximum similarity, which gives the transit time of the object moving from the top to the bottom. For the case from Figure 5.17, the transit time corresponds to 86 frames. The average movement speed could be calculated with the know data collecting speed of the system and the distance that defined as a sensitive matrix. The result will be shown and analyzed in the next section.

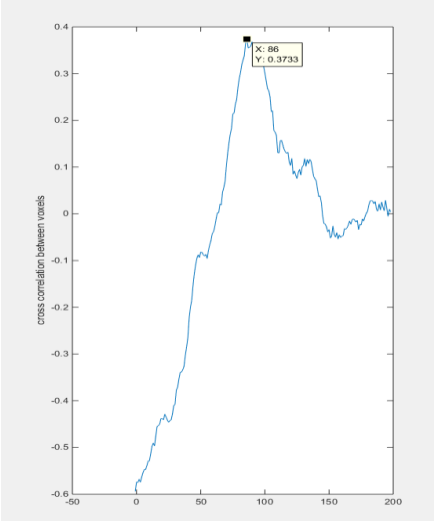

Figure 5.17. The results of cross-correlation: x-axis indicates the frame number, and the y-axis gives the value of cross-correlation result. The peak value on the x-axis in this case suggests the transit time of this movement.

5.4 Discussion

In this section, all of the results of both 2D and 3D experimental tests, including reconstructed images and results of velocity are concluded. The quality of the images are discussed and the cross-correlated results using proposed spatiotemporal TV algorithms are presented, where relative error of the speed is calculated, and further analysis is carried out. Table 5.2 shows the results of speed. The cross-correlated average angular speed is given by **360** °/ **(Transit time×System speed)**. The speed in this section is angular speed due to the circular movement of the plastic bar, where the measured time of the whole process was given by a timer, which is 10.8s and stands for the length of time that the inclusion move through the whole circle (360 degrees), and the real average angular speed could then be calculated with **360 degrees/ (Measured time×System speed).**

Table 5.2. Calculated results of the 2D experiment

Measured time (s)	**System speed (s/frame)**	**Transit time from cross-correlation (s)**	**Angle (°)**	**Measured speed (°/s)**	**Cross-correlated speed (°/s)**	**Relative error (%)**
10.80	0.21	10.71	360	33.33	34.29	0.8%

In the 3D experiment, the distance used for calculations was the distance between the top voxel layer and the bottom voxel layer, which is defined as 13cm. It was calculated that the transit time was 17.85s from the number of frames given by the peak of the cross-correlation plot. The cross-correlated speed and real speed are given by 0.76 and 0.73 respectively, which gives a 4% relative error.

Table 5.3. Calculated results of the 3D experiment

Measured time (s)	System speed (s/frame)	Transit time from cross correlation (s)	Distance (cm)	Measured speed (cm/s)	Cross correlated speed (cm/s)	Relative error (%)
33.07	0.21	17.85	13.00	0.76	0.73	4 %

The images of 2D and 3D has been shown in previous section. It worth of notice that the reconstruction results from simulation and experiment are different. It needs to be pointed out that the dynamic model is more complicated than a static one as the sample is actually kept moving at any moment, which would affect the data measurement. In the simulation part of both, it was assumed that the boundary data is corresponding to a specific location of the sample although what has been simulated is a dynamic model. However, for a real dynamic situation, the location of the sample is kept changing while that frame of data was being measured, which lead to the circumstance that the data are overlapping.

In terms of the image reconstruction quality, the proposed algorithm has a good performance in the 2D test. By contrast, the object of experimental images got slightly overlapping than ones from simulation, which could also be from the reason stated above. In the 3D simulation and experiment test, the sample movement could be monitored properly although the ones in the middle area seem relatively weaker than the ones close to rings. Images produced in the experiment are still acceptable although inter-frame data are introduced.

In conclusion, the method of flow measurement using ERT with the proposed algorithm is validated with 2D simulation and experimental test. For the case using 3D ERT, even if the reconstructed images are not as good as the 2D case and suffering from the problem of inter-frame data, however, a low-speed data collection ERT system was used and result from simulation study still shows a good performance. The speed measurement result of experimental test is controlled below 4%, which is still acceptable and proved that the speed measurement using the technique of 2D and 3D ERT with spatiotemporal TV algorithm combined and cross-correlation is achievable, and the result could potentially be upgraded with a fast ERT data collection system. The accuracy of cross-correlated result is actually determined by images. The quality of the reconstructed image would be quite important and must be upgraded, which is always a challenging topic to study. In further work, in terms of the proposed algorithm, a more effective method of parameter selection could be further researched in order to reconstruct images in a more time-efficient way. To eliminate the negative effect of inter-frame data, the time interval of collecting boundary data should be shortened, in this case, data collection system would be required to be fast enough.

5.5 Conclusions

Velocity profile measurement using high-speed two-channel 2D ERT and cross-correlation between two separate rings has been investigated for a few decades due to its fast development in the industrial field. Since the flow is a three-dimensional concept, using 2D ERT to obtain consecutive cross-sectional slices may ignore some occurrences in the flow pipe. In this case, it is desirable to combine the measurement method with a 3D reconstruction technique since a single multi-plane ERT can provide 3D flow velocity information with dual-plane electrodes. With a series of phantom experiments conducted, the measurement method based on 2D ERT was tested and validated, and the speed measurement method based on 3D ERT using spatiotemporal TV algorithm combined with voxel-voxel cross-correlation method is proposed. The reconstructed images showed the

feasibility of the speed measurement of a dynamic sample in 2D and 3D. The process reconstruction of 2D shows great performance with the proposed algorithm. A slightly degraded result in the 3D experiment has shown, and the reasons, as stated in the discussion chapter, could be from both insufficient time resolution and the inter-frame data generation. Produced noise in experiments can also be an influence factor to degrade the image quality. In this chapter, all the experiments were conducted by using an experimental tank with manually moved inclusion instead of real two-phase flow, the test is done in semi-dynamical setting, making it much more robust compared to fully static tests making presented results very useful method for flow measurement and interior flow system monitoring.

Chapter 6 ERT image reconstruction using Planar Array

ERT imaging modality has great potential for industrial applications with the advantages of being a high temporal resolution. It is especially useful in cases, such as, geophysical detection, landmine detection and detections on non-transparent region, where measurement data is only available from a single surface, for data acquisition. Instead of the circular ERT model that uses the traditional circular electrode model, in this work, Subsurface (also called Planar Array in this chapter) ERT is implemented, aiming to zvisualize a pipeline transporting a two-phase flow. The planar array can explore spatial information within its detectable region by producing 3D images, which have a higher spatial resolution in axis-direction than a traditional ERT with a dual-plane electrode sensor. However, in solving the inverse problem of a 3D subsurface ERT using a planar array the images may be degraded, especially in cases where the location of the target is relatively deep. The total variation (TV) algorithm as an L1-norm regularisation method has the potential to improve the image quality, and some works have shown that TV reconstructs sharper images, which provides an advantage when representing spatial information. In this chapter, the performance of subsurface ERT using the TV algorithm for 3D visualization are presented based on simulations and experiments, and the results of quantitative measurement of depth are discussed.

6.1 Introduction

ERT is capable of visualizing tested samples by solving conductivity distribution based on forward modelling and solving inverse problem. The solution of forward problem is achieved by combining FEM with complete electrode model, and EIDORS is a useful tool in the forward modelling of ERT. Various algorithms have been invented for image reconstruction to solve inverse problem, where regularization is involved to overcome the trouble brought by the ill-posed nature of ERT inverse problem. Of these algorithms Tikhonov is one of the most traditional and popular. However, the introduction of ‘smoothness’ may lead to blurring and result in the degradation of reconstructed images. Studies have shown that

total variation can make inroads into preserving the sharpness of the boundary by using the $l1 - norm$ regularisation function.

ERT sensors have a few different types, depending on the way of accessing data, and the availability of where data could be measured. Circular ERT is commonly applied to relatively flexible situations where most sides of the region of interest are accessible, for example, an electrode ring could be installed on the wall of the entire pipeline for monitoring purposes. However, some cases would have limitations and inconveniences in data collection, where only a single side would be available for measurement, for instance, some inclusions buried in the ground or inside the water that only the surface would be available for data acquisition. The circular electrode model would not be suitable for any such circumstance, and a planar array installed on a subsurface ERT sensor would potentially be helpful for visualizing the target. Subsurface ERT is similar to a 'scanner' for 3D visualization and can be useful in various applications, however, it would suffer from additional challenges, especially in cases where samples are placed very deep. Current density and the strength of electric fields would decay with the distance from the subsurface electrode-plane, and extra difficulties are imposing if inclusion leaving far from the planar array. However, compared with the planar array and dual-plane sensor for ERT visualization of a pipeline, a conventional circular electrode-plane could represent the spatial information of the whole medium of interest, but would suffer from a very low resolution along axis-directions because of the limited number of rings. Although multiple electrode-plane sensors have shown improvements in spatial resolution, it would also place a high demand on the data acquisition system since many more electrodes will be involved. The planar array can provide assistance in exploring information of the region with less depth. Although the center area might be difficult to detect (but also depending on the size of the pipeline and planar array), it still capable of generating 3D images with higher resolution on axis-direction in its detectable region, which supplements the traditional ERT model using electrode rings around the pipeline. In this case, a planar array could potentially be combined with a traditional ring model to produce more useful information.

Subsurface ERT has been studied mostly in clinical applications. In 2000, J.L. Mueller presented their work, in which a rectangular electrode array based on EIT was applied to the human chest for 3D reconstruction during ventilation and perfusion, suggesting the

potential for collecting information about blood volume variations in the chest [133]. Following on from that, other clinical applications have also been shown in the last decade, such as in, prostate disease [134], and cervical neoplasia [135]. More recently, H. Perez presented a method for 3D image reconstruction using a novel electrode configuration in the context of breast cancer, where electrodes of current injection and voltage measurement work separately [136] .ERT using planar array is actually different with the conventional ones with electrode bounded the whole region of interest if the domain of interest is infinite (such as ground), and such approach can also term open domain EIT since all electrodes are placed on one side, which introduces more challenges on image reconstruction. To overcome such an effect, most research approximates it to be an enclosed domain, but this brings error, and a recent study proposed to transform the original open domain into an enclosed 2D circular domain based on Riemann mapping [137].

For monitoring purpose, reconstructing high-quality images is always the target. Previous works suggest that TV has the capability to produce sharp-edged images and preserve the discontinuities between the background medium and the target and is especially suitable for big contrasts. The TV regularisation method was firstly proposed by L.I. Rudin and S. Osher in 1992 as a denoising algorithm [77]. In comparison, the conventional least-square method uses the L2-norm yields linear solutions and can be computed with an algebraic framework, whilst TV employing L1-norm is nonlinear and computationally complicated, however, research shows that TV functions makes contributions to edge preserving, and becomes an appropriate method for noise removal and deals with image restoration. TV regularisation has received much attention, especially in electrical tomography in recent years.

In this work, we are aiming to explore the flow visualization approach using a planar array with the ERT approach, in addition, numerical measurements of target depths based on reconstructed images are studied. Split Bregman TV regularisation has been chosen for visualization to test the performance of subsurface ERT, and both simulation and experiments are included in this work. Simulation is implemented by modelling a phantom with a 4×4 electrode planar array on the top surface to demonstrate the feasibility of the approach, and the experimental sensor was designed, keeping it consistent with the simulated model, in which a series of experiments are validated. Moreover, position error

and volume fraction are applied for assessing the image quality, and suggested parameter selection method. Furthermore, results based on selected parameters using real data are displayed, and spatial gradients along the depth were generated for working out the depths that reflected visualized images. The accuracy of the depth detection of the samples is shown at the end.

6.2 Method

The following sections are aimed at exploring the performance of ERT visualization based on a planar array, where simulated data and experiments are both conducted for a series of analyses. In section 6.2, the measurement strategy is described, and the parameter selection of the SBTV procedure is suggested. Some quantitative indices are defined for further numerical analysis.

6.2.1 Data acquisition

Among various current excitation and voltage measuring strategies, the traditional neighboring method has been used for data collection. Instead of the ring-electrode model that has been discussed in the previous chapter, electrodes are numbered No.1-No.16. Then the procedure of excitation and data collection would be the same as explained in Chapter 1. The diagrams below show the detailed steps, where the first two excitations are represented with numbered electrodes for illustration, and 16 current excitations are be conducted.

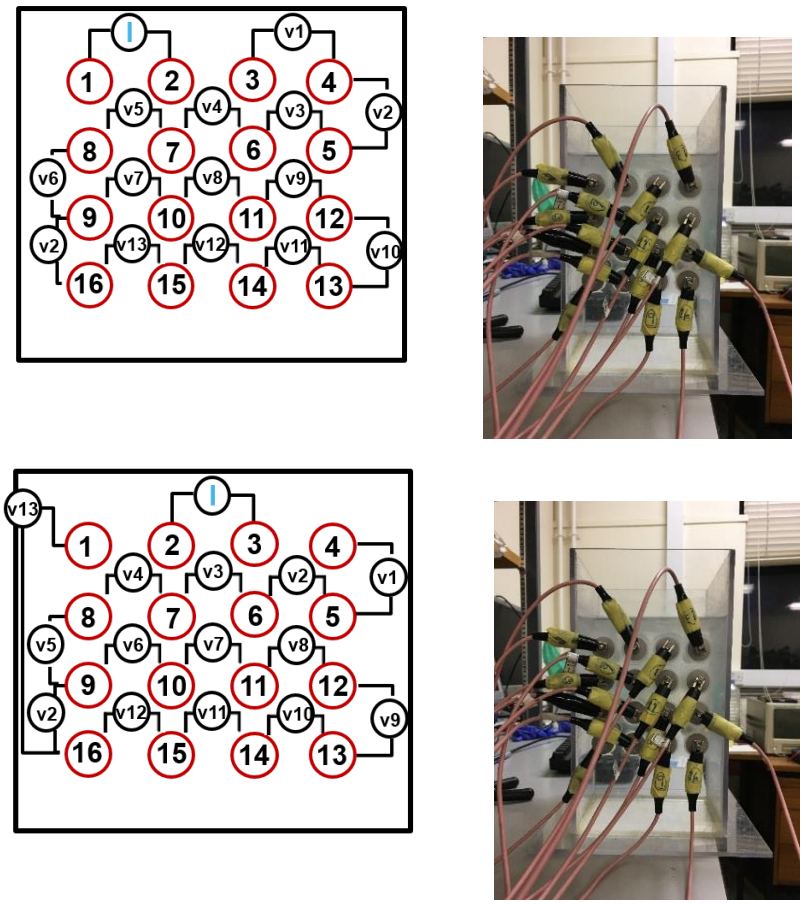

Figure 6.1: Illustration diagram of data measurement procedure.

6.2.2 Image-based depth detection

The depth of the target is detectable based on the 3D reconstructed image of ERT. There are two different depths defined. The distance between the CoG of the target and planar array is labelled D_c, and the distance D_t measures the distance from the top surface of the target to the planar array. Calculation of D_c is given by working out the CoG of target based on visualization. The distance D_t is measured with an average distance since the 3D image produced by ERT would not be perfect, so it is more accurate to discover the depth D_t of the target from different points from the top boundary os the 3D image. Note that the 3D images are composed with voxels of $21 \times 21 \times 21$, so the distance can be detected by searching downward from a voxel on the top slice through voxels of 1×21. In this chapter, a 2D slice is extracted from the center, and 3 lines of voxels in the center are taken out for calculations of average distance, where

$$D_t = \frac{1}{3}(D_1 + D_2 + D_3) \tag{6.1}$$

6.2.3 Numerical analysis

In some literature, the void fraction would commonly be utilized for analysis of the reconstructed result. In the two-phase, the void fraction is defined as the ratio between the disperse phase and continuous phase as stated in Chapter 3. In terms of the static experiments that have been discussed in this section, a similar definition is given, where the fraction of the 3D object (Volume fraction) is defined as the effective volume ratio between the inclusion and the 3D phantom. To evaluate the results that are generated using a planar array based on the SBTV algorithm, the error of volume is taken into account for the numerical analysis. The true volume of the target is 15.625 cm^3, and the calculation of the volume of the tested sample is given by the thresholding images. The numerical analysis of volume fraction uses the average relative error of volume (REV):

$$\mathrm{REV} = \mathrm{ave}\left(\frac{|V_{IMAGE} - V_{true}|}{V_{true}} \times 100\%\right) \tag{6.2}$$

In many industrial or geophysical applications, the detection aimed at an unknown object in a region of interest is very important, where knowledge of the depth of the detected object can potentially be suggested by reconstructed images from Subsurface ERT using a Planar Array sensor. Therefore, numerical analysis of position error aimed at depth detection is critical. Paying attention to the detected depth of the target, the calculation of the Centre of Mass of an image can reflect the depth D_C, and the residual error is given by the numerical difference of the depth from the reconstructed image and the actual depth. The numerical analysis of the performance of depth detection with subsurface ERT employed average relative error (RED):

$$\mathrm{RED} = \mathrm{ave}\left(\frac{|D_{IMAGE} - D_{true}|}{D_{true}} \times 100\%\right) \tag{6.3}$$

6.2.4 Parameter selection

Although some studies have shown that the SBTV algorithm contributes to improving the image quality, different combinations of parameters can largely affect the result of either visualization or measurements reflected from reconstructed 3D images. Such situations also create a fluctuating residual error which leads to uncertainty if optimal parameters cannot be discovered. In addition, the number of parameters, as in the case of SBTV algorithm with three parameters, also brings more difficulties as so many combinations of parameters make it too hard to make choices. In such situations, the numerical analysis would be helpful for making the selections of parameters. In the SBTV algorithm that has been used in this chapter, three parameters, $\mathrm{mu}, \mathrm{lambda}\ \mathrm{and}\ \mathrm{gamma}$, are involved in the iterative calculations (See equation 2.77-2.81 in section 2.5.2). If optimal parameter selection can be made using a training procedure, and those selected optimal parameters are brought for further testing, it would be helpful for effectively solving the inverse problem. The main idea of parameter selection is choosing those close to the ideal solution, and a range of relative error is set up for discovering qualified solutions among lots of parameter combinations. For detection purposes using an ERT planar array, the numerical depth and size of the reconstructed object were paid close attention. The true depth and volume are calculated as the expected 'ideal' solution. There were 3375 combinations of parameters produced for 'training', where each set of parameters has a corresponding image. The depth and volume can quantitatively be determined from reconstructed 3D images, which give a residual error between the solution and the true measurement. If their corresponding error is located within the defined range they are considered as optimal parameters. The parameter selection process requires the following scheme:

1. Choose the range of each parameter:

$$\mathrm{mu1} = \mathrm{logspace}(\mathrm{a1}, \mathrm{b1}, \mathrm{n1})$$
$$\mathrm{lambda1} = \mathrm{logspace}(\mathrm{a2}, \mathrm{b2}, \mathrm{n2})$$
$$\mathrm{gamma1} = \mathrm{logspace}(\mathrm{a3}, \mathrm{b3}, \mathrm{n3})$$

2. Input each combination of parameters and save all corresponding images and parameters.

```
for ii=1:n1
            mu=mu1(ii);
    for jj=1:n2
            lambda=lambda1(jj);
        for kk=1:n3
            gamma   =gamma1(kk);

        image=SBTV(mu, lambda, gamma, Data)
        number=number+1;
        save_parameter(1,num)=num;
        save_parameter(2,num)=mu;
        save_parameter(3,num)=lambda;
            save_parameter(4,num)=gamma;
        save_image{num}=image;

        end
    end
end
```

3. Calculating the true depth and volume, and defining a range of acceptable error.
4. Parameters are selected based on a residual error of depth/volume.

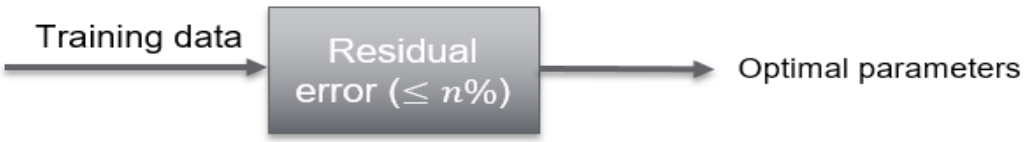

Figure 6.2: illustration of parameter selection process

In the following parts, results based on this parameter selection scheme are displayed and make discussion, where errors over 10% are filtered out.

6.3 Simulation tests

The 3D modelling of ERT using Planar Array has been simulated based on EIDORS. The phantom was designed as a cubic tank with a 16 (4×4) circular electrode-plane placed single sided. The background medium has been given a conductivity of 1, while a sphere with various locations and depth as an inclusion with a conductivity of 10. Excitation current was set at 0.1 mA, and the current pattern has been chosen as a neighboring excitation and measurement method. Figure (6.3) displayed below shows the forward modelling of such a planar array, and the specifications of sizes of different components of the model are illustrated in Table (6.1). In the 3D coordinate system, the subsurface ERT model is defined within the range of $-7cm < x < 7cm, -12.5\ cm < y < 12.5\ cm, -14\ cm < z < 0,$ with the geometrical centre of the electrode-plane being located at the origin of coordinates$(0, 0, 0)$. The coordinates of all electrodes are specified in Table (6.2), and the Sensitivity map of the Planar Array is drawn by Mayavi as shown in Figure (6.4). In this section, different locations with varying depths of the sample are set-up for the simulation test, and reconstructed images are displayed in Tables (6.3)-(6.5).

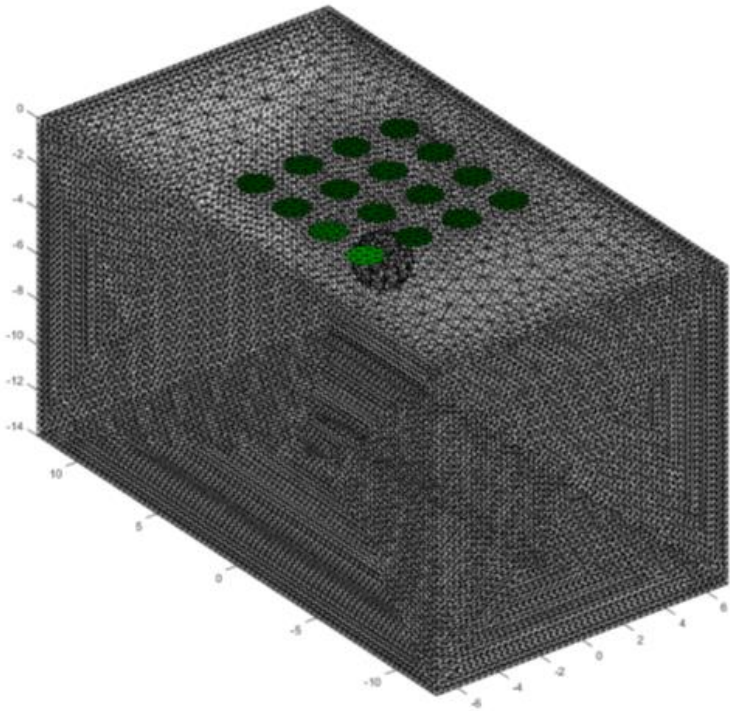

Figure 6.3: Forward modeling of planar array using EIDORS

Table 6.1: Specifications of simulation phantom of Planar Array

Items	**Size**
Number of electrodes	16
Length	25cm
Width	14cm
Depth	14cm
Diameter of circular electrodes	0.85cm

Table 6.2: Locations of each electrode. The electrode number in this table is keeping consistence with how it was numbered in forward modeling, and coordination of 16 electrodes has been given for illustration.

Electrode 1	**Electrode 2**	**Electrode 3**	**Electrode 4**
(-4.1 , 4.1)	(-1.3 , 4.1)	(1.3 , 4.1)	(4.1 , 4.1)
Electrode 8	**Electrode 7**	**Electrode 6**	**Electrode 5**
(-4.1 , 1.3)	(-1.3 , 1.3)	(1.3 , 1.3)	(4.1 , 1.3)
Electrode 9	**Electrode 10**	**Electrode 11**	**Electrode 12**
(-4.1 , -1.3)	(-1.3 , -1.3)	(1.3 , -1.3)	(4.1 , -1.3)
Electrode 16	**Electrode 15**	**Electrode 14**	**Electrode 13**
(-4.1 , -4.1)	(-1.3 , -4.1)	(1.3 , -4.1)	(4.1 , -4.1)

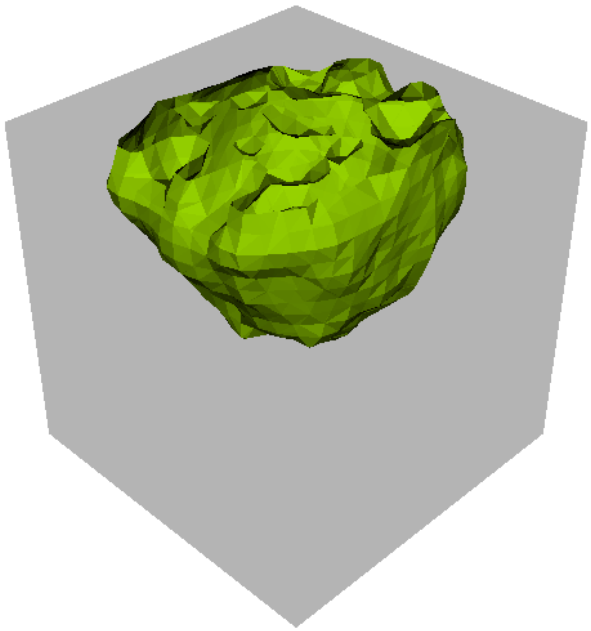

Figure 6.4: Sensitivity mapping of Planar Array drawing by Mayavi

Table 6.3: Results of image reconstruction in simulation test by placing the sample in the center of the electrode-plane with a depth of 2cm, 3cm and 4cm.

	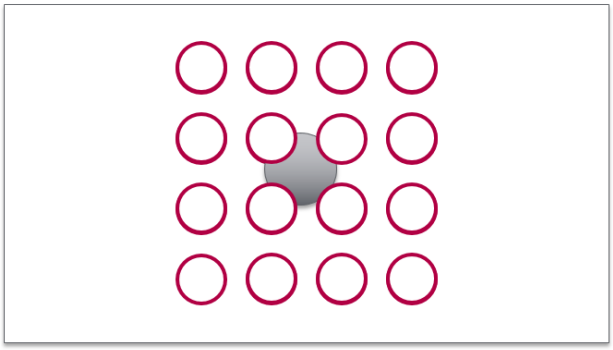	
Depth	**True image from simulation**	**Reconstructions**

2cm	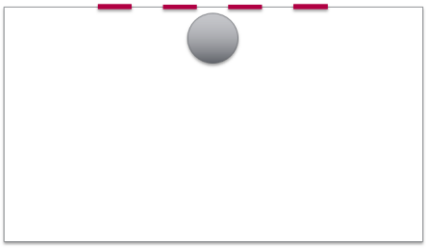	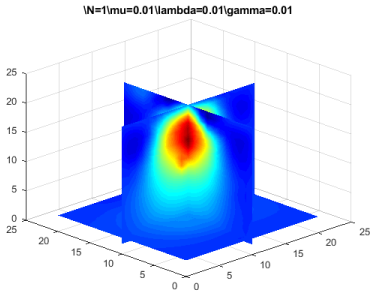 \N=1\mu=0.01\lambda=0.01\gamma=0.01
3cm	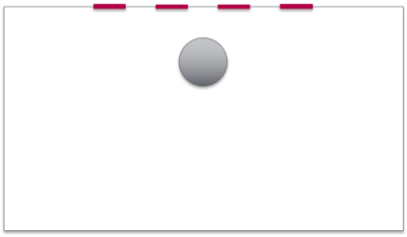	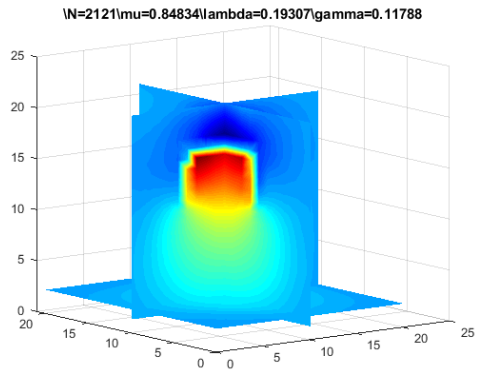 \N=2121\mu=0.84834\lambda=0.19307\gamma=0.11788
4cm	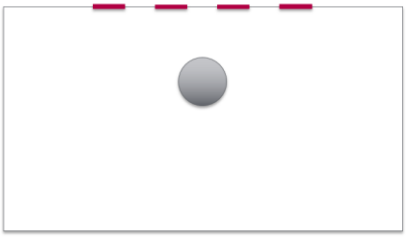	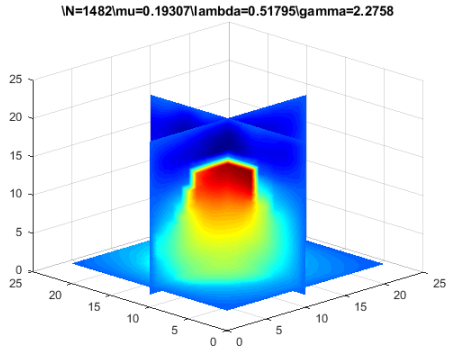 \N=1482\mu=0.19307\lambda=0.51795\gamma=2.2758
	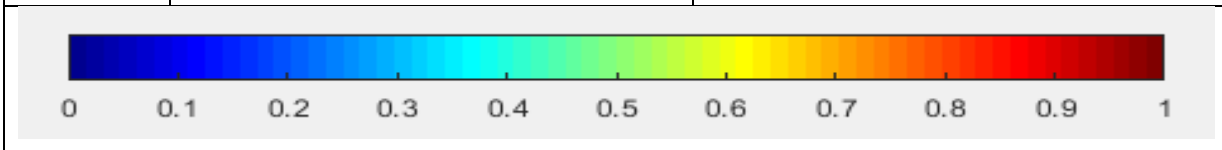 0 0.1 0.2 0.3 0.4 0.5 0.6 0.7 0.8 0.9 1	

Table 6.4: Results of image reconstruction of simulation test by placing the sample near the out boundary of the electrode-plane with a depth of 2cm, 3cm and 4cm.

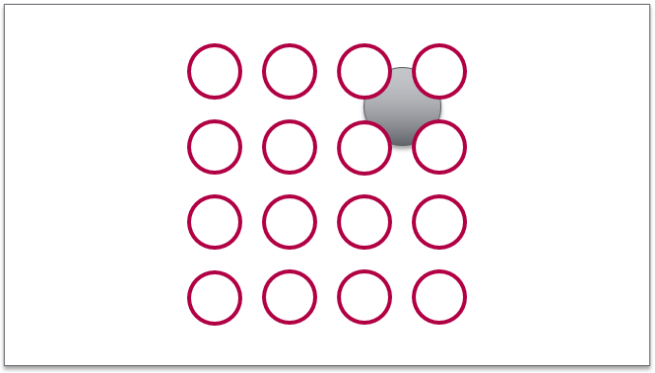

Depth	True image from simulation	Reconstructions
2cm	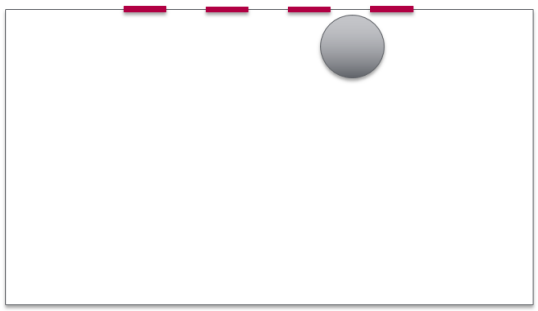	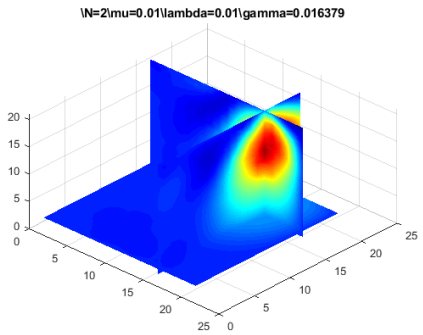
3cm	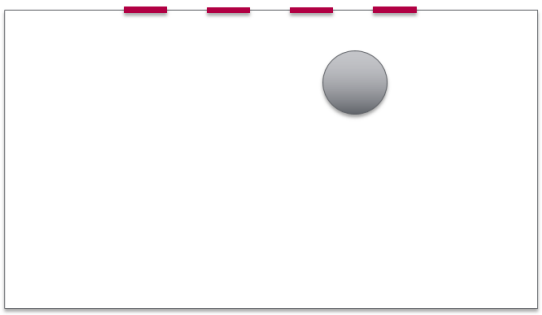	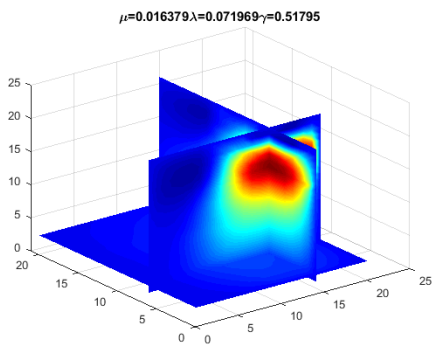
4cm	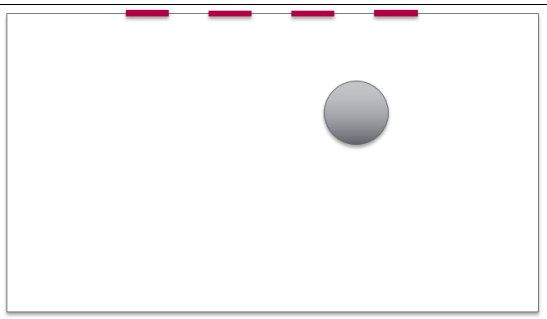	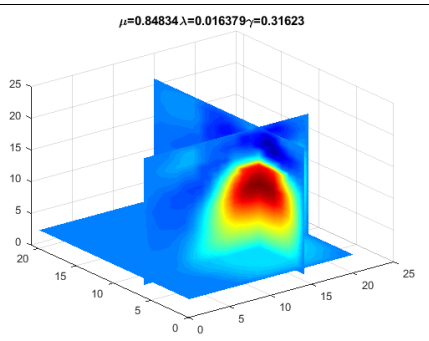

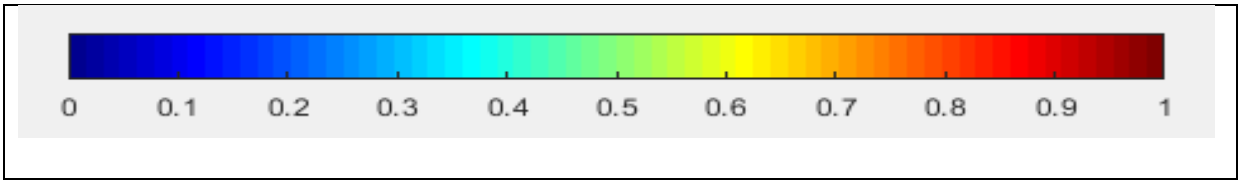

Table 6.5: Results of image reconstruction of simulation test by placing the sample near the out boundary of the electrode-plane with a depth of 2cm, 3cm and 4cm.

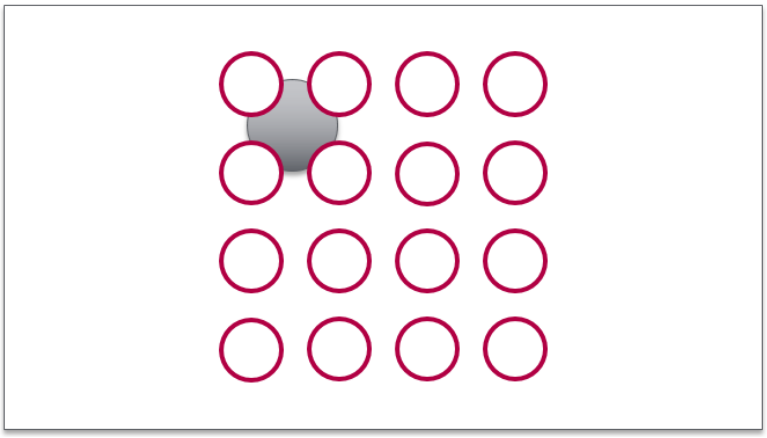

Depth	True image from simulation	Reconstructions
2cm	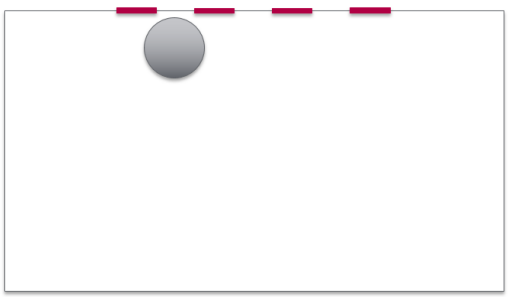	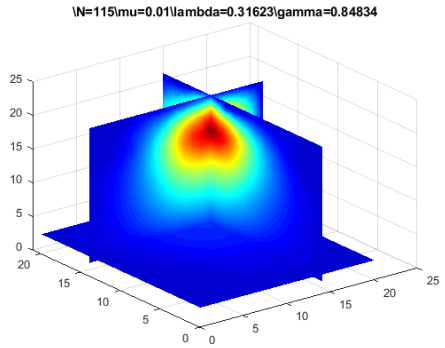
3cm	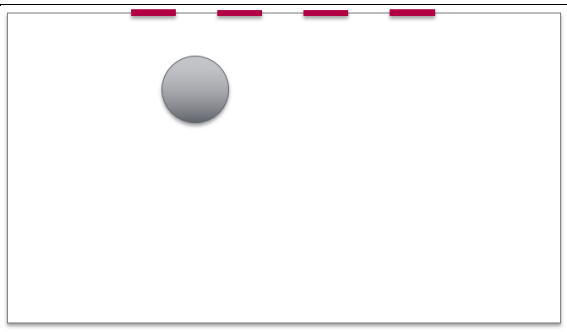	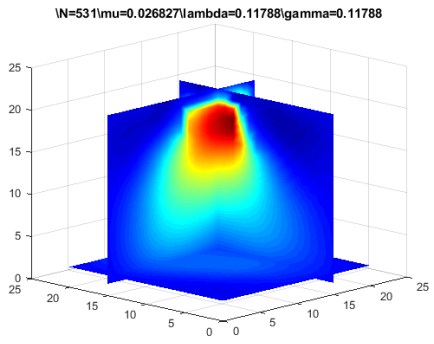

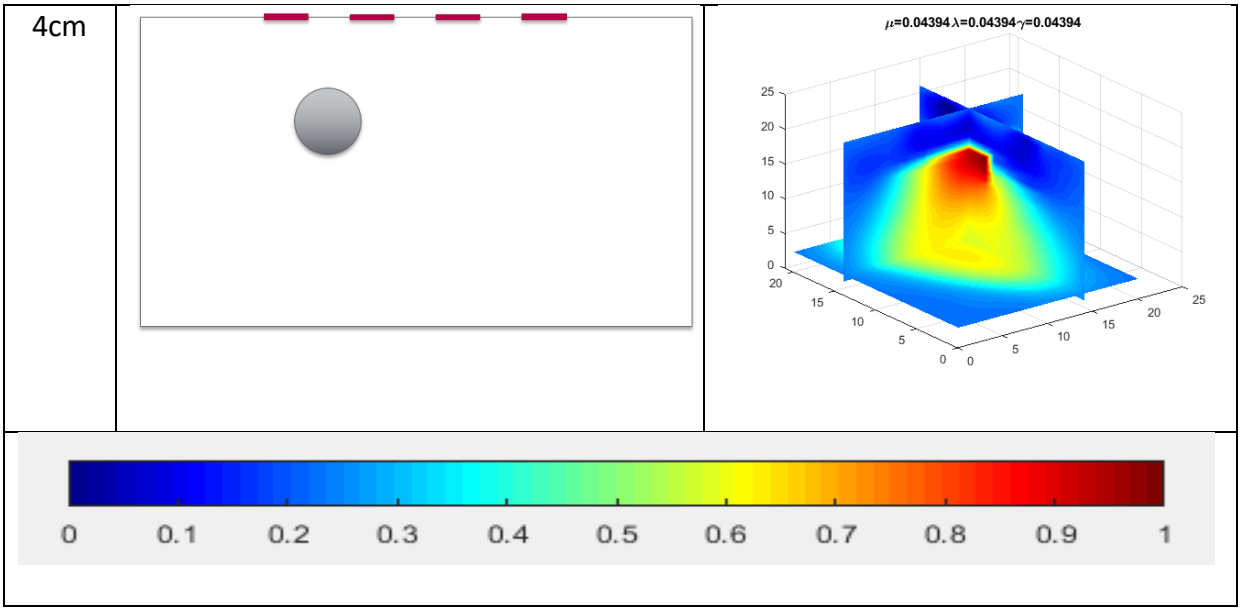

Depths of 2cm, 3cm, and 4cm have been chosen as distances between the center of the target and the planar array to make detections based on the shape of the sensitivity map. The simulated sample was placed at different positions with 3 different depths. In tables (6.3) and (6.5), the visualization results are displayed with corresponding true images placed on the left-hand side. According to the results shown in the tables above, visualizations produced using a planar array show consistence in various locations. At different depths of each location, the reconstructed 3D objects are showing agreement on tendency, with changes in the distance between the object's top surface and electrode-plane being recognized.

Since images are reconstructed from targets that are placed at different positions and depths, the numerical depths explored should be feasible based on visualized results using the TV algorithms with optimal parameters. If the depth is measured from the planar array to the center of the object, the Centre of Mass (CoM) of the recovered 3D object can be calculated based on the thresholding image. Results of the depth measurement based on visualization are shown below:

Table 6.6: Detected depth of different locations from simulation tests.

Locations\True Depth	2cm	3cm	4cm
Center	2.0328cm	3.0167cm	4.032cm
Left	2.078cm	3.037cm	4.11cm
Right	1.922cm	3.03cm	3.78cm

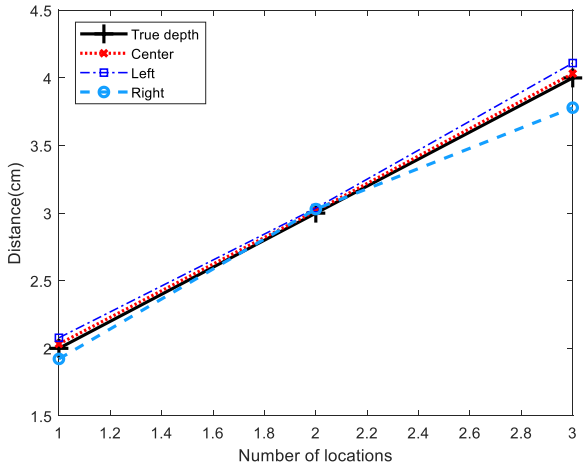

Figure 6.5: Plots of the reflected distance of the target from images based on simulation

In terms of the image quality before quantitative analysis, all images are showing a sharp edge on the top surface, and the other side is very smooth. Degraded 3D images are observed since the volume gets bigger as the distance moves further down. Numerical calculations of distance detected by ERT planar array based on simulation data are represented, and Figure (6.5) brings them together as line graphs to make a comparison. The black line indicates the true distance, and others are given by the quantitative results that are suggested from positions shown in Table (6.6). Regarding these numerical distances, results from all positions are showing a better performance with 2cm and 3cm, while it starts to degrade at the depth of 4cm. Comparing the different positions, the one at the center of the planar array gives a slightly better result as the calculated distance is closer to the true distance, with the others showing a little further deviation. In general, the simulation results display a successful visualization as well as providing the quantitative

measurement result of depth detection, which suggests that it would be feasible to explore information based on ERT using a planar array. In the next section, experiments using a phantom are engaged to validate this idea.

6.4 Experimental validation and results

Conductivity mapping across the region of interest would theoretically be re-distributed if the inclusion changed the locations or depth, therefore Subsurface ERT could potentially be applied to detecting or monitoring an invisible and unknown sample underneath a surface with real data. The previous section has shown reconstructed images with the sample at different depths and locations using simulation data, and compared detected distance based on visualization, which quantitatively showed agreement with the true distance, hence demonstrating the feasibility of sample detection using subsurface ERT. In this section, experimental validation has been engaged based on real experimental data collected from a designed Planar Array sensor. The main body of the designed physical planar array sensor for experiments is made from a transparent cubic tank with the electrode plane on the front surface, enabling it to contact the medium inside the tank. As shown in the photo of Figure (6.6), the size of the tank is $14\ \mathrm{cm(length)} \times 14\ \mathrm{cm(width)} \times 25\mathrm{cm(height)}$, and the 4×4 electrode-plane is fixed with a diameter of 0.85cm for all the circular electrodes. The EIT Swisstom Pioneer system has been utilized for data collection, where a current with an amplitude of 1mA and frequency of 195 KHz has been chosen as the excitation source. The experimental sensor was designed to be consistent with the simulation model. A metal cube with a size of $2.5\ \mathrm{cm} \times 2.5\ \mathrm{cm} \times 2.5\ \mathrm{cm}$ was chosen as a testing sample in a series of experimental tests, and tap water filled the tank as a background conductive liquid. Background measurement data using a planar array sensor is compared with simulation data, and Figure 6.7 shows consistent agreement.

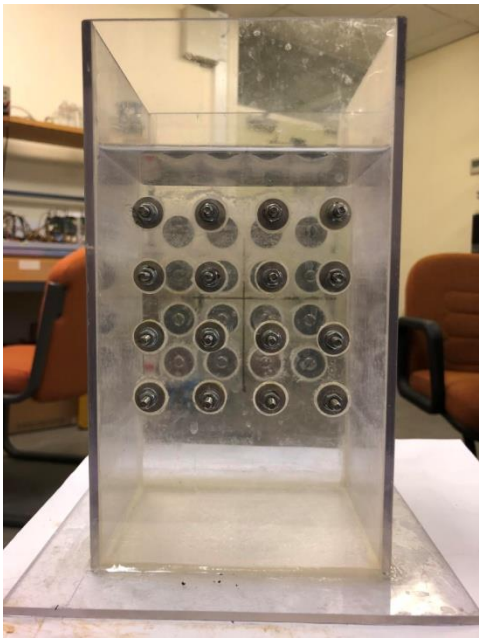

Figure 6.6: Planar Array experimental sensor for 3D image reconstruction: this sensor is designed for different works, in this study, electrodes placed on the single side are used for experiments, and the second array did not involve in this work.

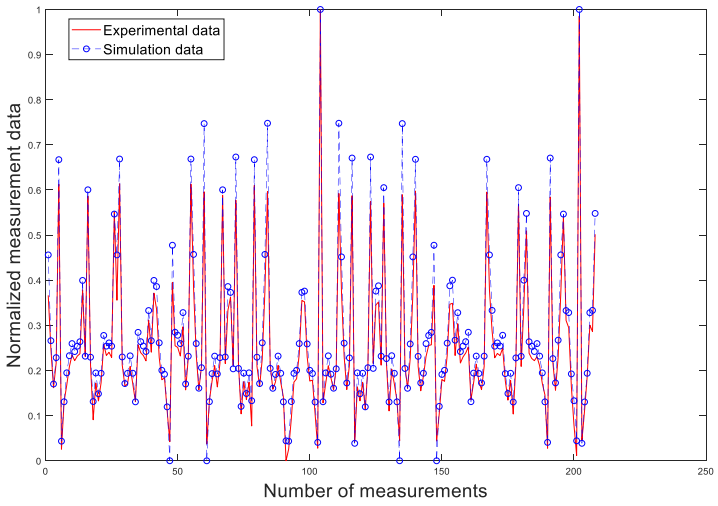

Figure 6.7: Comparison of normalized background data from simulation and experiment with EIT Planar Array

Position and depth tests are applied in this section, where the target has been placed at different positions and depths for each test. To simplify the illustration of each location of the sample, the region has been divided into a few areas, as shown in Figure (6.8). The top-view of the sensor has a 3×3 grid formed by the 16 electrodes, and each area could be renamed (for simplified description) as: Middle-left (ML), Middle-right (MR), Centre (C),

Upper-left (UL), Upper-middle (UM), Upper-right, Lower-left (LL), Lower-middle (LM), Lower-right (LR).

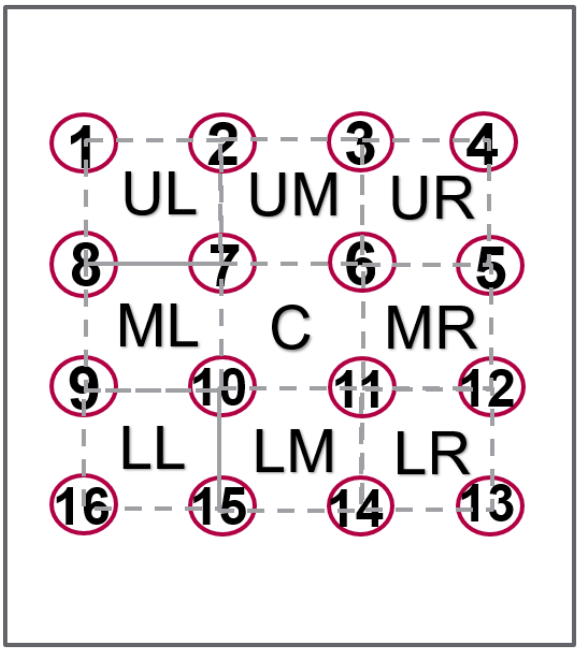

Figure 6.8: Simplified drawing of Subsurface ERT sensor

6.4.1 Position and depth detections

Above all, the capability of detecting different positions underneath the planar array is investigated. The metal cube has been placed at 6 positions with the same depth. Table 6.7 shows the pictures of the position detection experiments, and the reconstructed images using the SBTV algorithm are displayed in the right column.

Table 6.7: Optimized image reconstruction of **position detection**. The inclusion was placed on different locations to planar electrode array.

Locations	Photos (view from electrode plane)	Experimental results (optimized images)
ML	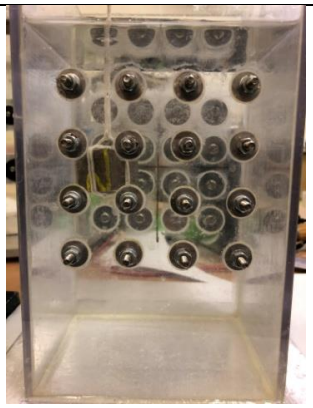	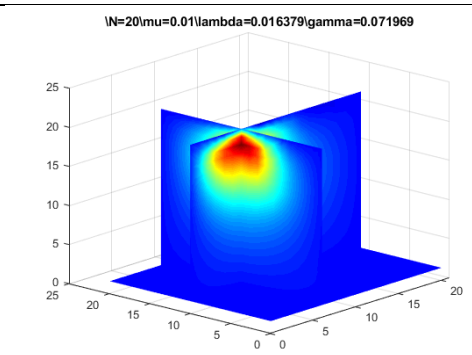
MR		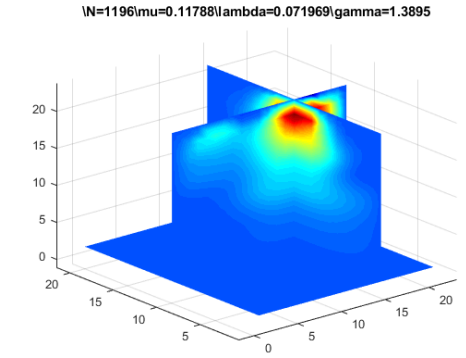
C	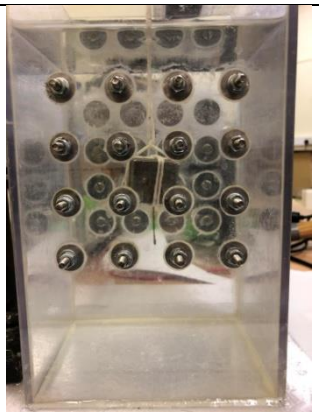	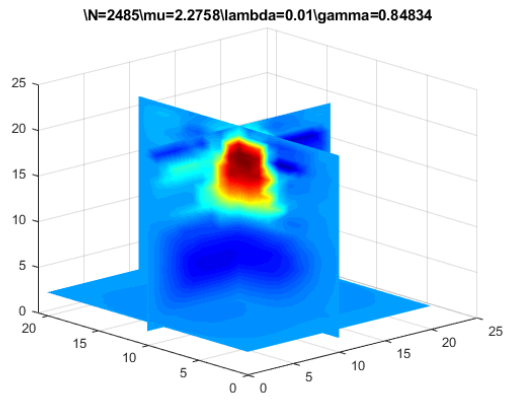

UL		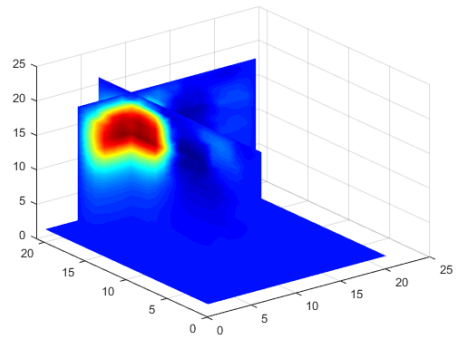
UM	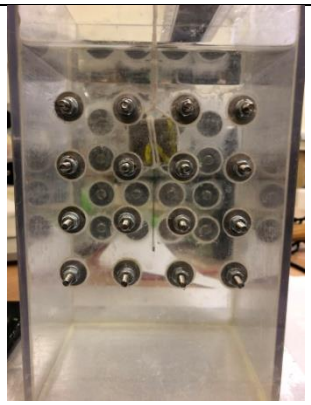	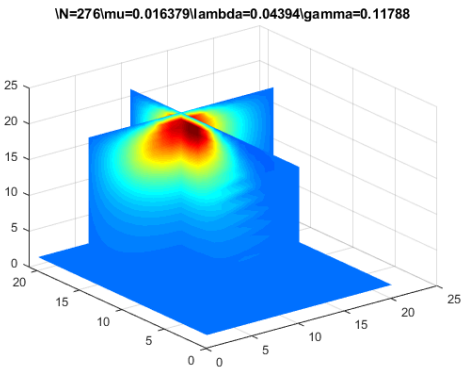
UR		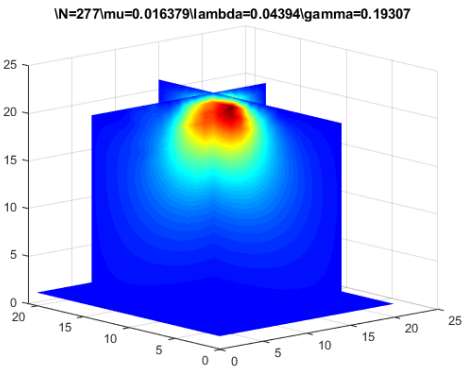

In order to produce good quality images using the experimental data, some quantitative parameters defined in section 2(c) are conducted for the purpose of selecting optimal parameters to be involved in the SBTV algorithm. The procedure of parameter selection was presented in section 2(d) in detail.

The SBTV algorithm has three parameters. The choice of the parameter can largely affect the reconstruction results when using TV regularization, and the residual error in numerical depth and volume are largely fluctuating. Figure 6.9 shows the results of numerical depth and volume with various combinations of parameters, such results mean some of the reconstructed images are actually very far from the truth and bias the expected result.

Hence, parameters should be optimized to obtain expected results. Manual parameter selection would require experts who are familiar with the TV algorithm and have knowledge of how each parameter would affect the image. However, TV regularisation is complicated, and such work would be time-consuming, and there were no much works suggesting how each parameter influence the reconstructions.

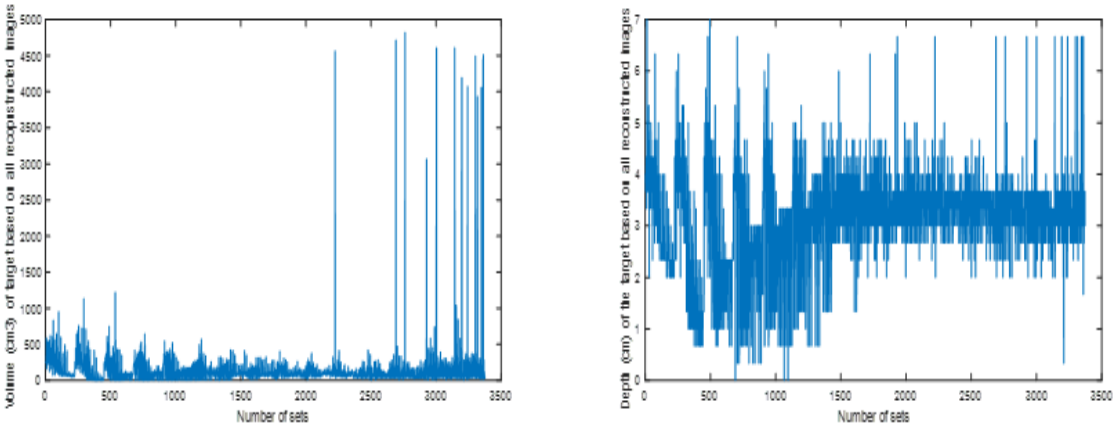

Figure 6.9: Plots of calculated volume and detected depth of the target based on reconstructed images using Planar Array with 3375 combinations of parameters.

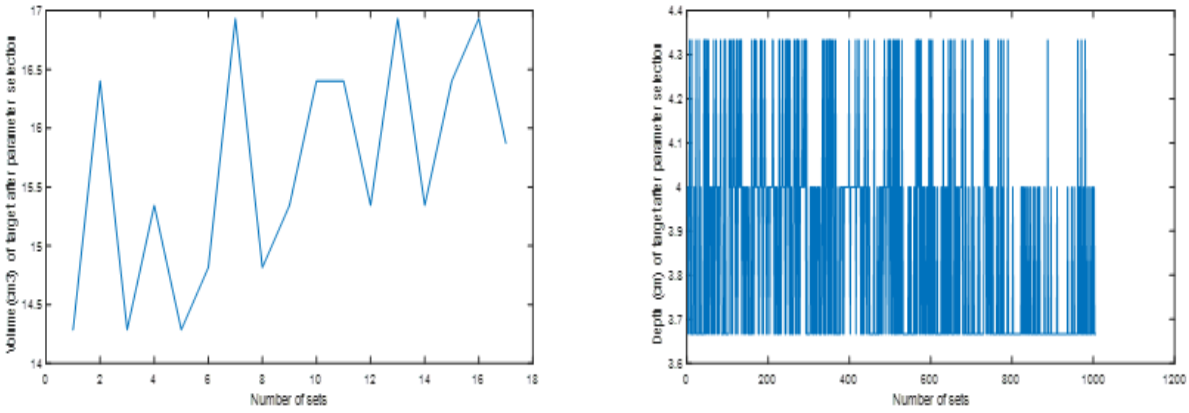

Figure 6.10: Results after applying parameter selection are displayed with the acceptable error of 10% on numerical depth and volume

Parameter selection in this chapter was manipulated using the procedure stated in the last section, where results with residual errors under 10% are considered acceptable. Results showing that relative error in the volume calculation of the target could be controlled to around 5% in all positions and different depths, which lead to the error being about 0.78

cm^3. In depth detection, the average residual error of the tested depth of up to 3cm could be controlled to be 0. For the depth of 4cm, the error in the center is slightly lower than other locations, and results located in the corners are showing a higher average relative error. However, for the planar array sensor that is employed in these experiments, the depth of 4cm is generally the detectable limit, since measurements would not react to further distances for such a small sensor, and such numerical analyses indicate the consistence between the result and the sensitivity mapping.

A series of experiments were conducted with the metal target hanging at positions UL, UM, UR, ML, C and MR with depths of 2cm, 3cm and 4cm measured from the center. For distances further than 4cm, the difference in measurement data from electrodes is hardly detectable, which indicates a detection limitation of the planar sensor of such a physical size.

Table 6.8: Numerical analysis of errors of reconstructed sample **volume** with respect to the actual volume of 15.625 cm^3

Depth(cm)/ error/ locations		UL	UM	UR	ML	Center	MR
2	**Measured volume / REV (%)**	15.380 cm^3/4.96%	15.560 cm^3/4.80%	15.953cm^3/5.70%	15.819cm^3/5.66%	16.177cm^3/6.5%	15.626cm^3/5.28%
3	**Measured volume / REV (%)**	15.849cm^3/5.10%	15.825cm^3/4.54%	15.575cm^3/5.74%	15.858cm^3/5.7%	15.790cm^3 / 5.47%	16.445cm^3/6.8%
4	**Measured volume / REV (%)**	16.169cm^3/6.83%	16.402cm^3/6.66%	15.814cm^3/5.44%	16.400cm^3/5.0%	16.100cm^3/6.09%	15.997cm^3/5.05%

Table 6.9: Numerical analysis of **position errors** of reconstructed sample with respect to actual depth

Depth(cm)/ error/ locations		UL	UM	UR	ML	Center	MR
2	**Measured Depth / RED (%)**	2cm/0%	2cm/0%	2cm/0%	2cm/0%	2cm/0%	2cm/0%
3	**Measured Depth / RED (%)**	3cm/0%	3cm/0%	3cm/0%	3cm/0%	3cm/0%	3cm/0%
4	**Measured Depth / RED (%)**	3.745cm/6.80 %	3.778cm/6.23 %	3.916cm/5.61 %	3.859cm/5.62 %	3.792cm/5.28 %	3.816cm/5.66 %

According to many experimental tests, it was discovered that optimized parameters based on volume fraction/ depth might not be the optimal combinations for detecting precise depth/ volume. In other words, the position error could still be large or over the expected standard although the volume is very close to the actual size of the tested sample, or ones with accurate depth might have an enlarged/shrunken volume of the target. For solving such a problem, joint constraints for training can be made to find out an 'overlapping' that satisfies both conditions. The flow chart illustrates the process of training. The position error is considered prior to the volume as the accuracy of depth is more important for detection purposes.

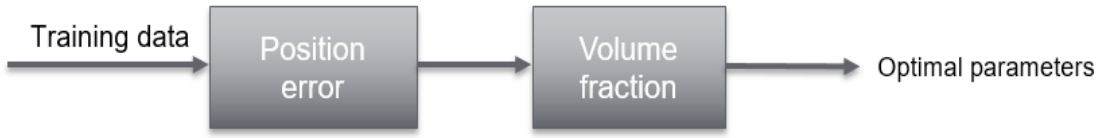

Figure 6.11: Flowchart of parameter optimization

Table 6.10: Image reconstruction of **depth detection**. Various depth was applied to each set with the metal cubic inclusion parallel to the center of the electrode plane.

Depth	Photos	Experimental results
2cm	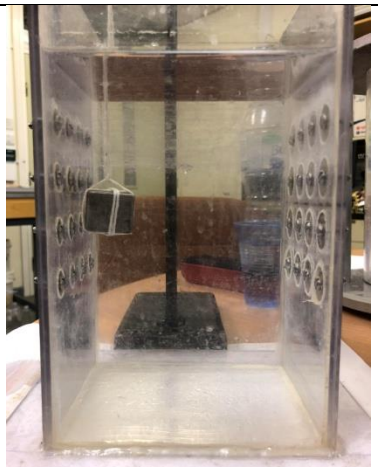	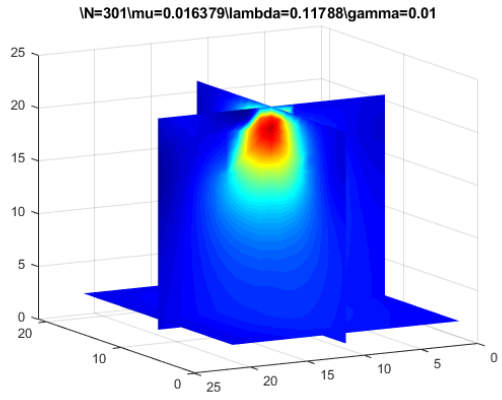
3cm	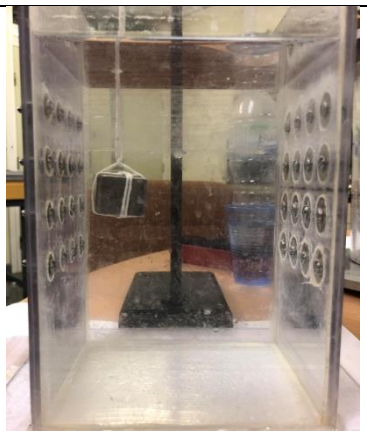	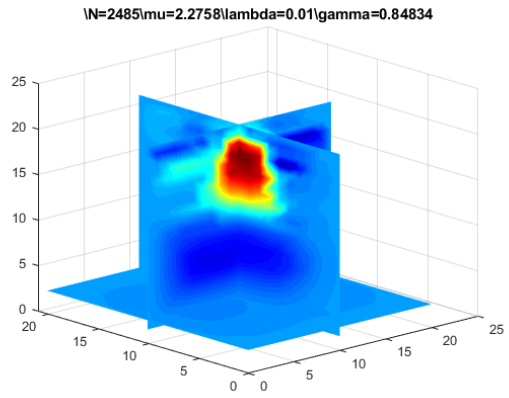
4cm	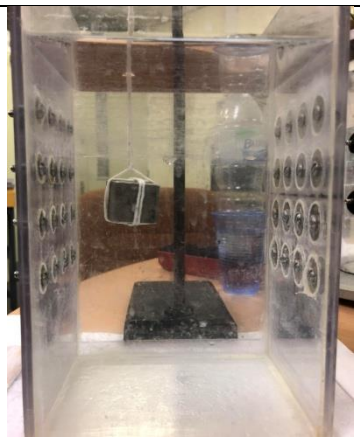	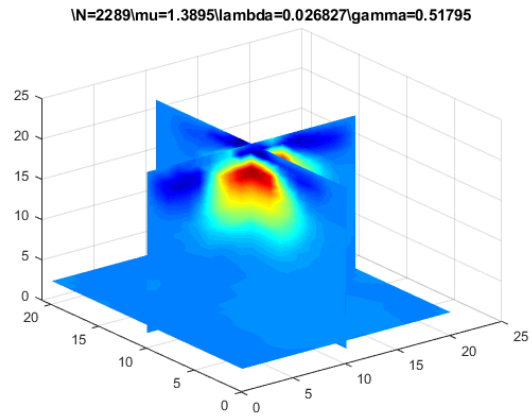

6.4.2 Analysis of gradient

Since the TV algorithm can reconstruct an image with a sharp boundary, the spatial gradient has the potential to explore useful information. visualizations of subsurface ERT in Figure (6.10) shows results using selected parameters with new experimental sampling data at different depths. Apparently, the recovered object has a sharp boundary on the side that is closest to the sensor, which corresponds to the distance between the top surface of the sample and the planar array if the image quality is high enough. The spatial gradient is given by the difference in conductivity distribution along the direction of interest. Smooth distributions would generate a gradient that is slowly stepping up/down, while a sharp gradient suggests a sharp boundary. The spatial gradient in the direction of depth is capable of discovering the upper boundary of the object which reflects the distance measured from the top surface to the electrode-plane. To conduct such an approach, new sampling data at depths of 2cm, 3cm, and 4cm are tested.

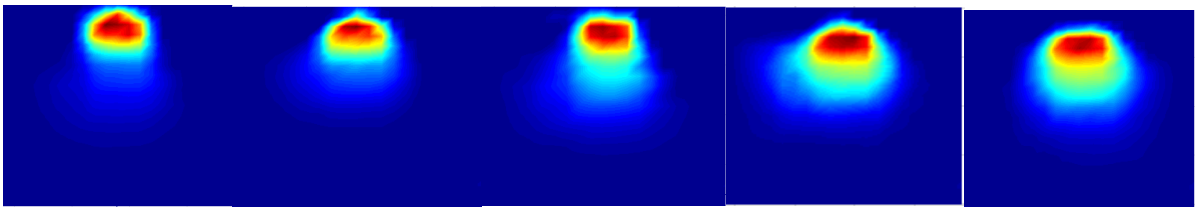

Figure 6.12: Visualization results of center position with various detection depth

Table 6.11: Distance measurement results based on images reconstruction reflected by spatial gradient

Depth	2cm	3cm	4cm
Distance (on top surface)	7.5mm	17.5mm	27.5mm

Spatial distribution	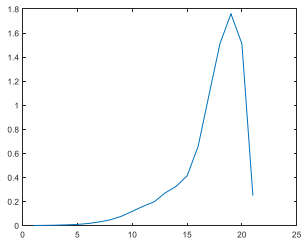	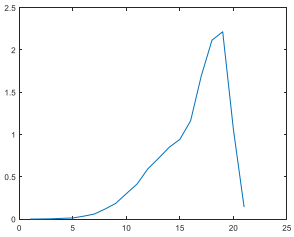	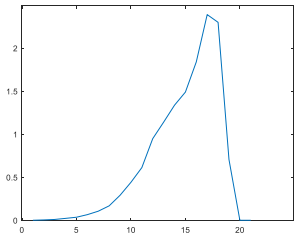
Spatial Gradient	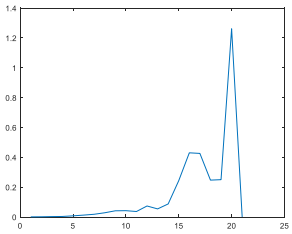	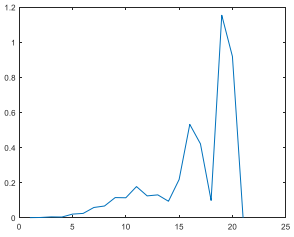	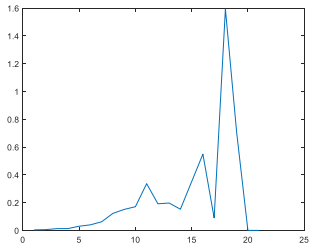
Reflected distance (mm)	6.67mm	13.33mm	20.00mm
Average Accuracy (%)	89.3%	76%	72.7%

The table above displays the spatial distribution conductivity values against the number of elements, where the reconstructed 3D image is composed of $21\times 21 \times 21$ elements. From the spatial distribution graphs, the growing tendency at the beginning is very smooth and steady and has a sharp change at the end. Such a result suggests the change of the sharpness along the direction of interest. The parts before and after the peak point correspond to the area underneath and above the top-boundary on reconstructed images. Sharpness on the top is far more than the region below the sample, this clarifies the truth that more information of the area near the top surface is recorded by electrodes, whilst missing data, as well as a weakened electric field on the other side, lead to a smoothing object boundary on reconstructed images. The absolute gradient demonstrates how fast the conductivity distribution varies along the plotted direction. The maximum peak value estimates the location of the upper boundary, and the corresponding pixel number on the 2D slice could be read from the x-axis, which is related to the distance between the upper

boundary and the subsurface sensor. Results suggest the accuracy of measuring distance using this method, and more error would be introduced with further distance to the planar-array due to image quality degradation. Numerical results show an accuracy of 89.3%-72.7% when the distance went from 2cm to 4cm. The number of elements that are setting up the reconstructed 3D images is actually limited for the purpose of saving computational time, and a 2D cross-sectional slice from the 3D image only contains 441 elements. Along the direction of depth, the limit number of elements may lead to degraded accuracy in calculations of distance. For the application stage in the future, an improvement in the element number would potentially contribute to a more precise measurement based on image reconstruction.

6.5 Conclusion

ERT is a visualization technique that produces images based on a sensitivity map and measurement data from electrodes in contact with a region of interest. Applications that use ERT can benefit from its features of high time resolution, low cost, and non-invasive. However, the inverse problem of ERT is ill-posed, and reconstructed images suffer from a low spatial resolution, especially in the cases of missing data. Subsurface ERT has been researched for a few decades. It is still a challenging problem despite many efforts has been put into many applications since the image quality might be degraded due to decaying of the current density on the region with deep distance. To detecting the depth of the targets, it is required to optimize the image quality, as a perfect image could reflect numerical parameter measurements. Total variation is capable of preserving the edge of the detected targets, although ERT planar array sensors suffer from data missing on the other side, a sharp boundary on the top surface is still observed. The visualized information of the target's topside is more critical while the bottom may be less important for sample detection purposes. Therefore, utilization of the TV algorithm can improve the image quality and spatial resolution of ERT reconstructed images, and visualizations of conductive objects in pipelines with ERT has great potential. In this chapter, the capability of the planar array has been investigated using a series of simulation and experimental phantom tests. Simulation has shown the feasibility of depth detection using an ERT planar array, and experiments have been carried out based on the simulation modelling. Visualization results

employing Split Bregman TV have been shown and discussed, where few quantitative parameters are defined for evaluating reconstructed images. In addition, a simple method has been suggested to select parameters aiming at producing qualified images. The imaging results showing that an ERT planar array with an overall size of 4.5cm×4.5cm could monitor to a depth of around 4cm, with a depth detection accuracy of up to 89.3%.

Chapter 7 Conclusions and Future Work

7.1 Conclusion

The purpose of this thesis is presenting works aiming at developing a better understanding on the boundary of materials by improving the performance of 2D/3D ERT for visualisations and quantitative analysis for potential applications in industrial flow pipelines, as the new emerging ERT technique is low-cost, has a high temporal resolution and is non-invasive for the tested targets. Many efforts have been made to upgrade the image quality by analyzing the inverse problem of 2D/3D dynamical ERT to improve the spatial/temporal performance of visualizing a moving target in a process tomography problem. The main contributions are based on TV regularisations, and a novel STTV algorithm is proposed to impose temporal information which is first being applied to dynamical ERT imaging. In addition, two types of sensors, conventional circular dual-plane sensors, and planar array sensors are investigated. Both sensor types have their own advantages, and a combination can potentially contribute to a high resolution, quality image. The contents of each chapter progressively demonstrate the procedures of gradually reaching the subjects. Each chapter of this thesis presents a specific problem, and the methods with valuable results are deeply discussed.

Previous works regarding the historical background and applications of ERT are reviewed in Chapter 1, where it proposes problems to be solved as well as procedures used in this thesis. Forward modelling and image reconstruction are two of the most important subjects for ERT. The Matlab-based software package known as EIDORS has been employed for assistance for forward modelling, and basic theory, including Maxwell's equations, forward mathematical modelling, basics of FEM and Jacobian, are reviewed and simple mathematical derivations are conducted. In the second chapter are the contents of ERT algorithms for solving the inverse problem, where two algorithms for static imaging, Tikhonov regularisation and Split Bregman Total Variation, are illustrated, and another two regularisations aiming at temporal imaging, Spatiotemporal Total Variation method and Temporal one-step solver, are demonstrated.

In chapter 4, a novel temporal regularisation method STTV for 2D dynamical imaging is proposed, and in particular, it represents how STTV performs for applications of a sharp

temporal 2D ERT visualization, which has never been attempted in ERT. ERT is a high temporal-resolution tomography modality, so STTV is supposed to be suitable for exploiting information along with both time and space. Experimental works are conducted by comparing STTV with the previously proposed temporal algorithm TOS. Quantitative analysis of reconstructed dynamical images, especially time response, show that the good sharpness of images from STTV benefits from a faster time response to the dynamical changing in the time domain. In this case, STTV not only shows a good performance in exploring spatial information, but also contributes to temporal information. Process tomography requires the exploitation of temporal information, which is difficult for conventional algorithms. This work suggests that STTV can help to develop more applications in industrial flow pipelines for dynamical processes.

In Chapter 5, 3D ERT with circular sensors is investigated with the extended STTV temporal algorithm. It represents the performance of STTV for monitoring a moving object. In addition, calculations of the velocity profile are expected in this work, and the cross-correlation method is supposed to be used to deal with the numerical calculation of time delay in order to work out the average speed of the moving target. By applying such an idea to both 2D and 3D ERT in simulation studies, the feasibility has been investigated. Experiments validate such a method, and the result of both image reconstructions and numerically calculated velocity are discussed. It verifies that a good time response is important in dynamical processes using a tomography-based method for the purpose of tracking or numerical analysis. Improvement of image quality can contribute to good time response and also spatial resolution, which means a better accuracy for quantitative calculations during the dynamical process. STTV can produce images with higher quality by benefitting from the capability of exploiting information from both spatial and temporal domains of the 3D imaging. The published journal paper suggested that such research work can potentially be developed for the real multiphase flow in industrial applications in the future.

Chapter 6 investigates 3D ERT with planar array sensors for further extending flow applications. Simulation and experiments are conducted, and both use SBTV for image reconstruction. Planar array sensors can represent better spatial distribution in axis-direction of flowing pipe compared with the sensor with two circular rings, although the

detectable region is relatively limited. However, these two types of 3D ERT can be combined to be a fusion-sensor, where a circular sensor can explore information concentrating on the center (undetectable for planar array) area, and the planar array sensor is responsible for visualizing the regions close to the electrode-plane. In other word, the performance of 3D ERT can be upgraded with the assistance of planar array based on the conventional multiple-ring circular sensor.

7.2 Future works

In this thesis, ERT for the application of flow imaging and basic measuring are researched by applying the novel temporal TV algorithm to 3D dynamical ERT, and also suggests that the information exploration can be better conducted using an ERT Planar array for 3D visualization, which further proposes the idea that two sensor types can be combined as a joint sensor that assembles the advantages of both. However, future works are still required for reaching the final target of being a mature technique in practical applications. In addition, this research can also be developed into more applications aside from flow visualizing. A list of further works and applications are suggested below:

- **Fusion-sensor for image quality improvement of 3D ERT**

In chapters 5 and 6, circular-ring and planar-array sensors are developed and evaluated separately. Although both show acceptable results in image reconstructions and numerical measurements, the approaches of combining information from both sensors are critical. With more complete information, theoretically, image quality can potentially be upgraded. For further study, a fusion-senor for 3D ERT should be designed, and more effort should also be made on information integration. Simulation and experimental validations can be conducted for evaluating the image quality from this method.

- **Real flow system**

All experimental data collected are from designed phantoms. Phantom studies are essential before applying novel ideas to real life, and real flow should be tested in the next stage of this work. Big differences exist between semi-dynamical movements conducted by phantom

studies and actual multi-phase flow in an industrial flow system. More noise will be present from different sources, such as, flow regime and pressure drop, which can bring many challenges. For the purpose of laboratory research, a small flow system can be designed to conduct flow loops with the generation of various flow regimes and enable data measurement via ERT sensors.

- **3D Flow Rheology with fusion-sensor**

Rheology generally describes the deformation behavior of materials. Regarding the motion of flow, deformation appearance is actually applied to fluid surfaces, which also lead to an inhomogeneous velocity of each spatial element. The combination of ERT sensors can potentially visualize real flow and also employ a velocity profile of the real flow. The circular ERT sensor can reflect information of the entire region, but the spatial resolution between electrode rings are low, whilst Planar array ERT sensor can exploit more information on the axis-direction of the pipe, which provides additional spatial information of flow pipes.

- **Open domain ERT imaging using a planar array**

Chapter 6 investigates the performance of subsurface ERT using TV algorithms, and the feasible domain of depth detection has been suggested with numerical analyses. In terms of the planar array sensor, it can be developed for open domain 3D ERT imaging. For most scenarios, the sensor cannot move as electrodes are normally directly connected to the solid medium, such as, the wall of the pipe or the ground. For the case that the domain being tested is a flexible liquid, a sensor board with electrodes embedded into it can be designed to enable the sensor to float on the top surface. On one hand, the movement of the sensor board can scan the top of the liquid medium to enable dynamical imaging using the planar array, on the other hand, horizontal rotation of the sensor board can collect more data for visualizing for more complete information underneath the domain.

- **Control with temporal TV algorithm**

Tomography-based control systems can potentially be developed in the future. In industrial processes, quantitative parameters are important. For example, the monitoring of oil-water two-phase flow can reflect information relating to, for instance, water disposal or reinjection. For the purpose of control, a real-time modality with a high time response is required. Based on the discoveries of the temporal TV algorithm showing a good time response, it could potentially be applied to a real-time visualization technique for exploiting information from the objects, and reflect quantitative factors for the purpose of control.

Bibliography

[1] A. Yao and M. Soleimani (2012) A pressure mapping imaging device based on electrical impedance tomography of conductive fabrics, Bath, UK.

[2] Dahlin, T. (2001). The development of DC resistivity imaging techniques. Computers & Geosciences, 27(9), 1019-1029. Doi:10.1016/s0098-3004(00)00160-6.

[3] Henderson, R. P., & Webster, J. G. (1978). An Impedance Camera for Spatially Specific Measurements of the Thorax. IEEE Transactions on Biomedical Engineering IEEE Trans. Biomed. Eng., BME-25(3), 250-254. doi:10.1109/tbme.1978.326329.

[4] Harris, N., Suggett, A., Barber, D., & Brown, B. (1987). Applied Potential Tomography (APT) - A New Technique for Monitoring Lung Function. Clin. Sci. Clinical Science, 72(S16). doi:10.1042/cs072005pb.

[5] Jossinet J J, Fourcade C and Schmitt M. (1981). A study for breast imaging with a circular array of impedance electrodes Proc. Vth International Conference Electrical Bioimpedance (ICEBI). Tokyo.

[6] Murdoch N, Murray P W, Rolfe P and Weindling A M. (1981). Computer modelling of cerebral electrical impedance in the newborn baby for comparison with in vivo measurements, Proc. 5th Nordic Med. and Biol. Engng Conf. Linkoping, Sweden. vol. 2. p 4 18-20.

[7] Barber, D. C., & Brown, B. H. (1984). Applied potential tomography. J. Phys. E: Sci. Instrum. Journal of Physics E: Scientific Instruments, 17(9), 723-733. doi:10.1088/0022-3735/17/9/002.

[8] Davide S Holder (n.d.) Electrical Impedance Tomography of brain function, London, UK.

[9] Harris, N. D., Suggett, A. J., Barber, D. C., & Brown, B. H.(1988). Applied potential tomography: A new technique for monitoring pulmonary function. Clinical Physics and Physiological Measurement Clin. Phys. Physiol. Meas., 9(4A), 79-85. doi:10.1088/0143.

[10] Mangnall, Y. F., Baxter, A. J., Avill, R., Bird, N. C., Brown, B. H., Barber, D. C., . . . Read, N. W. (1987). Applied potential tomography: A new noninvasive technique for assessing gastric function. Clinical Physics and Physiological Measurement Clin. P.

[11] Hu, J. and Soleimani, M. (2017). Deformable boundary EIT for breast cancer imaging. Biomedical Physics & Engineering Express, 3(1), p.015004.

[12] Conway, J. (1987). Electrical impedance tomography for thermal monitoring of hyperthermia treatment: An assessment using in vitro and in vivo measurements. Clinical Physics and Physiological Measurement Clin. Phys. Physiol. Meas., 8(4A), 141-146. doi:10.1.

[13] Tushar Kanti Bera, Application of Electrical Impedance Tomography (EIT): A Short Review, (2018). IOP Conf. Ser.: Mater. Sci. Eng. 331 012004.

[14] Tsung-Chin Hou, Kenneth J Loh and Jerome P Lynch. (2007). Spatial conductivity mapping of carbon nanotube composite thin films by electrical impedance tomography for sensing applications, Nanotechnology 18 (2007).

[15] Meir, A.; Rubinsky, B. (2014). Electrical impedance tomographic imaging of a single cell electroporation. Biomed. Microdevices, 16, 427–437.

[16] Wu, H., Zhou, W., Yang, Y., Jia, J. and Bagnaninchi, P. (2018). Exploring the Potential of Electrical Impedance Tomography for Tissue Engineering Applications. Materials, 11(6), p.930.

[17] Pontus Linderholm, Laurent Marescot, Meng Heng Loke, and Philippe Renaud. (2008). Cell Culture Imaging Using Microimpedance Tomography, 138 IEEE Trans Biomed Eng., Vol. 55, No. 1, pp 138-146.

[18] Tao Sun, Soichiro Tsuda, Klaus-Peter Zauner, Hywel Morgan. (2010). On-chip electrical impedance tomography for imaging biological cells, Biosensors and Bioelectronics 25 1109–1115.

[19] T. Sun, S. Tsuda, N.G. Green, K.P. Zauner and H. Morgan. (2008). On-Chip Electrical Impedance Tomography for Moniroting The Kinetics in The Cell Culture, Twelfth International Conference on Miniaturized Systems for Chemistry and Life Sciences, USA, pp 973-9.

[20] Kawashima, D., Liu, X., Sugawara, M., Obara, H. and Takei, M. (2018). Image Reconstruction Algorithm for Visualization of Cell Living Rate in Microchannel with Multi-layer Electrodes by Micro Electrical Impedance Tomography. In: 9th WORLD CONGRESS.

[21] Wang, M. and Cilliers, J. (1999). Detecting non-uniform foam density using electrical resistance tomography. Chemical Engineering Science, 54(5), pp.707-712.

[22] Henningsson, M., Östergren, K. and Dejmek, P. (2006). Plug flow of yoghurt in piping as determined by cross-correlated dual-plane electrical resistance tomography. Journal of Food Engineering, 76(2), pp.163-168.

[23] Jia, J., Wang, H. and Millington, D. (2017). Electrical Resistance Tomography Sensor for Highly Conductive Oil-Water Two-Phase Flow Measurement. IEEE Sensors Journal, 17(24), pp.8224-8233.

[24] F. D. Chao Tan. (2010). Cross Correlation Velocity of Oil-water Two-Phase Flow by a Dual-Plane Electrical Resistance Tomography System. IEEE, Tianjin, China.

[25] Y. Faraj et al. (2015). Measurement of vertical oil-in-water two-phase flow using dual-modality ERT-EMF system. Flow Meas. Instrum., vol. 46, pp. 255–261.

[26] Tan, C., Wang, N. and Dong, F. (2016). Oil–water two-phase flow pattern analysis with ERT based measurement and multivariate maximum Lyapunov exponent. Journal of Central South University, 23(1), pp.240-248.

[27] Dong, F., Xu, Y., Xu, L., Hua, L. and Qiao, X. (2005). Application of dual-plane ERT system and cross-correlation technique to measure gas–liquid flows in vertical upward pipe. Flow Measurement and Instrumentation, 16(2-3), pp.191-197.

[28] Dong, F., Jiang, Z., Qiao, X. and Xu, L. (2003). Applicationof electrical resistance tomography to two-phase pipe flow parameters measurement. Flow Measurement and Instrumentation, 14(4-5), pp.183-192.

[29] Dong, F., Xu, Y., Qiao, X., Xu, L. and Xu, L. (2008). Void Fraction Measurement for Two-Phase Flow Using Electrical Resistance Tomography. The Canadian Journal of Chemical Engineering, 83(1), pp.19-23.

[30] Olerni, C., Jia, J. and Wang, M. (2013). Measurement of air distribution and void fraction of an upwards air–water flow using electrical resistance tomography and a wire-mesh sensor. Measurement Science and Technology, 24(3), p.035403.

[31] Fransolet, E., Crine, M., L'Homme, G., Toye, D. and Marchot, P. (2001). Analysis of Electrical Resistance Tomography Measurements Obtained on a Bubble Column. Chemie Ingenieur Technik, 73(6), pp.754-754.

[32] JIN, H., WANG, M. and WILLIAMS, R. (2007). Analysis of bubble behaviors in bubble columns using electrical resistance tomography. Chemical Engineering Journal, 130(2-3), pp.179-185..

[33] Chen, B., Abascal, J. and Soleimani, M. (2018). Extended Joint Sparsity Reconstruction for Spatial and Temporal ERT Imaging. Sensors, 18(11), p.4014.

[34] Chen, B.; Abascal, J.F.P.J.; Soleimani, M. (2018). Electrical Resistance Tomography for Visualization of Moving Objects Using a Spatiotemporal Total Variation Regularization Algorithm. Sensors. 18, 1704.

[35] Holder, D. (2005). Electrical impedance tomography. London: Department of Medical Physics and Bioengineering, pp.21-22.

[36] Ahn, S., Jun, S., Seo, J., Lee, J., Woo, E. and Holder, D. (2010). Frequency-difference electrical impedance tomography: Phantom imaging experiments. Journal of Physics: Conference Series, 224, p.012152.

[37] Seo, J., Lee, J., Kim, S., Zribi, H. and Woo, E. (2008). Frequency-difference electrical impedance tomography (fdEIT): algorithm development and feasibility study. Physiological Measurement, 29(8), pp.929-944.

[38] L. M. Heikkinen, J. Kourunen, T. Savolainen, P. J. Vauhkonen, J. P. Kaipio, and M. Vauhkonen, (2006). Real time three-dimensional electrical impedance tomography applied in multiphase flow imaging. Meas. Sci. Technol., vol. 17, no. 8, pp. 2083–2087.

[39] Fan, W. and Wang, H. (2009). A fast three-dimensional image reconstruction method for ERT. In: IST 2009 - International Workshop on Imaging Systems and Techniques.

[40] Cao, Z. and Xu, L. (2013). Direct Image Reconstruction for 3-D Electrical Resistance Tomography by Using the Factorization Method and Electrodes on a Single Plane. IEEE Transactions on Instrumentation and Measurement, 62(5), pp.999-1007.

[41] Bayford, R. (2006). BIOIMPEDANCE TOMOGRAPHY (ELECTRICAL IMPEDANCE TOMOGRAPHY). Annual Review of Biomedical Engineering, 8(1), pp.63-91.

[42] Kolehmainen, V., Vauhkonen, M., Karjalainen, P. and Kaipio, J. (1997). Assessment of errors in static electrical impedance tomography with adjacent and trigonometric current patterns. Physiological Measurement, 18(4), pp.289-303.

[43] Adler, A., Dai, T. and Lionheart, W. (2007). Temporal image reconstruction in electrical impedance tomography. Physiological Measurement, 28(7), pp.S1-S11.

[44] Vauhkonen, M., et al.(1998). A Kalman Filter Approach to Track Fast Impedance Changes in Electrical Impedance Tomography." IEEE Transactions on Biomedical Engineering, vol. 45, no. 4, pp. 486–493., doi:10.1109/10.664204.

[45] Chen, Bo, et al. (2018). Electrical Resistance Tomography for Visualization of Moving Objects Using a Spatiotemporal Total Variation Regularization Algorithm. Sensors, vol. 18, no. 6, p. 1704., doi:10.3390/s18061704.

[46] Vauhkonen, P. J., et al. (2000). Dynamic Electrical Impedance Tomography - Phantom Studies. Inverse Problems in Engineering, vol. 8, no. 5, pp. 495–510.

[47] Brown B H and Seagar A D. (1987). The Sheffield data collection system Clin. Phys. Physiol. Meas. 8 (suppl A) 91–7.

[48] Brown B H, Barber D C, Leathard A D, Lu L, Wang W, Smallwood R H and Wilson A J. (1994). High frequency EIT data collection and parameteric imaging Innovation Technol. Biol. Med. 15 1–8.

[49] Wilson, A. J., Milnes, P., Waterworth, A. R., Smallwood, R. H., & Brown, B. H. (2001). Mk3.5: A modular, multi-frequency successor to the Mk3a EIS/EIT system. Physiological Measurement, 22(1), 49-54. doi:10.1088/0967-3334/22/1/307.

[50] C.N.McLeod, F.J.Lidgey and Q.S.Zhu (n.d.) Multiple drive EIT systems, Oxford.

[51] Q S Zhu, C N McLeod, C W Denyer, F J Lidgey and W R B Lionheart. (1994). Development of a real-time adaptive current tomograph, UK.

[52] Eung Je Woo (2007) Impedance Spectroscopy and Multi-Frequency Electrical Impedance tomography, Korea.

[53] D Y Kim, H Wi, P J Yoo, T I Oh and E J Woo. (2010). Performance evaluation of KHU Mark2 parallel multi-frequency EIT system, Korea.

[54] Tong In Oh, Hun Wi, Do Yub Kim, Pil Joong Yoo and Eung Je Woo. (2011). A fully parallel multi-frequency EIT system with flexible electrode configuration: KHU Mark2, Korea.

[55] Silvera-Tawil, D., Rye, D., Soleimani, M., & Velonaki, M. (2015). Electrical Impedance Tomography for Artificial Sensitive Robotic Skin: A Review.Sensors Journal, IEEE, 15(4), 2001-2016.

[56] N. Avis and D. Barber. (1994). Image reconstruction using non-adjacent drive configurations," Physiological Measurement, vol. 15, no. 15, pp. A153– A160.

[57] C. Xu, X. Dong, X. Shi, F. Fu, W. Shuai, R. Liu, and F. You. (2008). Comparison of drive patterns

for single current source EIT in computational phantom," in Proc. IEEE International Conference Bioinformatics and Biomedical Engineering, pp. 1500–1503.

[58] X. Shi, X. Dong, W. Shuai, F. You, F. Fu, and R. Liu. (2006). Pseudo-polar drive patterns for brain electrical impedance tomography. Physiological Measurement, vol. 27, no. 11, pp. 1071–1080.

[59] D. Silvera Tawil, D. Rye, and M. Velonaki. (2009). Improved EIT drive patterns for a robotics sensitive skin. in Proc. Australasian Conference on Robotics and Automation.

[60] J. a. Andy Adler. (2016). Electrical impedance tomography in 3D using two electrode planes: characterization and evaluation," vol. 37.

[61] Holder, D. (2005). Electrical impedance tomography: Methods, History and Applications. London: Institute of Physics, p.23.

[62] Somersalo, E., Cheney, M. and Isaacson, D. (1992). Existence and Uniqueness for Electrode Models for Electric Current Computed Tomography. SIAM Journal on Applied Mathematics, 52(4), pp.1023-1040.

[63] Boyle, A. and Adler, A. (2011). The impact of electrode area, contact impedance and boundary shape on EIT images. Physiological Measurement, 32(7), pp.745-754.

[64] K-S. Cheng, D. Isaacson, J. C. Newell, and D. G. Gisser. (1989). Electrode models for electric current computed tomography. IEEE Trans. Biomed. Eng., vol. 36, no. 9, pp. 918-924.

[65] Michael Graham, B. (2019). Enhancements in EIT Image Reconstruction for 3D Lung Imaging. Ph.D. University of Ottawa.

[66] Polydorides N and Lionheart W R B. (2002). A Matlab toolkit for three-dimensional electrical impedance tomography: a contribution to the Electrical Impedance and Diffuse Optical Reconstruction Software project Meas. Sci. Technol. 13 1871–1883.

[67] Holder, D. (2005). Electrical impedance tomography: Methods, History and Applications. London: Institute of Physics, p.46-48.

[68] Santosa, F. and Vogelius, M. (1990). A Backprojection Algorithm for Electrical Impedance Imaging. SIAM Journal on Applied Mathematics, 50(1), pp.216-243.

[69] M.Cheney,D.Isaacson,J.C.Newell,S.Simake,andJ.Goble. (1990). Noser: An algorithm for solving the inverse conductivity problem. Int. J. Imag. Syst. Technol., vol. 2, pp. 66–75.

[70] Vauhkonen, M., Vadasz, D., Karjalainen, P., Somersalo, E. and Kaipio, J. (1998). Tikhonov regularization and prior information in electrical impedance tomography. IEEE Transactions on Medical Imaging, 17(2), pp.285-293.

[71] B. Brandstatter, G. Holler, and D. Watzenig. (2003). Reconstruction of inhomogeneities in fliuids by means of capacitance tomography. COMPEL: The international Journal for Computation and Mathematics in Electrical and Electronic Engineering, 22(3): 508-519.

[72] Li, Y. and Yang, W. (2008). Image reconstruction by nonlinear Landweber iteration for complicated distributions. Measurement Science and Technology, 19(9), p.094014.

[73] X. Song, Y. Xu, F. Dong. (2015). A spatially adaptive total variation regularization method for electrical resistance tomography'. Meas. Sci. Technol. 26, 125401 (15pp).

[74] Goldstein, T.; Osher, S. (2009). The Split Bregman Method for L1-Regularized Problems. SIAM J. Imaging Sci. 2, 323–343.

[75] Zhou, Zhou, et al. (2015). Comparison of Total Variation Algorithms for Electrical Impedance Tomography. Physiological Measurement, vol. 36, no. 6, pp. 1193–1209., doi:10.1088/0967-3334/36/6/1193.

[76] Nasehi Tehrani, J., McEwan, A., Jin, C. and van Schaik, A. (2012). L1 regularization method in electrical impedance tomography by using the L1-curve (Pareto frontier curve). Applied Mathematical Modelling, 36(3), pp.1095-1105.

[77] Rudin, L., Osher, S. and Fatemi, E. (1992). Nonlinear total variation based noise removal algorithms. Physica D: Nonlinear Phenomena, 60(1-4), pp.259-268.

[78] C. R. Vogel and M. E. Oman. (1996). Iterative methods for total variation denoising," SIAM J. Sci. Comput., vol. 17, pp. 227–238.

[79] Li, F., Abascal, J., Desco, M. and Soleimani, M. (2017). Total Variation Regularization With Split Bregman-Based Method in Magnetic Induction Tomography Using Experimental Data. IEEE Sensors Journal, 17(4), pp.976-985.

[80] Tholin-Chittenden, C., Abascal, J. and Soleimani, M. (2018). Automatic Parameter Selection of Image Reconstruction Algorithms for Planar Array Capacitive Imaging. IEEE Sensors Journal, 18(15), pp.6263-6272.

[81] Borsic, A. (2002). Regularisation Methods for Imaging from Electrical Measurements. Ph.D. Oxford Brookes University.

[82] Andersen K D, Christiansen E, Conn A R and Overton M L. (1999). An efficient primal-dual interior-point method for minimizing a sum of euclidean norms SIAM J. Sci. Comput. 22 243–62.

[83] Li, F., Soleimani, M. and Abascal, J. (2018). Planar array magnetic induction tomography further improvement. Sensor Review.

[84] Abascal, J., Montesinos, P., Marinetto, E., Pascau, J. and Desco, M. (2014). Comparison of Total Variation with a Motion Estimation Based Compressed Sensing Approach for Self-Gated Cardiac Cine MRI in Small Animal Studies. PLoS ONE, 9(10), p.e110594.

[85] Adler, A., Arnold, J., Bayford, R., Borsic, A., Brown, B., Dixon, P., Faes, T., Frerichs, I., Gagnon, H., Gärber, Y., Grychtol, B., Hahn, G., Lionheart, W., Malik, A., Patterson, R., Stocks, J., Tizzard, A., Weiler, N. and Wolf, G. (2009). GREIT: a unifie.

[86] Yadigaroglu, G. and Hewitt, G. (2018). Introduction to Multiphase Flow. Cham: Springer International Publishing.pp10-13.

[87] Rite.or.jp. (2019). Various Methods of Generating Electricity | RITE Systems Analysis Group. [online] Available at: https://www.rite.or.jp/system/en/learn-energy/energy-use/hatsuden/

[Accessed 13 Mar. 2019].

[88] Zeroco2.no. (2019). What is CCS? — zeroco2. [online] Available at: http://www.zeroco2.no/introduction/what-is-ccs [Accessed 13 Mar. 2019].

[89] Gasflooding.com. (2019). Gas Flooding | GasFlooding.com. [online] Available at: http://www.gasflooding.com/ [Accessed 13 Mar. 2019].

[90] Meziou, A., Chaari, M., Franchek, M., Borji, R., Grigoriadis, K. and Tafreshi, R. (2016). Low-Dimensional Modeling of Transient Two-Phase Flow in Pipelines. Journal of Dynamic Systems, Measurement, and Control, 138(10), p.101008.

[91] Hernández, L., Juliá, J., Chiva, S., Paranjape, S. and Ishii, M. (2006). Fast classification of two-phase flow regimes based on conductivity signals and artificial neural networks. Measurement Science and Technology, 17(6), pp.1511-1521.

[92] Torres, Carlos. (2005). Modeling of oil-water flow in horizontal and near horizontal pipes. 10.13140/2.1.3305.0565.

[93] Xu, X. (2007). Study on oil–water two-phase flow in horizontal pipelines. Journal of Petroleum Science and Engineering, 59(1-2), pp.43-58.

[94] Ismail, A., Ismail, I., Zoveidavianpoor, M., Mohsin, R., Piroozian, A., Misnan, M. and Sariman, M. (2015). Review of oil–water through pipes. Flow Measurement and Instrumentation, 45, pp.357-374.

[95] Wang, M. (2015). Industrial tomography. UK: Woodhead Publishing is an imprint of Elsevier, pp.434-438.

[96] Olerni, C., Jia, J. and Wang, M. (2013). Measurement of air distribution and void fraction of an upwards air–water flow using electrical resistance tomography and a wire-mesh sensor. Measurement Science and Technology, 24(3), p.035403.

[97] Tan, C. (2009). Multisensor Fusion Based Measurement on Two-phase Flow Parameters. Ph.D. Tianjin University.

[98] Yadigaroglu, G. and Hewitt, G. (2018). Introduction to multiphase flow. Cham: Springer, pp.58-74.

[99] Tan, C., Dong, F. and Wu, M. (2007). Identification of gas/liquid two-phase flow regime through ERT-based measurement and feature extraction. Flow Measurement and Instrumentation, 18(5-6), pp.255-261.

[100] Tan, C. and Dong, F. (2009). Gas-Water Two-Phase Flow Regime Identification with Feature Fusion from an ERT System and a VCone Meter. In: International Workshop on Imaging Systems and Techniques.

[101] Zhang Y., Chen Y. (2012) A Novel PCA-SVM Flow Pattern Identification Algorithm for Electrical Resistance Tomography System. In: Jin D., Lin S. (eds) Advances in Future Computer and Control Systems. Advances in Intelligent and Soft Computing, vol 160. Spri.

[102] Zhang, Y. (2015). A Novel Identification Method of Two Phase Flow Based on LDA Feature Extraction and GRNN in ERT System. In: International Symposium on Knowledge Acquisition and Modeling. Atlantis Press.

[103] Karki, B, Faraj, Y and Wang, M (2016) Electrical Conductivity Based Flow Regime Recognition of Two-phase Flows in Horizontal pipeline. In: WCIPT8 Proceedings. 8th World Congress on Industrial Process Tomography, 26-29 Sep 2016, Iguassu Falls, Brazil.

[104] Deng, X, Dong, F, Xu, L.J, Liu, X.P. Xu, L.A. (2001). The design of a dual-plane ERT system for cross correlation measurement of bubbly gas/liquid pipe flow. Meas. Sci. Technol. 12, 1024–1031.

[105] Dong, F, Xu, Y, Xu, L, Hua, L, Qiao, X. (2005). Application of dual-plane ERT system and cross-correlation technique to measure gas–liquid flows in vertical upward pipe. Flow Meas. Instrum. 16, 191–197.

[106] Wu, Y, Li, H, Wang, M, Williams, R. (2008). Characterization of Air-Water Two-Phase Vertical Flow by Using Electrical Resistance Imaging. Can. J. Chem. Eng. 83, 37–41.

[107] Dai, Y., Wang, M., Panayotopoulos, N., Lucas, G. and Williams, R. (2019). 3-D Visualisation of a Swirling Flow Using Electrical Resistance Tomography. In: 4th World Congress on Industrial Process Tomography.

[108] Wang, M., Jones, T. and Williams, R. (2003). Visualization of Asymmetric Solids Distribution in Horizontal Swirling Flows Using Electrical Resistance Tomography. Chemical Engineering Research and Design, 81(8), pp.854-861.

[109] Stevenson, R., Harrison, S., Miles, N. and Cilliers, J. (2006). Examination of swirling flow using electrical resistance tomography. Powder Technology, 162(2), pp.157-165.

[110] S. Ren, C. Tan and F. Dong. (2012). Two phase flow visualization in an annular tube by an Electrical Resistance Tomography. 2012 IEEE International Conference on Imaging Systems and Techniques Proceedings, Manchester, pp. 488-492.

[111] Sharifi, M. and Young, B. (2011). 3-Dimensional spatial monitoring of tanks for the milk processing industry using electrical resistance tomography. Journal of Food Engineering, 105(2), pp.312-319.

[112] Ma, Y., Zheng, Z., Xu, L., Liu, X. and Wu, Y. (2001). Application of electrical resistance tomography system to monitor gas/liquid two-phase flow in a horizontal pipe. Flow Measurement and Instrumentation, 12(4), pp.259-265.

[113] Y. Xu, H. Wang, Z. Cui and F. Dong. (2009). Application of electrical resistance tomography for slug flow measurement in gas/liquid flow of horizontal pipe. 2009 IEEE International Workshop on Imaging Systems and Techniques, Shenzhen, pp. 319-323.

[114] Na, W., Jia, J., Yu, X., Faraj, Y., Wang, Q., Meng, Y., Wang, M. and Sun, W. (2015). Imaging of gas–liquid annular flows for underbalanced drilling using electrical resistance tomography. Flow Measurement and Instrumentation, 46, pp.319-326.

[115] Wang, M., Lucas, G., Dai, Y., Panayotopoulos, N. and Williams, R. (2006). Visualisation of Bubbly Velocity Distribution in a Swirling Flow Using Electrical Resistance Tomography. Particle & Particle Systems Characterization, 23(3-4), pp.321-329.

[116] Qiu C, Hoyle B S and Podd F J W (2007), Engineering and application of a dual-modality process tomography system, Flow Meas. and Instrum., 18, pp 247-254.

[117] Yi Li and W. Yang. (2009)Measurement of multi-phase distribution using an integrated dual-modality sensor. 2009 IEEE International Workshop on Imaging Systems and Techniques, Shenzhen, pp. 335-339.

[118] Sun, J. and Yang, W. (2015). A dual-modality electrical tomography sensor for measurement of gas–oil–water stratified flows. Measurement, 66, pp.150-160.

[119] Q. Wang, M. Wang, K. Wei and C. Qiu. (2017). Visualization of Gas–Oil–Water Flow in Horizontal Pipeline Using Dual-Modality Electrical Tomographic Systems. in IEEE Sensors Journal, vol. 17, no. 24, pp. 8146-8156.

[120] Wang, Q., Polansky, J., Wang, M., Wei, K., Qiu, C., Kenbar, A. and Millington, D. (2018). Capability of dual-modality electrical tomography for gas-oil-water three-phase pipeline flow visualisation. Flow Measurement and Instrumentation, 62, pp.152-166.

[121] Faraj, Y., Wang, M., Jia, J., Wang, Q., Xie, C., Oddie, G., Primrose, K. and Qiu, C. (2015). Measurement of vertical oil-in-water two-phase flow using dual-modality ERT–EMF system. Flow Measurement and Instrumentation, 46, pp.255-261.

[122] Mahmud, M., Faraj, Y. and Wang, M. (2015). Visualisation and Metering of Two Phase Counter-gravity Slurry Flow using ERT. Procedia Engineering, 102, pp.930-935.

[123] Meng, Z., Huang, Z., Wang, B., Ji, H., Li, H. and Yan, Y. (2010). Air–water two-phase flow measurement using a Venturi meter and an electrical resistance tomography sensor. Flow Measurement and Instrumentation, 21(3), pp.268-276.

[124] Soleimani, Manuchehr, et al. (2007). Dynamic Imaging in Electrical Capacitance Tomography and Electromagnetic Induction Tomography Using a Kalman Filter. Measurement Science and Technology, vol. 18, no. 11, pp. 3287–3294., doi:10.1088/0957-0233/18/11/004.

[125] Vauhkonen, M, Lionheart, W, Heikkinen, L, Vauhkonen, P.; Kaipio, J. (2001). A MATLAB package for the EIDORS project to reconstruct two-dimensional EIT images. Phys. Meas. 22, 107–111.

[126] “EIT Technology.” Swisstom, Available: www.swisstom.com/en/eit-technology-3.

[127] Beck, M.; Pla˛skowski, A. (1987). Cross Correlation Flowmeters; Hilger: Bristol, UK.

[128] Gurau, B.; Vassallo, P.; Keller, K. (2004). Measurement of gas and liquid velocities in an air–water two-phase flow using cross-correlation of signals from a double sensor hot-film probe. Exp. Therm. Fluid Sci. 28, 495–504.

[129] Saoud, A.; Mosorov, V.; Grudzien, K. (2017). Measurement of velocity of gas/solid swirl flow using Electrical Capacitance Tomography and cross correlation technique. Flow Meas. Instrum.

53, 133–140.

[130] Banasiak, Z.R.; Ye, M. Soleimani. (2012). Improving three-dimensional electrical capacitance tomography imaging using approximation error model theory. J. Electromagn. Waves Appl, 26, 411–421.

[131] Soleimani, M.; Wang, H.G.; Li, Y.; Yang, W.Q. (2007).A comparative study of 3d electrical capacitance tomography. Int. J. Inf. Syst. Sci, 3, 292–306.

[132] Cao, Z.; Xu, L.J. (2013).Direct image reconstruction for 3-D electrical resistance tomography by using the factorization method and electrodes on a single plane. IEEE Trans. Inst. Meas. 62, 999–1007..

[133] J.L. Mueller, D. Isaacson, and J.C. Newell. (2001). Reconstruction of conductivity changes due to ventilation and perfusion from EIT data collected on a rectangular electrode array," Physiol. Meas., vol. 22, no. 1, pp. 97-106.

[134] A. Borsic, R. Halter, Y Wan, A Hartov, and K.D. Paulsen. (2010). Electrical impedance tomography reconstruction for three-dimensional imaging of the prostate," Physiol. Meas., vol. 31, no. 8, pp. S1-S16.

[135] V A Cherepenin, Y V Gulyaev, A V Korjenevsky, S A Sapetsky, and T S Tuykin. (2012). An electrical impedance tomography system for gynecological application GIT with a tiny electrode array," Physiol. Meas., vol. 33, no. 5, pp. 849-862.

[136] H. Perez, M. Pidcock, and C. Sebu. (2017). A three-dimensional image reconstruction algorithm for electrical impedance tomography using planar electrode arrays. Inverse Probl. Sci. En., vol. 25, no. 4, pp. 471-491.

[137] "Wang, Y., Ren, S. and Dong, F. (2019). A Transformation-Domain Image Reconstruction Method for Open Electrical Impedance Tomography Based on Conformal Mapping. IEEE Sensors Journal, 19(5), pp.1873-1883.